

Computational Fluid Dynamics (CFD) Modelling of Renewable Energy Turbine Wake Interactions

by

Benjamin Michael Carver Johnson

A thesis submitted in partial fulfilment for the requirements for the degree of
Doctor of Philosophy at the University of Central Lancashire

May 2015

STUDENT DECLARATION FORM

Concurrent registration for two or more academic awards

I declare that while registered as a candidate for the research degree, I have not been a registered candidate or enrolled student for another award of the University or other academic or professional institution

Material submitted for another award

I declare that no material contained in the thesis has been used in any other submission for an academic award and is solely my own work

Signature of Candidate

Robinson

Type of Award

PhD

School

School of CEPS

Contents

Abstract	17
Acknowledgements	19
1 Introduction	31
1.1 Background/motivation	32
1.2 Aim and objectives	33
1.3 Thesis overview	34
1.4 Wind energy	34
1.4.1 Wind-farm	36
1.4.2 Wind turbine wake	38
1.5 Computational Fluid Dynamics	38
1.5.1 Turbulence	41
1.5.2 Reynolds number	41
1.5.3 Reynolds-Averaged Navier-Stokes	42
1.5.4 Large Eddy Simulations	43
2 Theory	45
2.1 Computational Fluid Dynamics	45
2.1.1 Reynolds-Averaged Navier-Stokes	46
2.1.2 Large Eddy Simulations	58

2.1.3	Detached Eddy Simulation	61
2.1.4	Direct Numerical Simulations	62
2.1.5	Discretization	63
2.2	Rotor models	66
2.2.1	Porous disc	66
2.2.2	Actuator disc method	70
2.2.3	Actuator line method	76
3	Literature review	80
3.1	Theory	80
3.1.1	One-dimensional momentum theory	80
3.1.2	Betz limit	82
3.1.3	Ideal Horizontal Axis Wind Turbine (HAWT)	83
3.2	Previous experimental work	85
3.2.1	NREL Unsteady Aerodynamics Experiment (UAE) project	85
3.2.2	Model EXperiments In COntrolled conditions (MEXICO) project	87
3.2.3	Mexnext project	88
3.3	Previous numerical work	88
3.3.1	Blade models	89
3.3.2	Vortex wake methods	89
3.3.3	Wake models and computer programs	90
3.4	Previous computational work	91
3.4.1	Software/codes	91
3.4.2	Reynolds-Averaged Navier-Stokes	93
3.4.3	Problems	94
3.4.4	Large Eddy Simulations	95
3.4.5	Boundary conditions	96

3.5	Rotor modelling	97
3.5.1	Actuator disc method	98
3.5.2	Actuator line method	99
3.5.3	Actuator surface	100
3.5.4	Full Rotor	100
4	Methods	103
4.1	One-dimensional momentum theory study	103
4.2	Porous disc study	104
4.2.1	Mesh	106
4.2.2	Boundary conditions	106
4.2.3	Resistance	109
4.2.4	Code comparison	110
4.2.5	Cell type study	110
4.3	Actuator disc study	112
4.3.1	Mesh	113
4.3.2	Boundary conditions	115
4.4	Two turbine study	116
4.4.1	Current work	118
4.4.2	Mesh	119
4.4.3	Boundary conditions	122
4.4.4	Repeatability study	122
4.5	Rotor diameter study	124
5	Results	126
5.1	One-dimensional momentum theory results	126
5.2	Porous disc Results	127
5.2.1	Influence of the boundary conditions	128

5.2.2	Wake predictions	128
5.2.3	Cell type study results	132
5.2.4	Code comparison results	135
5.3	Actuator disc study results	144
5.4	Two turbine study results	149
5.4.1	Repeatability study results	150
5.5	Rotor diameter study results	151
5.5.1	First turbine	152
5.5.2	60m spacing wake	154
5.5.3	60m spacing second turbine velocity	155
5.5.4	60m spacing second turbine power	158
5.5.5	30m spacing wake	162
5.5.6	30m spacing second turbine velocity	164
5.5.7	30m spacing second turbine power	165
5.5.8	Power comparison between spacings	169
6	Discussion	171
6.1	Computational techniques	171
6.1.1	RANS and LES	172
6.1.2	Cell type	172
6.1.3	Boundary conditions	173
6.1.4	ANSYS-CFX and ANSYS-Fluent	175
6.2	Rotor models	176
6.2.1	Near wake discrepancy	176
6.2.2	Actuator disc	178
6.2.3	Actuator line	179
6.2.4	Ground affect and shear	181

6.3	Scaling	182
6.3.1	Reynolds number	183
6.4	Rotor diameter	184
6.4.1	Wake	185
6.4.2	Power	185
6.4.3	Power Coefficient	189
6.4.4	Overall performance	194
6.4.5	Wind-farm	195
7	Conclusions & Recommendations	196
7.1	Conclusions	198
7.1.1	Porous disk in water	198
7.1.2	Influence of the boundary conditions	199
7.1.3	Actuator disc in air	199
7.1.4	Two turbine interactions	200
7.1.5	Influence of rotor diameter	201
7.2	Recommended work	202
	References	204
A	Reynolds number	226

List of Tables

4.1	Mesh densities using linear and quadratic cells	111
4.2	Various mesh densities and tip refinement.	121
4.3	Computational time for various mesh densities	122
5.1	Thrust coefficient results to 3 s.f.	130
5.2	Mesh densities using linear and quadratic cell types	133
5.3	Mesh variation in the repeatability study	150
5.4	Velocity at the first turbine to 3 s.f.	154
5.5	Approximate power extracted by the first turbine to 3 s.f.	154
5.6	Power difference of the first turbines compared with the baseline to 3 s.f.	155
5.7	Average velocity at the second turbine to 3 s.f.	159
5.8	Velocity difference at the second turbine compared to the baseline to 3 s.f.	159
5.9	Difference in power extracted by the second turbines compared to the baseline to 3 s.f.	160
5.10	Comparison in the combined power extracted by the 7.5m and 12.5m configurations with the baseline configuration to 3 s.f.	161
5.11	Power deficit of the second turbine to 3 s.f.	162
5.12	Average velocity at the second turbine with a spacing of 30m to 3 s.f.	165

5.13	Velocity difference at the second turbine compared to that behind the baseline to 3 s.f.	165
5.14	Difference in power of the second turbines compared to 10m turbine to 3 s.f.	168
5.15	Comparison in the combined power extracted by the 7.5m and 12.5m configurations with the baseline configuration to 3 s.f.	169
5.16	Power deficit of second turbine compared to the first turbine to 3 s.f. .	169
5.17	Comparison of the power extracted by the turbines with a spacing of 60m and 30m to 3 s.f.	170
6.1	New C_T values	174
6.2	Average velocity difference between this study and Réthoré <i>et al.</i> . .	179
6.3	Power of 9m configuration	189
6.4	New power coefficient values to 3 s.f.	191
6.5	Approximate power extract by the first turbine with a variable C_P to 3 s.f.	191
6.6	Power difference of the first turbines compared with the baseline using a variable C_P to 3 s.f.	191
6.7	C_P values calculated for the second turbine referred to as C_{P2}	192
6.8	Approximate power extract by the second turbine for different C_P values	192
6.9	Difference in power of the second turbines compared to 10m turbine .	193
6.10	Power deficit of the second turbine	193
6.11	Combined power of the first and second turbines for two variable C_P values	194

6.12 Comparison in the combined power extracted by the 7.5m and 12.5m configurations with the power extracted by the 10m configuration for two variable C_P values 194

List of Figures

1.1	Types of wind turbine	36
1.2	Illustration of the resolved and modelled parts of the flow	40
2.1	Difference in grid resolution using a wall function	57
2.2	Control volumes of (a) the cell-centred scheme, (b) the cell-vertex scheme (overlapping) and (c) the cell-vertex scheme (dual control volumes)	67
2.3	Geometry of two methods used to define disc location a) algebraically b) geometrically	68
2.4	Aerofoil cross-section showing force vectors	71
3.1	1D momentum theory	82
3.2	Aerofoil forces	84
4.1	1D momentum theory	104
4.2	Normalized velocity profiles showing different mesh densities (a) along the centre line and (b) 7 diameters downstream of the disc	107
4.3	Normalized velocity at the inlet of this study (solid line) and experimental data (o)	108
4.4	Difference in cell type	111

4.5	Representation of the blade used in the MEXICO project where the red zones represent the transition zones between aerofoils	112
4.6	Mexico study wind tunnel	113
4.7	Mesh used in the actuator disc study (a) cross-section through the domain and (b) detailed view	114
4.8	Centre line velocity for the 10m/s inlet with the 15×10^6 cell mesh (dashed line), 30×10^6 cell mesh (solid line), numerical study (o) and experimental data (.)	115
4.9	Two turbine domain with 3 diameter spacing on top and 6 diameter spacing on the bottom	119
4.10	Mesh refinement zones	120
4.11	Mesh comparison (a) 70m behind the first turbine and (b) detail view of the velocity deficit	123
4.12	Velocity difference between the 22 million and 37 million cell mesh densities	124
5.1	Pressure and velocity profiles along the centre line of the rotor given by (a) the 1D momentum theory and (b) the actuator disc method	127
5.2	Velocity profile with no disc of the channel flow (solid line) and the duct flow (dashed line) at 24m, 31m and 40m from the inlet	128
5.3	Velocity along the centre line showing the channel (solid line), duct (dashed line), numerical (x) and experimental data (o) for the C_T values of a) 0.61, b) 0.86 and c) 0.97 for the experimental study. The inlet 1 simulations are shown black and inlet 2 simulations are in red	130

5.4	Turbulence intensity along the centre line showing the channel (solid line), duct (dashed line), numerical (x) and experimental data (o) for the C_T values of a) 0.61, b) 0.86 and c) 0.97 for the experimental study. The inlet 1 simulations are shown black and inlet 2 simulations are in red.	131
5.5	Normalized velocity of the channel (solid line), duct (dashed line) and experimental data (o) at different C_T values of a) 0.61, 0.62, b) 0.86, 0.91 and c) 0.97, 0.99 for this study and the experimental study respectively. The inlet 1 simulations are shown black and inlet 2 simulations are in red. Each figure represents the distance downstream of the disc corresponding to 8R, 14R, 22R, 30R and 40R respectively	133
5.6	Turbulence intensity at 8R, 14R, 22R, 30R and 40R downstream of the disc, with the channel (solid line), duct (dashed line) and experimental data (o) at different C_T values of a) 0.61, 0.62, b) 0.86, 0.91 and c) 0.97, 0.99 for this study and the experimental study respectively. The inlet 1 simulations are shown black and inlet 2 simulations are in red .	134
5.7	Velocity profile 7 diameters behind the disc of the channel simulations with the quadratic cells (solid line) and linear cells (dashed line) . . .	136
5.8	Velocity profile 7 diameters behind the disc of the duct simulations with the quadratic cells (solid line) and linear cells (dashed line) . . .	137
5.9	Normalized turbulence intensity behind the disc	138
5.10	Normalized velocity profile through the centre of the domain with ANSYS-CFX (red), ANSYS-Fluent (blue) and experimental data (o) for the channel (solid line) and duct (dashed line) simulations	138
5.11	Normalized velocity profile behind the disc at $\frac{x}{2R} = 4$ with ANSYS-CFX (red), ANSYS-Fluent (blue) and experimental data (o) for the channel (solid line) and duct (dashed line) simulations	140

5.12	Normalized velocity profile behind the disc with ANSYS-CFX (red), ANSYS-Fluent (blue) and experimental data (o) for the channel (solid line) and duct (dashed line) simulations	141
5.13	Turbulence intensity through the centre of the domain with ANSYS-CFX (red), ANSYS-Fluent (blue) and experimental data (o) for the channel (solid line) and duct (dashed line) simulations	142
5.14	Turbulent intensity behind the disc at $\frac{x}{2R} = 4$ with ANSYS-CFX (red), ANSYS-Fluent (blue) and experimental data (o) for the channel (solid line) and duct (dashed line) simulations	142
5.15	Turbulence intensity behind the disc with ANSYS-CFX (red), ANSYS-Fluent (blue) and experimental data (o) for the channel (solid line) and duct (dashed line) simulations	143
5.16	Velocity profile through the centre of the domain at $1.84797m$ or $z/R = 0.82132$ for this study (solid line), experimental data (.) and previous numerical study (o) for three inlet velocities	145
5.17	Velocity variation towards the inlet for this study (solid line), experimental data (.) and previous numerical study (o)	146
5.18	Normalized velocity profile at $x/2R = -0.4$ with this study (blue) and previous numerical study (red o)	147
5.19	Normalized velocity profiles of this study (blue) and previous numerical study (red o) at various locations	148
5.20	Normalized velocity profiles at 50m, 60m and 70m downstream respectively of the first turbine with this study (solid line), previous numerical data at 5% (o) and 10% (x) ambient turbulence and experimental data (*)	150
5.21	Velocity difference along yz plane between two simulations used in the repeatability study	151

5.22	Detailed view of the velocity difference	151
5.23	Velocity profiles at the first turbine for each wind speed of 7m/s, 10m/s, 15m/s and 20m/s respectively and the different colours represent the different turbine configurations; 7.5m turbine (blue), 10m turbine (green) and 12.5m turbine (red)	153
5.24	Velocity at 70m behind the first turbine for each wind speed of 7m/s 10m/s, 15m/s and 20m/s respectively and the different colours represent the different turbine configurations; 7.5m turbine (blue), 10m turbine (green) and 12.5m turbine (red)	156
5.25	Velocity profile through the centre of the domain offset by 4m with velocity behind the 7.5m (blue), 10m (green) and 12.5m (red) turbines	157
5.26	Velocity profile through the centre of the domain offset by 2m with velocity behind the 7.5m (blue), 10m (green) and 12.5m (red) turbines	157
5.27	Velocity profiles at the second turbine for each wind speed of 7m/s 10m/s, 15m/s and 20m/s respectively and the different colours represent the different turbine configurations; 7.5m turbine (blue), 10m turbine (green) and 12.5m turbine (red)	158
5.28	Power extracted by the second turbine (7.5m turbine (blue), 10m turbine (green) and 12.5m turbine (red)) at different wind speeds	160
5.29	Combined power extracted by the first and second turbines at different wind speeds	161
5.30	Velocity profiles 70m behind the first turbine for each wind speed of 7m/s 10m/s, 15m/s and 20m/s respectively with the different colours representing the different turbine configurations; 7.5m turbine (blue), 10m turbine (green) and 12.5m turbine (red)	163
5.31	Velocity profile through the centre of the domain offset by 4m with velocity behind the 7.5m (blue), 10m (green) and 12.5m (red) turbines	164

5.32	Velocity profile through the centre of the domain offset by 2m with velocity behind the 7.5m (blue), 10m (green) and 12.5m (red) turbines	165
5.33	Velocity profiles at the second turbine for each wind speed of 7m/s, 10m/s, 15m/s and 20m/s respectively and the different colours represent the different turbine behind the 7.5m turbine (blue), 10m turbine (green) and 12.5m turbine (red)	166
5.34	Power extracted by the second turbine (7.5m turbine (blue), 10m turbine (green) and 12.5m turbine (red)) at different wind speeds	167
5.35	Combination of the power extracted by the first and second turbines at different wind speeds	168
6.1	Force distribution of (a) actuator disc and (b) actuator line methods	180
6.2	Isosurface of the vorticity (a) actuator disc and (b) actuator line methods	181
6.3	Log relationship between the Reynolds number and rotor diameter	184
6.4	Velocity contours on the YZ plane for the (a) 7.5m configuration, (b) 10m configuration and the (c) 12.5m configuration	186
6.5	Streamlines viewed along (a) the yz-plane and (b) the xy-plane	187
6.6	Power of each turbine at different wind speeds. Blue is the 7.5m turbine, green is the 10m turbine, red is the 12.5m turbine and light blue is the 9m turbine.	190

Abstract

This thesis presents Computational Fluid Dynamics (CFD) simulations of renewable turbines akin to those used for wind, hydro, and tidal applications. In line with similar studies in the literature and to significantly reduce computational expense, the models developed took the form of actuator discs with the solution of incompressible Reynolds-Averaged Navier-Stokes equations with the $k-\omega$ SST turbulence models.

Simulations were initially conducted of a single turbine in water and air and then two axially aligned turbines to study the flow field interactions. These models were compared with previous theoretical, experimental and numerical data evident in the literature. Generally, good agreement was found between these models and other analogous data sources in terms of velocity profiles in the far wake. The actuator disc method was underpinned using the transient actuator line method, which showed good agreement from a quantitative and qualitative viewpoint. However, it required significant additional computational time when compared to the actuator disc method.

Each of the models were developed and solved using complimentary commercially available CFD codes, ANSYS-CFX and ANSYS-Fluent. For this type of study, a critical evaluation of these codes was in all probability performed for the first time, where it is shown that for the studies investigated in this thesis ANSYS-CFX performed better than ANSYS-Fluent with respect to the computational effort (i.e. time and lines of code).

The novel contributions to knowledge of the work described in this thesis is in regard to the aerodynamic interactions between two turbines with different rotor diameters and its effect on performance. It was observed that the rotor diameter of the first turbine had a significant influence on the downstream turbines performance. Varying the power coefficient exaggerates the differences between the first turbines but predicts similar power extraction from the second turbines. Similar predictions with respect to power extraction are made if the power coefficient of the second turbine is defined using the free stream velocity or the local free stream velocity even though there is less power available for the second turbine to extract.

The work carried out as part of this thesis has been presented at two conferences [1][2] and published within peer-reviewed journals [3][4].

Acknowledgements

I would like to thank my fiancée for supporting me in every way possible and moving around the country for me to take this opportunity. My family for their continued support, particularly my granddad for proof reading and providing feedback on my multiple drafts.

I would like to thank my supervisors, Drs Justin Whitty and Jonathan Francis for guiding and shaping me into the researcher I am today. I am also grateful for the other researcher at the University who make my time far more enjoyable.

Lastly, I would like to acknowledge the Samuel Lindow Foundation who provided me with a bursary and the opportunity to carry out this research.

Nomenclature

Latin

a	Axial induction factor [–]
a'	Angular or tangential induction factor [–]
a_1	Constant (fraction of the rate of turbulence production) [–]
A	Boundary layer model constant [–]
A_r	Rotor swept area [m^2]
b	Distance between a grid point and source point [m]
B	Number of blades [–]
c	Chord length [m]
c_p	Specific heat capacity [Nm/K]
C	Closure coefficient [–]
$C_{1,2}$	Prescribed matrix [–]
C_D	Drag coefficient [–]
C_{ijk}	Turbulent transport tensor [–]

C_L	Lift coefficient [-]
C_p	Power coefficient [-]
C_S	Smagorinsky constant [-]
C_T	Thrust coefficient [-]
CD_{kw}	Cross diffusion term [-]
D	Drag force [N]
D_{AD}	Actuator Disc [N/m^3]
D_{ADUT}	Actuator Disc with Uniform Thrust definition term [N/m^2]
D_{ADVT}	Actuator Disc with Variable Thrust definition term [N/m]
D_{ADL}	Actuator Disc with Lift definition term [N/m]
D_{ADLD}	Actuator Disc with Lift and Drag definition term [N/m]
D_{AL}	Actuator Line definition term [N/m]
D_n	Disc definition term [N/m]
d	Rotor thickness/depth [m]
e_L	Lift unit vector [-]
e_D	Drag unit vector [-]
f	Base term used in the definition of the actuator methods [N/m^2]
F_1, F_2	Blending function [-]
F_P	Prandtl's correction factor [-]

F_G	Glauert's correction factor [–]
F_S	Shen <i>et al.</i> correction factor [–]
G	Filter function [–]
$H(x)$	Step function [–]
i, j	Represents components in the i, j th direction [–]
k	Specific turbulence kinetic energy [m^2/s^2]
k	Thermal diffusivity [m^2/s]
K	Resistance coefficient [–]
l	Characteristic length [m]
L	Lift force [N]
L_n	Actuator line area [m^2]
L_S	Mixing length for the SGS [m]
\dot{m}	Mass flow-rate [m/s]
Ma	Mach number [–]
n	Integer number [–]
N	The blade number [–]
p	Pressure [N/m^2]
P	Power [Nm/s]
P_{WF}	Wind-farm power [Nm/s]

P_{WT}	Wind turbine power [Nm/s]
r	Radius (variable) [m]
r, θ, z	Cylindrical coordinates [m, rad, m]
R	Radius [m]
\mathfrak{R}	Function defining the volume of the rotor [–]
R_R	Function defining the rotor area [–]
R_r	Variable rotor radius [m]
R_T	Function defining the rotor thickness [–]
\mathbb{S}	Mean strain tensor [N/m^2]
S	Invariant measure of the strain rate [$1/s$]
S_i	Source term in i th direction [various]
\bar{S}_{ij}	Rate-of-strain tensor [$1/s$]
$S_{r,\theta,x}$	Source terms in cylindrical coordinates [various]
t	Time [s]
T	Thrust [N]
Υ	Temperature [K]
u, v, w	Velocity components in the x, y, z directions [m/s]
$\bar{u}, \bar{v}, \bar{w}$	Mean velocity components in the x, y, z directions [m/s]
\bar{u}_i	Mean velocity component [m/s]

u', v', w'	Velocity fluctuation components in the x, y, z directions [m/s]
\bar{U}	Mean velocity [m/s]
U	Velocity [m/s]
U_0	Free stream Velocity [m/s]
U_i	Velocity in $i = x, y$ or z direction [m/s]
U_r	Velocity at the rotor [m/s]
U_t	Velocity at the turbine [m/s]
U^*	Friction velocity [m/s]
\bar{U}_i	Large scale filtered component [–]
U_{inlet}	Inlet velocity [m/s]
U_{rel}	Relative velocity [m/s]
V	Volume of the computational cell [–]
\vec{V}	Velocity vector [m/s]
$V_{r,\theta,x}$	Velocity in cylindrical coordinates [m/s]
V_z	Axial velocity [m/s]
V_θ	Tangential velocity [m/s]
x, y, z	Cartesian coordinate system [–]
$x_{i,j}$	Cartesian coordinate system [–]
$(X, Y, Z)_R$	Local coordinate system of the rotor [m]

y_d	Distance to the closest wall [m]
y_s	Distance to the nearest surface [m]
y_w	Water depth [m]

Greek

$\alpha^\omega, \beta_1^\omega, \beta_2^\omega, \sigma_1^\omega, \sigma_2^\omega$ Closure coefficients of k - ω turbulence model [–]

$\alpha^\varepsilon, \beta_1^\varepsilon, \sigma_1^\varepsilon, \sigma_2^\varepsilon, C_\varepsilon$ Closure coefficients of k - ε turbulence model [–]

$\alpha^{sst}, \beta_1^{sst}, \beta_2^{sst}, \sigma_1^{sst}, \sigma_2^{sst}$ Closure coefficients of k - ω SST turbulence model [–]

α	Local angle of attack [$^\circ$]
β_i	Initial blade position [$^\circ$]
β_n	Blade position [$^\circ$]
δ_{ij}	Kronecker delta [–]
ζ	Constant of smoothing function [–]
ε	Specific dissipation [m^2/s^3]
ε_{ij}	Dissipation tensor [m^2/s^3]
ξ	Thermal conductivity [W/mK]
γ	Local pitch angle [$^\circ$]
κ	von Karman constant [–]
ℓ	Turbulence length scale [m]

ℓ_{mix}	Mixing length [m]
λ	Tip speed ratio [–]
μ	Dynamic viscosity [Ns/m^2]
μ_T	Eddy viscosity [m^2/s]
μ_{sgs}	Eddy viscosity of the SGS [m^2/s]
η_ζ	Smoothing function [–]
η	Kolmogorov length scale [m]
Ω	Rotational speed [rad/s]
ω	Specific dissipation rate [$1/s$]
ρ	Density [kg/m^3]
$-\overline{u'_i u'_j}$	Reynolds stresses [N/m^2]
τ_{ij}	Reynolds stress tensor [N/m^2]
τ_{sgs}	Subgrid scale stress term [N/m^2]
ν	Kinematic viscosity [m^2/s]
$\psi(x, t)$	Flow variable [–]
$\bar{\psi}(x, t)$	Large scale filtered component [–]
$\psi'(x, t)$	Small scale sub-filtered component [–]
ϕ_{sst}	Variables used in the k - ω SST model [–]
ϕ_ω	Variables used in the k - ω model (α^ω, \dots) [–]

ϕ_ε	Variables used in the transformed k - ε model ($\alpha^{\omega\varepsilon}, \dots$) [–]
ϕ	Angle between U_{rel} and rotor plane [°]
φ	Blade twist [°]
Θ	Fluid domain [–]
∇^2	Laplacian operator [–]
$\Delta = (\Delta_1\Delta_2\Delta_3)^{1/3}$	Filter width [m]
Δ_i	Filter width in the i th direction [m]
ζ	Viscous dissipation term [m^2/s]
Δp	Change in pressure over the disc [N/m^2]
Δt	Time step [s]
Δx	Spatial step [m]
Π_{ij}	Pressure-strain correlation tensor [m^2/s^3]
σ_k	Closure coefficient [–]
$\dot{\gamma}$	Shear rate [$1/s$]

Abbreviations

1D	One Dimension
2D	Two Dimensions
3D	Three Dimensions

<i>ABL</i>	Atmospheric Boundary Layer
<i>AD</i>	Actuator Disc
<i>ADL</i>	Actuator Disc with Lift
<i>ADLD</i>	Actuator Disc with Lift and Drag
<i>ADM</i>	Actuator Disc Method
<i>ADUT</i>	Actuator Disc with Uniform Thrust
<i>ADVT</i>	Actuator Disc with Variable Thrust
<i>ADV</i>	Acoustic Doppler Velocimeter
<i>AL</i>	Actuator Line
<i>ALM</i>	Actuator Line Method
<i>APG</i>	Adverse Pressure Gradient
<i>AS</i>	Actuator Surface
<i>BE</i>	Blade Element
<i>BEM</i>	Blade Element Momentum
<i>BSL</i>	Baseline
<i>CEL</i>	CFX Expression Language
<i>CFD</i>	Computational Fluid Dynamics
<i>CFL</i>	Courant–Friedrichs–Lewy
<i>DES</i>	Detached Eddy Simulation

<i>DNS</i>	Direct Numerical Simulation
<i>DNW</i>	German Dutch Wind tunnel Organization
<i>EU</i>	European Union
<i>FDM</i>	Finite Difference Method
<i>FEM</i>	Finite Element Method
<i>FVM</i>	Finite Volume Method
<i>GE</i>	General Electric
<i>HAWT</i>	Horizontal Axis Wind Turbine
<i>HPC</i>	High Performance Computer
<i>IEA</i>	International Energy Agency
<i>KE</i>	Kinetic energy
<i>LES</i>	Large Eddy Simulation
<i>LLF</i>	Large Scale Low Speed Facility
<i>MCT</i>	Marine Current Turbines
<i>MEXICO</i>	Model EXperiments In COntrolled COnditions
<i>NDA</i>	Non Disclosure Agreements
<i>NREL</i>	National Renewable Energy Laboratory
<i>PIV</i>	Particle Image Velocimetry
<i>RANS</i>	Reynolds-Averaged Navier-Stokes

<i>RSM</i>	Reynolds Stress Model
<i>RMS</i>	Root-Mean-Square
<i>SST</i>	Shear Stress Transport
<i>VAWT</i>	Vertical Axis Wind Turbine
<i>VTM</i>	Vorticity Transport Model
<i>UDF</i>	User Defined Function
<i>UK</i>	United Kingdom

Chapter 1

Introduction

The world is currently moving towards renewable energy sources. This growth is driven by policy and renewable energy targets such as the European Union (EU) Renewables directive [5] which aims to have 20% of the EU energy needs met by renewable energy by 2020. Two of these sources, wind and tidal, employ turbines to extract energy from the environment. Tidal or marine energy is very promising as it provides predictable energy and the UK has an estimated 50% of Europe's tidal energy resource¹. However, it is currently in its infancy and the UK only has 9MW installed capacity. The wind energy industry is more mature, and continues to grow despite the economic climate. In the year 2000 there was 17.4GW of installed capacity worldwide. This grew by an average of 27% each year until 238GW was installed by 2011 [6]. As capacity increases the percentage of growth is likely to fall. Between 2011 and 2012 growth slowed to 19% with total installed capacity reaching 283GW [6][7]. However, approximately 13GW was installed during this time in both the US and China (the two largest renewable energy markets) and almost 45GW worldwide [6]. Due to the increased maturity and knowledge available, the majority of the work described in this thesis will be focused on wind energy.

¹<http://www.renewableuk.com/en/renewable-energy/wave-and-tidal>

The UK wind industry, which is leading the offshore market, grew by 29% in 2012 to 8.4GW [6] and now contributes as much as 12%² to UK energy requirements. This growth and the trend in wind-farms increasing in size, to the point where they are sometimes constructed in stages, means manufacturers and developers are often unable to create wind-farms using a single wind turbine specification. Many existing wind-farms are also under consideration to be re-powered and/or extended. This can result in wind-farms being made up of multiple designs and/or supplied by a number of different companies, meaning different wind turbines with varying sizes and specifications are installed at a single site. An example of this is the Roscoe wind-farm in Texas, USA which uses three types of wind turbines (Mitsubishi 1MW, Siemens 2.3MW and GE 1.5MW) ranging from 350ft to 415ft in height. Such situations are seldom by design, but are rapidly becoming more common as developers strive to meet renewable energy policy targets by extending current wind-farms and building larger ones.

1.1 Background/motivation

A wind-farm using different wind turbines is not necessarily a negative proposition and may, in fact, improve overall power output. Chowdhury *et al.* [8] discussed the factors affecting the maximum power output of a wind-farm and included the wind turbine rotor diameter as a variable in their optimization algorithm. The study [8] focused on a single wind-farm case, which originally consisted of a 3×3 wind turbine array. To allow thousands of configurations to be investigated, a simple velocity deficit model [9] was used with the optimization algorithm. The algorithm found a 30% increase in energy yield using identical wind turbines and a 43% increase using rotor diameter as a variable. This suggests a 10% increase in energy yield of the wind-farm is possible using wind turbines with different sizes. This provides promising insight into possible

²<http://www.gridwatch.templar.co.uk/>

new optimization approaches, which have not yet been investigated. However, the study [8] was limited to a single case using a single wind speed, hub height and blade geometry while varying the rotor diameter and location. It is necessary to conduct a more detailed study into how the rotor diameter influences the energy yield of a wind-farm. To the author's knowledge, there are no computational studies on the interactions of different sized turbines within the literature.

1.2 Aim and objectives

This thesis aims to investigate the affect rotor diameter size has on turbine interactions, through the use of Computational Fluid Dynamics (CFD) modelling and aerodynamic analysis.

These will be demonstrated via achievement of the following objectives:

1. to identify current turbine models used within the literature and demonstrate their implementation within commercially available CFD software;
2. to produce salient benchmark regimes of turbine model(s) for verification of modelling procedures with analogous studies within the literature;
3. to predict the aerodynamic flow field interactions between two similar axially aligned turbines;
4. to analyse the relative sensitivity of the aforementioned interactions to rotor size;
5. to critically evaluate the overall performance of two non-identical (different rotor sizes) turbines;
6. to demonstrate if there are any benefits/limitations of using non-identical turbines compared to using identical turbines;

7. to produce publishable quantitative and qualitative evidence in order to fully describe any benefits/limitation realized.

1.3 Thesis overview

This thesis is divided into seven chapters. The opening chapter describes the motivation, key concepts and principles for the research described in this thesis. Chapter 2 discusses the theory behind the methods used in this thesis; considering the mathematics behind the main CFD methods available, focusing on the RANS and LES methods. It concludes by detailing the rotor models employed in this thesis and their implementation within CFD codes. Chapter 3 consists of a literature review covering previous theoretical, experimental and numerical work on turbines and their wakes, concentrating on current numerical methods. Chapter 4 describes the five CFD studies conducted as part of this thesis, featuring simulations of a single turbine in water and air and two axially aligned turbines. Chapter 5 details the results of the five studies, described in Chapter 4, focusing on the interactions between two axially aligned turbines. Chapter 6 is the discussion chapter, where quantitative and qualitative evaluation of the results obtained in this thesis is performed. Finally, Chapter 7 presents the major conclusions of the work conducted in this thesis, highlighting the novel findings and concluding with recommendations for further work.

1.4 Wind energy

Wind energy has always been an important resource. Windmills were built as long as 3000 years ago and wind was very important for early travel utilizing sails [10]. For more information on wind energy's history see the references [10][11] and their extended reading lists.

Wind turbines work by converting the kinetic energy of the wind into usable energy, normally electrical. However, windmills convert the kinetic energy into mechanical power and are commonly used to pump water or grind grain. There are two main types of wind turbine: the Horizontal Axis Wind Turbine (HAWT), which is the most common design today and will be the focus of this thesis; and the Vertical Axis Wind Turbine (VAWT) such as the Darrieus and Savonius designs. Both designs are shown in Figure 1.1. There are two variations on these types: drag-based variations which try to catch or block the wind and use drag forces to rotate (e.g. cup anemometers) and lift-based turbines, which use blades that work the same way as aeroplane wings, responding to the wind by generating aerodynamic lift. Both of these forces are explained in more detail in subsection 3.1.3. The force created turns the rotor about its axis, thus generating shaft torque which turns a generator. Turbines may or may not have a gearbox depending on the configuration (see reference [10][11] for more detail). The power extracted by a turbine is calculated from the kinetic energy in the air, multiplied by the fraction extracted as shown in equation (1.1).

$$P = KE \times C_p = \frac{1}{2} \dot{m} u^2 C_p = \frac{1}{2} (\rho A_r u) u^2 C_p = \frac{1}{2} \rho \pi r^2 u^3 C_p. \quad (1.1)$$

Where KE is the kinetic energy per sec, C_p is the power coefficient, \dot{m} is the mass flow-rate, u is the wind speed, ρ is the air density, A_r is the rotor swept area and r is the rotor radius.

Equation (1.1) shows that changes in wind speed have the largest affect on power extraction, which is why it is so important to place the wind turbine in the *best* location. The power coefficient (discussed in subsections 3.1.1 and 3.1.2) varies between 0–0.6 and the density remains approximately equal to one, so have a smaller affect on the power. The rotor radius is the easiest variable to change by design. It has a greater affect on the power extracted than other variables, as the radius is squared. This is the

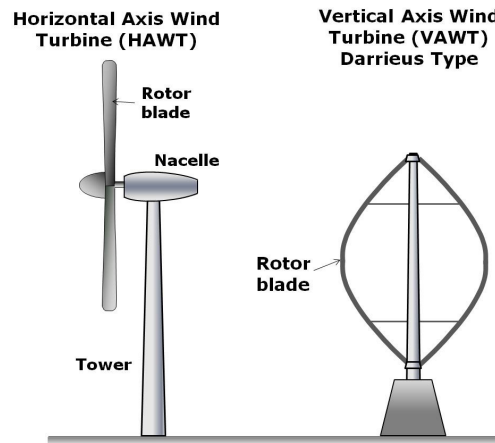


Figure 1.1: Types of wind turbine

main reason for the trend in wind turbine design towards bigger turbines in order to produce more power.

1.4.1 Wind-farm

Calculating the power of a wind-farm is much more complex than a single turbine, as a wind-farm is not just a sum of its individual parts.

$$P_{WF} \neq n \times P_{WT} \quad (1.2)$$

Where P_{WF} is the wind-farm power, n is the number of turbines and P_{WT} is the wind turbine power [12].

Downwind turbines experience a power reduction by as much as 40% compared to that of an isolated turbine [13][14]. When averaged over all wind directions this power loss has been calculated at approximately 10 – 20% [15]. These power losses are due to the wake of the upwind turbine and its interactions on the turbines downwind; this is often referred to as the wake loss. The wake interactions also affects the fatigue loads of the turbines. Due to these factors, wind-farm design is concerned with minimizing wake interactions.

Wind-farm optimization

To overcome wake interactions, wind turbines need to be positioned to minimize the affect of this phenomenon. However, this is not always practical, as it would require a wide spaced wind-farm, creating a very low power density (power per area). The wake of a wind turbine is extremely complex in nature and is affected by an extensive list of variables including atmospheric turbulence and wind shear (change in wind speed with height), as well as the wind direction. The latter can change rapidly and varies both in time and space (location), which makes it difficult to predict and model.

There are a wide range of wind-farm optimization techniques and programs which use various variables and assumptions. These are predominately mathematical in nature, using simplified engineering models of the flow parameters with a mathematical algorithm to determine the turbine's location. There are a number of optimization algorithms used including genetic algorithms, heuristic algorithms and swarm optimization. For more details see reference [16].

The optimization methods have limitations, as all programs sacrifice accuracy for speed. This enables hundreds and thousands of possible layout combinations to be simulated and assessed. Some codes are also limited in terms of the turbine locations, using only grid layouts or discrete points instead of continuous points in space. Another important limitation is the input data (which will be discussed in section 3.2). Many optimization programs use a flow modeller to provide an estimation of the flow field, instead of calculating it explicitly. One popular method is the Wind Atlas Analysis and Application Program, referred to as WAsP³. WAsP uses wind mast data and linear flow models to predict the flow field.

³www.wasp.dk

1.4.2 Wind turbine wake

The rotor causes the wind to slow; this slower moving air is referred to as the wake. The wake is commonly divided into two or three regions: the near wake and the far wake, with some also considering the transition phase as an additional region [17].

This division in the wake is made by defining the near wake as the region which is directly affected by the geometry of the rotor and the aerodynamics of the blades (number of blades and their associated vortices). This definition is ambiguous, resulting in various region sizes ranging from one diameter to several, depending on the flow conditions. Analysis in the near wake region focuses on wind turbine performance and wake development. The far wake region is defined as beyond the near wake, where the vortex system has broken down. Here the focus is on wake modelling and the turbine's influence on its surroundings.

1.5 Computational Fluid Dynamics

Fluid mechanics is the study of fluids either in motion (fluid dynamics) or at rest (fluid statics). Computational Fluid Dynamics (CFD) is an extension of fluid mechanics; it describes fluid motion through the use of numerical techniques using a computer. It is concerned with the solution of the velocity field and hence, the pressure field for given fluid properties (e.g. density, viscosity (measure of fluids resistance to flow) and surface tension). Both liquids and gases are considered as fluids. The two main obstacles in fluid mechanics to a workable theory are viscosity and geometry [18].

In a small number of idealized cases viscosity can be neglected, rendering the flow fields inviscid. However, for the vast majority of cases viscosity is present and may even vary, which increases the difficulty of constructing and using the basic equations [18]. Moreover, it can have a destabilizing effect on the aforementioned flow field

creating a disorderly, random phenomenon known as turbulence.

Complex geometry featuring rapid changes in the geometrical bounds of the fluid, make it difficult to find so-called ‘closed-formed analytical solutions’ of problems, which is why most textbooks concentrate on simple geometries such as flat plates and pipes. It is possible to solve problems featuring complex geometry and viscosity using numerical techniques on a computer which is commonly known as Computational Fluid Dynamics (CFD).

CFD implements conservation principles, including the three fundamental conservation equations of:

- Mass (continuity)
- Momentum (Newton’s second law [19])
- Energy (first law of thermodynamics [20][21])

By applying conservation principles to fluid motion it is possible to define the Navier-Stokes (N-S) Equations, which can be given in different forms. Equation (1.3) - (1.4) gives them in incompressible vector form. These equations describe the motion of any Newtonian fluid.

$$\nabla \cdot \vec{V} = 0 \quad (1.3)$$

$$\rho \left(\frac{\partial \vec{V}}{\partial t} + \vec{V} \cdot \nabla \vec{V} \right) = -\nabla p + \mu \nabla^2 \vec{V} + \vec{S} \quad (1.4)$$

Where \vec{V} is the velocity vector, t is time, ρ is density, p is the pressure, μ is the viscosity, \vec{S} is a source term and ∇^2 is the Laplacian operator.

Incompressibility is assumed for flows when the local Mach number (the ratio of the speed of an object to the speed of sound of the fluid) is below 0.3. For wind turbines the flow has velocities normally around 5 – 25m/s, resulting in a Mach number of less

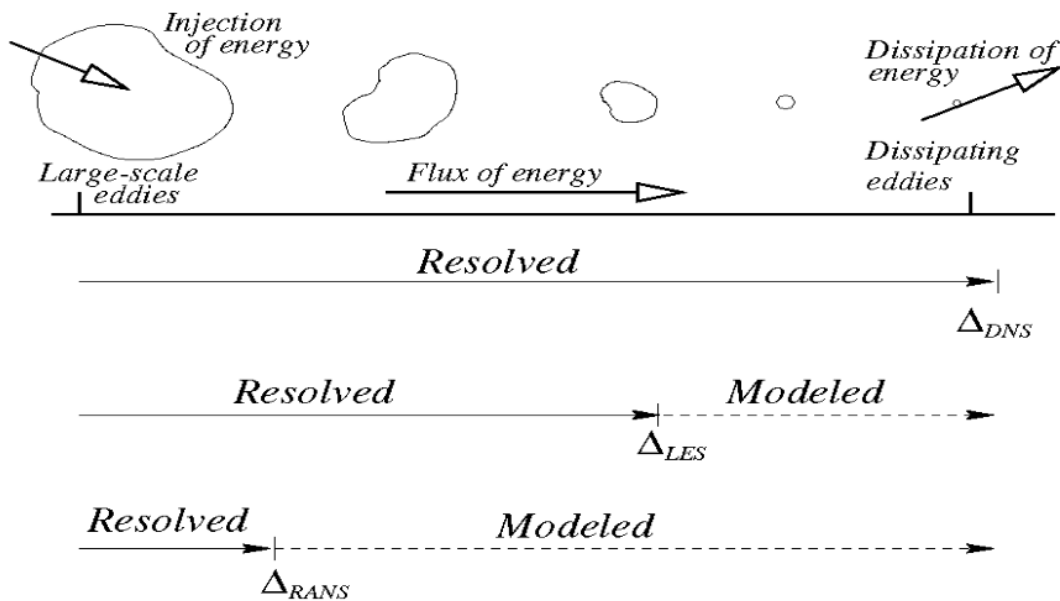


Figure 1.2: Illustration of the resolved and modelled parts of the flow

than 0.1, therefore the incompressible assumption is completely justifiable [22].

Although the incompressible Navier-Stokes equations implicitly describe turbulent flow fields they are inherently difficult to solve due to the non-linear nature, specifically the convective acceleration term $(\vec{V} \cdot \nabla \vec{V})$. Due to this there are a number of different CFD methodologies, each of which numerically resolve the Navier-Stokes equations and model the resulting flows to varying degrees as shown in Figure (1.2). Four such methods are the Reynolds-Averaged Navier-Stokes (RANS), Large Eddy Simulation (LES), Detached Eddy Simulation (DES) and Direct Numerical Simulation (DNS) which are briefly mentioned in this section with a more detailed description in Chapter 2.1. There is much research reported in the literature as well as a number of textbooks with greater detail regarding these methods, including references [18][23][24]. The difference between these models is their consideration of turbulence modelling.

1.5.1 Turbulence

Turbulence is characterized by random velocity variations within the flow that are generally modelled using statistical methods, based on experimental work [24]. If a fluid is not turbulent then it is said to be laminar, and is normally characterized by steady parallel fluid layers with no mixing. The problem with solving turbulent fluid problems is that turbulence is inherently three-dimensional, and operates at a smaller length scale than laminar (non-turbulent) flows. The Atmospheric Boundary Layer (ABL) can have a length scale ranging from approximately 1km to as small as 1mm [25] and blade boundary layers can have even smaller scales. This creates a problem in trying to resolve all the length scales. However, it is sometimes feasible and is called Direct Numerical Simulation (DNS) which is extremely computationally expensive and is not always viable. To overcome this a large number of turbulence models have been constructed for these small length scales, allowing the large scales to be resolved. There are a large number of books and other materials available on this approach, such as reference [24].

1.5.2 Reynolds number

The Reynolds number, Re , is a dimensionless number (has no units) that is used in fluid mechanics to describe flow. In 1883 Osborne Reynolds [26] showed that the transition from laminar to turbulent flow occurs at a critical value. The Reynolds number is commonly calculated using equations (1.6)-(1.7), referred to as the ratio of inertia force to viscous force, as shown in equation (1.5) with a proof given in Appendix A. Laminar flows feature low Reynolds numbers. The higher the Reynolds number the more likely a flow is to be turbulent; and the finer the small length scales (mixing)

within the flow.

$$Re = \frac{\text{Inertia force}}{\text{Viscous force}} \quad (1.5)$$

$$= \frac{\rho ul}{\mu} \quad (1.6)$$

$$= \frac{ul}{\nu} \quad (1.7)$$

Where ρ is the density, u is the speed, l is a characteristic length, μ is the dynamic viscosity and $\nu = \frac{\mu}{\rho}$ is the kinematic viscosity.

1.5.3 Reynolds-Averaged Navier-Stokes

The Reynolds-Averaged Navier-Stokes (RANS) method is the fastest CFD approach. It was first described in 1895 by Osborne Reynolds [27]. It uses time averaged motion, which introduces a new quantity known as the Reynolds stress. RANS models compute this variable either through the use of an eddy-viscosity model or Reynolds Stress model. The eddy-viscosity models vary with complexity, ranging from algebraic models to two equation models. The most commonly used in wind turbine applications are the two equation models k - ϵ [28], k - ω [24] and k - ω SST [29], where k is the turbulence kinetic energy per unit mass (or specific turbulence kinetic energy), ϵ is the specific dissipation and ω is the specific dissipation rate and are described in section 2.1.1.

The problem with the eddy-viscosity models is that they are based on the Boussinesq hypothesis [30], discussed in section 2.1.1. It is considered inadequate and invalid for flows featuring sudden changes in mean strain rate, rotation and 3D effects [24], all of which feature in turbine wakes. Nonetheless, it is still possible to use RANS methods without relying on the Boussinesq hypothesis by using the Reynolds Stress Method (RSM). However, RSM requires six additional equations to be solved, making it much

more resource expensive; and similar assumptions to the Boussinesq hypothesis are used.

1.5.4 Large Eddy Simulations

Large Eddy Simulation (LES) is able to handle unsteady anisotropic turbulent flow much better than RANS, but requires more computational resources. LES is increasingly being used due to the increase in computer power and resources that are now available.

As the name suggests, LES resolves large eddies while the eddies smaller than the grid size are modelled using a sub-grid scale (SGS) model. This approach is based on the assumption that the smallest eddies have a more or less universal characteristic that is not dependent on the flow geometry. This distinction between resolved and modelled is done through a filtering function applied to the Navier-Stokes equations. This introduces a new term called the SGS stress (similar to the Reynolds stress tensor of the RANS method). This stress is used to represent the effects of the SGS modelled eddies on the larger resolved eddies of the flow. This stress needs to be calculated and there are a large number of models available.

Although specific models have been developed, it is possible to use turbulence models developed for the RANS application (such as k - ϵ and k - ω models), which means that problems with the Boussinesq Hypothesis are still encountered. However, the fact that they are only used on the small scale eddies reduces the documented limitations. Réthoré [31] showed that if cell size is taken small enough, then the error made by the k - ϵ model and the eddy-viscosity concept are negligible. Due to this, it is very common to use one equation models based on the Smagorinsky model [32], such as the Smagorinsky Lilly model [33][34].

Near solid boundaries, LES becomes extremely computationally expensive. A

method used to reduce this is a hybrid approach where RANS is employed in the near wall region and LES everywhere else, this is called a Detached Eddy Simulation (DES).

Chapter 2

Theory

This chapter describes the theory behind the methods employed in this thesis. It covers the main CFD methods focusing on the RANS and LES methods as well as discretization methods. The chapter concludes with descriptions of the actuator methods (as these are the main rotor models used within the literature), and their implementation with CFD codes.

2.1 Computational Fluid Dynamics

This section discusses the mathematics used as part of the Computational Fluid Dynamics (CFD) process. For more details including the derivation of these equations see the references [24][35][36]. This thesis considers only incompressible situations and as such only the incompressible equations will be discussed. It should be noted that some of the nomenclature used here is slightly different to those of the references, this is to provide clearer differences between described models and provide consistency within this thesis.

CFD uses numerical techniques and a computer to solve fluid flow problems, specifically the Navier-Stokes (N-S) equations, which can be given in different forms. Equation (1.3) - (1.4) gives them in compact incompressible vector form which does not do them justice in term of complexity, whereas equations (2.1) - (2.4) gives them in Cartesian form. These equations describe the motion of any Newtonian fluid.

$$\frac{\partial u}{\partial x} + \frac{\partial v}{\partial y} + \frac{\partial w}{\partial z} = 0 \quad (2.1)$$

$$\rho \left(\frac{\partial u}{\partial t} + u \frac{\partial u}{\partial x} + v \frac{\partial u}{\partial y} + w \frac{\partial u}{\partial z} \right) = -\frac{\partial p}{\partial x} + \mu \left(\frac{\partial^2 u}{\partial x^2} + \frac{\partial^2 u}{\partial y^2} + \frac{\partial^2 u}{\partial z^2} \right) + S_x \quad (2.2)$$

$$\rho \left(\frac{\partial v}{\partial t} + u \frac{\partial v}{\partial x} + v \frac{\partial v}{\partial y} + w \frac{\partial v}{\partial z} \right) = -\frac{\partial p}{\partial y} + \mu \left(\frac{\partial^2 v}{\partial x^2} + \frac{\partial^2 v}{\partial y^2} + \frac{\partial^2 v}{\partial z^2} \right) + S_y \quad (2.3)$$

$$\rho \left(\frac{\partial w}{\partial t} + u \frac{\partial w}{\partial x} + v \frac{\partial w}{\partial y} + w \frac{\partial w}{\partial z} \right) = -\frac{\partial p}{\partial z} + \mu \left(\frac{\partial^2 w}{\partial x^2} + \frac{\partial^2 w}{\partial y^2} + \frac{\partial^2 w}{\partial z^2} \right) + S_z \quad (2.4)$$

Where x, y, z is the Cartesian coordinate system, u, v, w is the Cartesian velocity system, t is time, ρ is density, p is the pressure, μ is the viscosity and $S_{x,y,z}$ is a source term.

2.1.1 Reynolds-Averaged Navier-Stokes

As previously mentioned the Navier-Stokes equations are inherently difficult to solve directly due to their non-linear nature, specifically the convective acceleration terms. There are a number of numerical methods that approximate these equations. The most commonly used method involves using Reynolds averaging or Reynolds decomposition which was first described in 1895 by Osborne Reynolds [27]. This splits the instantaneous velocities into a mean velocity (\bar{u}) and a fluctuation (u') such that $u = \bar{u} + u'$. In this case the mean component has to have a number of properties such as

the mean of the fluctuation is zero ($\overline{u'} = 0$) and is known as a Reynolds operator. Using Reynolds averaging on the Navier-Stokes equations and then time averaging the result produces a time averaged version of these equations which are commonly known as the Reynolds-Averaged Navier-Stokes (RANS) equations shown in Cartesian form in equations (2.5)-(2.8) and in tensor form in equation (2.9).

$$\frac{\partial \bar{u}}{\partial x} + \frac{\partial \bar{v}}{\partial y} + \frac{\partial \bar{w}}{\partial z} = 0 \quad (2.5)$$

$$\begin{aligned} \rho \left(\frac{\partial \bar{u}}{\partial t} + \bar{u} \frac{\partial \bar{u}}{\partial x} + \bar{v} \frac{\partial \bar{u}}{\partial y} + \bar{w} \frac{\partial \bar{u}}{\partial z} \right) &= -\frac{\partial \bar{p}}{\partial x} + \mu \left(\frac{\partial^2 \bar{u}}{\partial x^2} + \frac{\partial^2 \bar{u}}{\partial y^2} + \frac{\partial^2 \bar{u}}{\partial z^2} \right) \\ &\quad - \rho \left(\frac{\partial \overline{u'u'}}{\partial x} + \frac{\partial \overline{u'v'}}{\partial y} + \frac{\partial \overline{u'w'}}{\partial z} \right) + S_x \end{aligned} \quad (2.6)$$

$$\begin{aligned} \rho \left(\frac{\partial \bar{v}}{\partial t} + \bar{u} \frac{\partial \bar{v}}{\partial x} + \bar{v} \frac{\partial \bar{v}}{\partial y} + \bar{w} \frac{\partial \bar{v}}{\partial z} \right) &= -\frac{\partial \bar{p}}{\partial y} + \mu \left(\frac{\partial^2 \bar{v}}{\partial x^2} + \frac{\partial^2 \bar{v}}{\partial y^2} + \frac{\partial^2 \bar{v}}{\partial z^2} \right) \\ &\quad - \rho \left(\frac{\partial \overline{u'v'}}{\partial x} + \frac{\partial \overline{v'v'}}{\partial y} + \frac{\partial \overline{v'w'}}{\partial z} \right) + S_y \end{aligned} \quad (2.7)$$

$$\begin{aligned} \rho \left(\frac{\partial \bar{w}}{\partial t} + \bar{u} \frac{\partial \bar{w}}{\partial x} + \bar{v} \frac{\partial \bar{w}}{\partial y} + \bar{w} \frac{\partial \bar{w}}{\partial z} \right) &= -\frac{\partial \bar{p}}{\partial z} + \mu \left(\frac{\partial^2 \bar{w}}{\partial x^2} + \frac{\partial^2 \bar{w}}{\partial y^2} + \frac{\partial^2 \bar{w}}{\partial z^2} \right) \\ &\quad - \rho \left(\frac{\partial \overline{u'w'}}{\partial x} + \frac{\partial \overline{v'w'}}{\partial y} + \frac{\partial \overline{w'w'}}{\partial z} \right) + S_z \end{aligned} \quad (2.8)$$

$$\rho \frac{D\bar{u}_i}{Dt} = -\frac{\partial \bar{p}}{\partial x_i} + \mu \Delta \bar{u}_i - \rho \left(\frac{\partial \overline{u'_i u'_j}}{\partial x_j} \right) + S_i \quad (2.9)$$

Where x, y, z is the Cartesian coordinate system, $\bar{u}, \bar{v}, \bar{w}$ is the mean velocity component, u', v', w' is the velocity fluctuation, t is time, ρ is density, p is the pressure, μ is the viscosity, $S_{x,y,z}$ is a source term and i, j represent components in the i, j th direction.

This process creates six new terms, which are commonly known as Reynolds stresses and denoted by $\tau_{ij} = -\rho \overline{u'_i u'_j}$. The problem is that this creates additional terms with no additional equations, creating an incomplete system and is often referred to

as the RANS closure problem. To close the system turbulence models are used to approximate the unknown terms.

Eddy-viscosity Turbulence models

There are many different turbulence models available, although there are two predominant classes of turbulence models used with RANS which attempt to calculate or approximate the Reynolds stresses. The first class is based on the eddy-viscosity assumption and the other is the Reynolds Stress Model (RSM).

The eddy-viscosity models vary with complexity and approximate the Reynolds stresses using the Boussinesq hypothesis also called the Boussinesq approximation and Boussinesq eddy-viscosity assumption. The Boussinesq hypothesis, proposed by Boussinesq [30], is a linear relation, shown in equation (2.10), between the stress tensor (τ_{ij}) and mean strain tensor (\mathbb{S}) and is analogous to the linear relation between the viscous stress tensor and viscosity [37]. It relates the Reynolds stresses to the velocity gradients through an eddy-viscosity, in an analogy to molecular viscosity, assuming that the Reynolds stress tensor is coincident with the mean rate tensor. The implications of this are detailed in many textbooks and publications including Wilcox [24] which states there is no physical basis for this assumption. In particular, Schmitt [37] analysed the validity of the hypothesis using databases as well as DNS and LES test cases and found that it is almost never verified. Despite this the eddy-viscosity is widely used to model turbulence and can perform well when used correctly.

$$\tau_{ij} = -\mu_T \mathbb{S} \quad (2.10)$$

$$\mathbb{S} = \frac{1}{2} \left(\frac{\partial \bar{u}_j}{\partial x_i} + \frac{\partial \bar{u}_i}{\partial x_j} \right) \quad (2.11)$$

Where \mathbb{R} is the stress tensor and \mathbb{S} is the mean strain tensor, μ_T is the eddy-viscosity,

\bar{u} is the mean velocity component, $x_{i,j}$ is the Cartesian coordinate system and i, j represent components in the i, j th direction.

There are numerous models which use the eddy-viscosity concept to different degrees. These models are divided into algebraic models, one equation models and two equations models.

Algebraic models

Algebraic or zero equation turbulence models are computationally the simplest models and often compute the eddy-viscosity in terms of the mixing length. The mixing length hypothesis was proposed by Prandtl in 1925 [38]. The hypothesis leads to defining the eddy-viscosity as:

$$\mu_T = \rho \ell_{mix}^2 \left| \frac{d\bar{u}}{dy} \right| \quad (2.12)$$

where μ_T is the eddy-viscosity, ρ is density and ℓ_{mix} is the mixing length.

The mixing length is empirical, depending on the flow and must be specified in advance. Therefore, by definition the algebraic models are incomplete turbulence models.

One equation models

One equation models calculate one turbulent transport equation, usually the turbulence kinetic energy. It is technically the specific turbulent kinetic energy as it is per unit mass, shown in equation (2.13), although it is commonly just called the turbulence kinetic energy. One equation models are incomplete as they normally relate the turbulence length scale to some flow parameter. The original one equation model was developed by Prandtl in 1945 [39]. Prandtl calculated the specific turbulent kinetic energy as shown in equation (2.14) and assumed that the turbulent dissipation (ϵ) was proportional to $k^{3/2}/\ell$. The turbulence length scale still needs to be defined in advance to close the system.

$$k = \frac{1}{2} \left(\overline{u'^2} + \overline{v'^2} + \overline{w'^2} \right) \quad (2.13)$$

$$\rho \frac{\partial k}{\partial t} + \rho \bar{u}_j \frac{\partial k}{\partial x_j} = \tau_{ij} \frac{\partial \bar{u}_i}{\partial x_j} - C \rho \frac{k^{3/2}}{\ell} + \frac{\partial}{\partial x_j} \left[\left(\mu + \frac{\mu_T}{\sigma_k} \right) \frac{\partial k}{\partial x_j} \right] \quad (2.14)$$

$$\mu_T = \rho k^{1/2} \ell \quad (2.15)$$

Where k is the specific turbulence kinetic energy, $x_{i,j}$ is the Cartesian coordinate system, \bar{u}_i is the mean velocity component, t is time, ρ is density, μ is the viscosity, μ_T is the eddy-viscosity, C, σ_k are closure coefficients, i, j represent components in the i, j th direction and ℓ is the turbulence length scale.

Since Prandtl's one equation model there have been many more models developed, most more elaborate than his. Prandtl's model only requires two closure coefficients (C, σ_k) whereas other have many more such as Baldwin-Barth model [40] which has seven closure coefficients and two damping functions and the Spalart-Allmaras model [41] which features eight closure coefficients and three damping functions.

Two equation models

Two equation models are complete, providing a closed system and are the simplest complete system used in CFD modelling. They calculate two equations: one for the specific turbulence kinetic energy and the other is related to the turbulence length scale. There are many different models, the main difference being the second equation and the variable calculated, including the turbulence length scale (ℓ), specific dissipation (ϵ) or specific dissipation rate (ω) [42][43]. The first two equation model was developed by Kolmogorov in 1942 [44] which was a k - ω model. All two equation models feature closure coefficients which have been used to replace double and triple correlation terms with algebraic expression involving known properties. If turbulence theory

was exact these coefficients would be set from first principles but it is not and the models are developed based on dimensional analysis and observations [24]. There are many models but the main models used today are the k - ϵ , k - ω and k - ω SST models, which are discussed in more detail.

The k - ϵ model

The k - ϵ model is the most popular model and in many cases the default model. It features equations of the specific turbulence kinetic energy (k) and the dissipation per unit mass (ϵ) often just referred to as the dissipation. It was first developed by Jones & Launder [28] and later improved by Launder and Sharma [45]. The model is so widely used it is normally referred to as the standard k - ϵ model or just the k - ϵ model without any references. The model defines k using equation (2.16) and ϵ using equation (2.17).

$$\rho \frac{\partial k}{\partial t} + \rho \bar{u}_j \frac{\partial k}{\partial x_j} = \tau_{ij} \frac{\partial \bar{u}_i}{\partial x_j} - \rho \epsilon + \frac{\partial}{\partial x_j} \left[\left(\mu + \frac{\mu_T}{\sigma_1^\epsilon} \right) \frac{\partial k}{\partial x_j} \right] \quad (2.16)$$

$$\rho \frac{\partial \epsilon}{\partial t} + \rho \bar{u}_j \frac{\partial \epsilon}{\partial x_j} = \alpha^\epsilon \frac{\epsilon}{k} \tau_{ij} \frac{\partial \bar{u}_i}{\partial x_j} - \beta^\epsilon \rho \frac{\epsilon^2}{k} + \frac{\partial}{\partial x_j} \left[\left(\mu + \frac{\mu_T}{\sigma_2^\epsilon} \right) \frac{\partial \epsilon}{\partial x_j} \right] \quad (2.17)$$

Where k is the specific turbulence kinetic energy, $x_{i,j}$ is the Cartesian coordinate system, \bar{u}_i is the mean velocity component, t is time, ρ is density, μ is the viscosity, μ_T is the eddy-viscosity, $\alpha^\epsilon, \beta^\epsilon, \sigma_1^\epsilon, \sigma_2^\epsilon$ are closure coefficients and i, j represent components in the i, j th direction.

This model has five closure coefficients which are $\alpha^\epsilon = 1.44, \beta^\epsilon = 1.92, \sigma_1^\epsilon = 1.0, \sigma_2^\epsilon = 1.3$ and $C_\epsilon = 0.09$. It also has two auxiliary relations which are that $\omega = \epsilon / (C_\epsilon k)$ and $\ell = C_\epsilon k^3 / \epsilon$. Equation 2.17 is only an approximation to the exact equation of the turbulence dissipation [24][46] which is shown in equation (2.18). The problem is that the exact equation is too difficult to solve as it introduces several new unknowns.

$$\begin{aligned}
\frac{\partial \varepsilon}{\partial t} + \bar{u}_j \frac{\partial \varepsilon}{\partial x_j} &= -2\nu [\overline{u'_{i,j} u'_{j,k} \bar{u}_{j,k}} + \overline{u'_{k,i} u'_{k,j} \bar{u}_{i,j}}] - 2\nu \overline{u'_j u'_{i,k} \bar{u}_{i,jk}} \\
&\quad - 2\nu \overline{u'_{i,j} u'_{j,k} u'_{k,i}} - 2\nu^2 \overline{u'_{i,jj} u'_{i,kk}} \\
&\quad + \nu \frac{\partial \varepsilon}{\partial x_j} - \nu \overline{u'_{i,k} u'_{i,k} u'_j} - 2\nu \overline{p'_k u'_{j,k}}
\end{aligned} \tag{2.18}$$

The k - ε model does have a number of flaws and limitations, which are well documented such as performing badly with severe pressure gradients and separation [24][29]. To this extent there have been a large number of modifications to the standard model to improve it. The most commonly used of these are: RNG k - ε model and realizable k - ε model. The RNG k - ε model or Renormalization Group Method k - ε model adds a term to the turbulence dissipation equation to account for the interaction between the dissipation and mean shear. The realizable k - ε model changes one of the closure coefficients (C_ε) to allow it to vary based on the velocity gradients.

The k - ω model

There are a number of methods that use the specific dissipation rate (ω). The most common k - ω model is often referred to as the standard k - ω model or the Wilcox k - ω model [24][47]. This model defines k using equation (2.19) and ω using equation (2.20).

$$\rho \frac{\partial k}{\partial t} + \rho \bar{u}_j \frac{\partial k}{\partial x_j} = \tau_{ij} \frac{\partial \bar{u}_i}{\partial x_j} - \beta_1^\omega \rho k \omega + \frac{\partial}{\partial x_j} \left[(\mu + \sigma_1^\omega \mu_T) \frac{\partial k}{\partial x_j} \right] \tag{2.19}$$

$$\rho \frac{\partial \omega}{\partial t} + \rho \bar{u}_j \frac{\partial \omega}{\partial x_j} = \alpha^\omega \frac{\omega}{k} \tau_{ij} \frac{\partial \bar{u}_i}{\partial x_j} - \beta_2^\omega \rho \omega^2 + \frac{\partial}{\partial x_j} \left[(\mu + \sigma_2^\omega \mu_T) \frac{\partial \omega}{\partial x_j} \right] \tag{2.20}$$

Where k is the specific turbulence kinetic energy, $x_{i,j}$ is the Cartesian coordinate system, \bar{u}_i is the mean velocity component, t is time, ρ is density, μ is the viscosity, μ_T

is the eddy-viscosity, ω is the specific dissipation rate $\alpha^\omega, \beta_1^\omega, \beta_2^\omega, \sigma_1^\omega, \sigma_2^\omega$ are closure coefficients and i, j represent components in the i, j th direction.

This model has five closure coefficients which are $\alpha^\omega = 5/9$, $\beta_1^\omega = 9/100$, $\beta_2^\omega = 3/40$, $\sigma_1^\omega = 1/2$ and $\sigma_2^\omega = 1/2$. It also has two auxiliary relations which are $\varepsilon = \beta_1^\omega \omega k$ and $\ell = k^{1/2}/\omega$. It is known to perform better under adverse pressure gradients and for flows featuring separation than the k - ε model. It is also considered more accurate within the wall region [48]. Although it has been shown to be more sensitive to free stream velocities at the boundary layer edge

The k - ω SST model

The k - ω shear stress transport model normally written k - ω SST or SST k - ω model is a combination of the standard k - ω and k - ε models defined by Menter [29][49][50]. The k - ω SST model is a variation and improvement of the baseline (BSL) model. The BSL model varies between the k - ω and k - ε models in an almost linear manner whereas the k - ω SST model also accounts for the turbulent shear stress. It uses the k - ω definition in the inner part of the boundary layer and the k - ε definition outside the boundary layer.

Menter [29] created one set of equations by blending the k - ω and k - ε model equations, by first transforming the k - ε model into a k - ω formulation, shown in equation (2.21).

$$\begin{aligned} \rho \frac{\partial \omega}{\partial t} + \rho \bar{u}_j \frac{\partial \omega}{\partial x_j} = & \alpha^{\omega\varepsilon} \frac{\omega}{k} \tau_{ij} \frac{\partial \bar{u}_i}{\partial x_j} - \beta_2^{\omega\varepsilon} \rho \omega^2 + \frac{\partial}{\partial x_j} \left[(\mu + \sigma_2^{\omega\varepsilon} \mu_T) \frac{\partial \omega}{\partial x_j} \right] \\ & + 2\rho \sigma_2^{\omega\varepsilon} \frac{1}{\omega} \frac{\partial k}{\partial x_j} \frac{\partial \omega}{\partial x_j} \end{aligned} \quad (2.21)$$

Where $\alpha^{\omega\varepsilon}, \beta_1^{\omega\varepsilon}, \beta_2^{\omega\varepsilon}, \sigma_1^{\omega\varepsilon}, \sigma_2^{\omega\varepsilon}$ are the new closure coefficients and all other variables are as previously defined. The two models are combined to create a new set of equations for k and ω as shown in equations (2.22) and (2.23).

$$\rho \frac{\partial k}{\partial t} + \rho \bar{u}_j \frac{\partial k}{\partial x_j} = \tau_{ij} \frac{\partial \bar{u}_i}{\partial x_j} - \beta_1^{sst} \rho k \omega + \frac{\partial}{\partial x_j} \left[(\mu + \sigma_1^{sst} \mu_T) \frac{\partial k}{\partial x_j} \right] \quad (2.22)$$

$$\begin{aligned} \rho \frac{\partial \omega}{\partial t} + \rho \bar{u}_j \frac{\partial \omega}{\partial x_j} &= \alpha^{sst} \frac{\omega}{k} \tau_{ij} \frac{\partial \bar{u}_i}{\partial x_j} - \beta_2^{sst} \rho \omega^2 + \frac{\partial}{\partial x_j} \left[(\mu + \sigma_2^{sst} \mu_T) \frac{\partial \omega}{\partial x_j} \right] \\ &+ 2\rho(1 - F_1) \sigma_2^{sst} \frac{1}{\omega} \frac{\partial k}{\partial x_j} \frac{\partial \omega}{\partial x_j} \end{aligned} \quad (2.23)$$

Where $\alpha^{sst}, \beta_1^{sst}, \beta_2^{sst}, \sigma_1^{sst}, \sigma_2^{sst}$ are the new combined closure coefficients, F_1 is the blending function and all other variables are as previously defined.

A blending function (F_1) is used to gradually change between the two methods in the desired regions. It is designed so that the k - ω formulation is used in the near wake region and the k - ϵ formulation is used in the free shear layers. With the coefficients also blended using equation (2.24)

$$\phi_{sst} = F_1 \phi_\omega + (1 - F_1) \phi_\epsilon \quad (2.24)$$

where ϕ_{sst} represents the variables used in the k - ω SST model (α^{sst}, \dots), ϕ_ω represents the variables used in the k - ω model (α^ω, \dots) and ϕ_ϵ represents the variables used in the transformed k - ϵ model ($\alpha^{\omega\epsilon}, \dots$).

The blending function is based on a set of logical arguments and utilizes both spatial and fluid terms as shown in equation (2.25).

$$F_1 = \tanh \left(\left(\min \left(\max \left(\frac{\sqrt{k}}{0.09\omega y_s}; \frac{500\nu}{y_s^2 \omega} \right); \frac{4\rho\sigma_2^{\omega\epsilon} k}{CD_{kw} y_s^2} \right) \right)^4 \right) \quad (2.25)$$

$$CD_{kw} = \max \left(2\rho\sigma_2^{\omega\epsilon} \frac{1}{\omega} \frac{\partial k}{\partial x_j} \frac{\partial \omega}{\partial x_j}, 10^{-10} \right) \quad (2.26)$$

Where k is the specific turbulence kinetic energy, ω is the specific dissipation rate,

y_s is the distance to the nearest surface, ρ is the density, ν is the kinematic viscosity, $\sigma_2^{\omega\epsilon}$ is a closure coefficient and CD_{kw} is the cross diffusion term.

The three terms in equation (2.25) correspond to arguments related to the turbulent length scale, viscous sublayer and small free stream values. The limiter has a factor of 10 in this formulation in line with the latest improvements [50] instead of 20 as initially proposed [29][49].

The advantage of the k - ω SST model over the BSL model is that it accounts for the turbulence shear stress by limiting the eddy-viscosity as shown in equation (2.27). It is limited based on the assumption that the turbulent shear stress is proportional to the specific turbulence kinetic energy in the logarithmic and wake regions of the turbulence boundary layer [51].

$$\mu_T = \frac{\rho a_1 k}{\max(a_1 \omega, S F_2)} \quad (2.27)$$

$$F_2 = \tanh \left(\left(\max \left(2 \frac{\sqrt{k}}{0.09 \omega y_s}; \frac{500 \nu}{y_s^2 \omega} \right) \right)^2 \right) \quad (2.28)$$

Where μ_T is the eddy-viscosity, a_1 is a constant equal to 0.31, k is the turbulence kinetic energy, ω is the specific dissipation rate, S is the invariant measure of the strain rate, F_2 is the second blending function, y_s is the distance to the nearest surface, ρ is the density and ν is the kinematic viscosity.

The k - ω SST model is an improvement over the other two equation models for many flow situations, although it is limited by the use of the eddy-viscosity and Boussinesq hypothesis. These models assume isotropic turbulence, which is not normally valid and can cause unrealistic results.

Near wall region

For turbulent flow conditions, the velocity profile can be split into two regions: the viscous sublayer and the inertial layer. The location of the outer edge of the inertial layer depends on the Reynolds number. The extent of the inertial layer grows with increasing Reynolds number.

To fully resolve the boundary layers in the near wall region requires excessive grid resolution. It requires the first computational cell from the wall be located within the viscous sublayer and achieve $y^+ = 1$, shown in equation (2.29). Wall functions are used to significantly reduce computational expense by reducing the grid resolution and modelling the flow using semi-empirical functions, shown in Figure 2.1. A corresponding wall function grid can have a the first cell with a $y^+ = 100$ [52]. There are many different wall functions available, used for different turbulence models. Wall functions will not be discussed here in detail as the topic is too vast, only a brief summary of their implications. For more information see the references [52].

$$y^+ \equiv \frac{U^* y_d}{\nu} \quad (2.29)$$

Where U^* is the friction velocity at the wall, y_d is the distance to the nearest wall and ν is the local kinematic viscosity of the fluid.

For the $k-\omega$ model, an analytical expression is known for the viscous sublayer and there is an approximation for the logarithmic layer[52]. Whereas for the $k-\epsilon$ model there is no analytical expression for the viscous sublayer. This means the wall function needs to approximate the entire boundary layer. Many functions assume the first grid point is within the fully turbulent log-law region which has a significant impact on the result and is not always the case and is why the $k-\omega$ model is more accurate for wall bounded simulations.

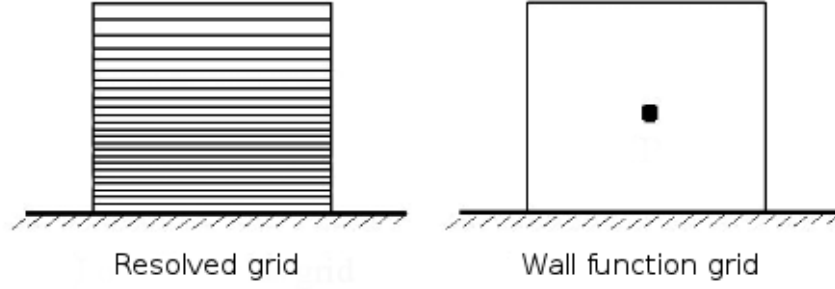


Figure 2.1: Difference in grid resolution using a wall function

Reynolds Stress Model

The Reynolds Stress Model (RSM) also known as a second moment closure model, closes the Reynolds-Averaged Navier-Stokes equations without relying on the Boussinesq hypothesis. Instead, it solves additional transport equations for all components of the Reynolds stress tensor (τ_{ij}). However, the derivation of the RSM requires higher order correlations to be modelled. RSM avoids the isotropic eddy-viscosity assumption allowing the full 3D nature of turbulence to be modelled. This added accuracy requires additional computational resources to solve the additional equations.

Nearly all RSMs start from the same point, the exact differential equation of the Reynolds stress tensor as shown in equation (2.30).

$$\frac{\partial \tau_{ij}}{\partial t} + \bar{u}_k \frac{\partial \tau_{ij}}{\partial x_k} = -\tau_{ik} \frac{\partial \bar{u}_j}{\partial x_k} - \tau_{jk} \frac{\partial \bar{u}_i}{\partial x_k} + \epsilon_{ij} - \Pi_{ij} + \frac{\partial}{\partial x_k} \left[\nu \frac{\partial \tau_{ij}}{\partial x_k} + C_{ijk} \right] \quad (2.30)$$

$$\epsilon_{ij} = 2\nu \overline{\frac{\partial u'_i}{\partial x_k} \frac{\partial u'_j}{\partial x_k}} \quad (2.31)$$

$$\Pi_{ij} = p' \overline{\left(\frac{\partial u'_i}{\partial x_j} + \frac{\partial u'_j}{\partial x_i} \right)} \quad (2.32)$$

$$C_{ijk} = \overline{p u'_i u'_j u'_k} + \overline{p' u'_i} \delta_{jk} + \overline{p' u'_j} \delta_{ik} \quad (2.33)$$

Where ϵ_{ij} is the dissipation tensor, Π_{ij} is the pressure-strain correlation tensor, C_{ijk} is the turbulent transport tensor, δ_{ij} is the Kronecker delta and all other variables are as previously described.

To close the equations, three tensors (dissipation tensor (ϵ_{ij}), pressure-strain correlation tensor (Π_{ij}) and the turbulent transport tensor (C_{ijk})) needs to be modelled. Rotta [53] was the first to develop a closure of the Reynolds stress equation in 1951. There are many different approaches to modelling the tensors and some are based on similar methods and equations used in the eddy-viscosity turbulent models. Of the three tensors Π_{ij} has received the most attention, this is because it has a similar magnitude to the production term, so has a critical role in the flow and it is essentially unmeasurable [24].

RSM is good for accurately predicting complex flows as it accounts for streamline curvature, swirl, rotation and high strain rates. Although it does struggle with stability without the eddy viscosity term and has a higher computational expense (2 – 3 times) compared to the other turbulence models.

2.1.2 Large Eddy Simulations

The Large Eddy Simulations (LES) computes the large eddies and models the smallest eddies. The large eddies are dependent on the boundary conditions and geometry so need to be calculated. However, the small eddies are nearly isotropic with more universal characteristics allowing them to modelled [24]. The small eddies are modelled by subgrid scale (SGS) models.

The differentiation between the large eddies (resolved) and the small eddies (modelled) of the flow field are accomplished using a filtering method. The filtering process effectively filters out eddies smaller than the filter width. A common filtering method decomposes a flow variable ($\psi(x, t)$) into the large scale filtered part ($\bar{\psi}(x, t)$) and small

scale sub-filtered part ($\psi'(x, t)$):

$$\psi(x, t) = \bar{\psi}(x, t) + \psi'(x, t) \quad (2.34)$$

The filtered variable is defined at x_0 as:

$$\bar{\psi}(x_0) = \int_{\Theta} \psi(x, t) G(\Delta) dx' \quad (2.35)$$

where Θ is the fluid domain, G is the filter function.

The filter function depends on the filter width $\Delta = (\Delta_1 \Delta_2 \Delta_3)^{1/3}$ where Δ_i is the filter width in the i th direction. There are a number of different filtering functions, the most common are the Gaussian filter (equation (2.36)), the tophat or box filter (equation (2.37)) and cut-off filter (equation (2.38)).

$$G = \left(\frac{6}{\pi \Delta^2} \right)^{3/2} \exp \left(-6 \frac{|x_0 - x|^2}{\Delta^2} \right) \quad (2.36)$$

$$G = \begin{cases} \frac{1}{\Delta} & \text{if } |x_0 - x| \leq \frac{\Delta_i}{2} \\ 0 & \text{otherwise} \end{cases} \quad (2.37)$$

$$G = \prod_{i=1}^3 \frac{\sin \left(\frac{\pi}{\Delta_i} (x_0 - x) \right)}{\pi (x_0 - x)} \quad (2.38)$$

Whichever filtering function is used it is applied to the Navier-Stokes equations to create filtered equations, as shown in equations (2.39) and (2.40), which are solved in LES simulations.

$$\frac{\partial \bar{U}_i}{\partial x_i} = 0 \quad (2.39)$$

$$\frac{\partial \bar{U}_i}{\partial t} + \frac{\partial}{\partial x_j} (\bar{U}_i \bar{U}_j) = -\frac{1}{\rho} \frac{\partial \bar{P}}{\partial x} - \frac{\partial \tau_{sgs}}{\partial x_j} + \nu \frac{\partial^2 \bar{U}_i}{\partial x^2} + S_i \quad (2.40)$$

Where \bar{U}_i is the large scale filtered component and τ_{sgs} is the subgrid scale stress term.

Subgrid scale models

Most subgrid scale models are eddy-viscosity models using the Boussinesq hypothesis. The most widely used models are based on the Smagorinsky model [32] which uses an algebraic eddy-viscosity. This has been used due to its simplicity as the SGS eddy-viscosity (μ_{sgs}) is determined by:

$$\mu_{sgs} = \rho (C_S \Delta)^2 \sqrt{2 \bar{S}_{ij} \bar{S}_{ij}} \quad (2.41)$$

where \bar{S}_{ij} is the rate-of-strain tensor for the resolved scale, C_S is the Smagorinsky constant usually varying between 0.1 to 0.2.

Of the models based on the Smagorinsky model [32] the most commonly used is the Smagorinsky-lilly model [33][34] which uses a modified SGS eddy-viscosity given by:

$$\mu_{sgs} = \rho L_S^2 \sqrt{2 \bar{S}_{ij} \bar{S}_{ij}} \quad (2.42)$$

$$L_S = \min(\kappa y_d, C_s V^{1/3}) \quad (2.43)$$

where L_S is the mixing length for the SGS, κ is the von Karman constant, y_d is the distance to the closest wall, C_s is the Smagorinsky constant, and V is the volume of the computational cell.

One problem with these models is that C_s is not universal. Lilly [33][34] derived a value of 0.17 for homogeneous isotropic turbulence. However, this can cause excessive dampening near solid boundaries and a value of around 0.1 has been found to yield the best results for a wide range of flows [54].

LES is a transient method, requiring time discretization and definition of a time-step. This is normally defined to maintain stability and to accurately resolve turbulence in time. The most common condition is the Courant–Friedrichs–Lewy (CFL) condition [55] that requires:

$$\left| \frac{u\Delta t}{\Delta x} \right| \leq 1 \quad (2.44)$$

where Δt is the time step and Δx is the spatial step.

For more information about LES, the SGS models and its applications see the references [24][35][36][56][57][58].

2.1.3 Detached Eddy Simulation

Detached Eddy Simulation (DES) is a hybrid method which combines LES and RANS. As LES becomes extremely computationally expensive within the near wall region, one method used to reduce this expense is to use another formulation. DES uses the LES formulation for the majority of the domain and switches to the RANS formulation near wall boundaries. The switch between the two formulations can be accomplished using turbulence length scales, distance variables or specified by the user within certain zones known as zonal DES [59]. DES is only in its infancy as it was first proposed in 1997 [60], for more information on DES, its history and applications see the reference

[61].

2.1.4 Direct Numerical Simulations

Direct Numerical Simulations (DNS) solves the Navier-Stokes equations for all scales of motion without any averaging or approximation. To capture all the turbulence scales the small scales need to be captured as these are responsible for the turbulence dissipation and the Kolmogorov scale (η) is commonly considered as the smallest scale that needs to be resolved, although this is not always the case [62].

This need to resolve all length scales means that the number of grid points required are in the order of $Re^{9/4}$. Equally, the simulation must be time dependent and given that the Kolmogorov time-scale is proportional to $Re^{1/2}$ this results in an overall computational time of $Re^{11/4}$. This shows the dependence and limitation of DNS on the Re and why only low Re flows have been simulated. For example, if $Re = 10^6$ (reasonable for many applications such as in the aerospace industry) the grid would need to contain approximately $10^{13.5}$ (3162 billion) points, which is not possible considering the current computational resources. In comparison, LES requires grids in the order of $Re^{1.8}$ [36] which results in LES typically requiring 5-10% the CPU time needed for analogous DNS [24]. Despite the high computational requirements DNS is still an important tool for CFD, particularly in regards to understanding turbulence and improving turbulence models.

For more information on the DNS, applications and previous work see the references [24][35][57][62].

2.1.5 Discretization

Computers do not solve the equations of motion in differential form, but in a discretized form. The discretization process which is also referred to as meshing or grid generation, involves dividing the continuous fluid domain into discrete points (also called nodes, or vertices) and volumes (cells or elements). There are two types of grid:

- structured grids are created with each grid point being uniquely defined by indices i,j,k and are made up of hexahedral cells;
- unstructured grids are created with points that have no particular ordering. The grid cells are commonly tetrahedral cells, although they can be made up of various cells including tetrahedral, hexahedral, prisms, pyramids and wedges such grids are known as hybrid or mixed grids.

The advantage of a structured grid is that it is easy to relate cells and their neighbours, which allows data to quickly and easily be calculated by adding or subtracting indices by an integer. This is also a disadvantage when considering complex geometry that can not be regularly divided. One approach to address this is known as the multiblock approach which divides the geometry into smaller parts or blocks which can be discretized easier. This can create what is known as hanging nodes where nodes only exist on one side of these block boundaries. Another approach is known as the overset or chimera method where grids are created around boundaries independently and then overlapped. The important part of this approach is in transferring the data between grids within the overlapping region.

The unstructured grids are more flexible and can be generated more easily due to the use of tetrahedral cells. However, it is common to use hexahedral and prism cells to resolve the boundary layer. Another advantage is they can handle refinement and coarsening with ease. The main disadvantage is that they require more complex data

structures to keep track of cells and their connections. This leads to higher memory requirements compared to structured grids.

Once the domain has been discretized to form a grid the equations need to be discretized. There are three main processes of discretization used; the Finite Difference method (FDM), Finite Element Method (FEM) and Finite Volume Method (FVM).

Finite Difference Method

The Finite Difference Method (FDM) was among the first methods and was utilized by Euler [35]. It is directly applied to the differential equations using the Taylor series expansion to discretize the flow variables. The advantage of this method is its simplicity and ease to obtain high order approximations and hence accuracy. The disadvantage is that it requires a structured grid and can not be applied to body fitted grids which limits its applications. For more details on this method see the reference [35].

Finite Element Method

The Finite Element Method (FEM) was originally developed for structural analysis, proposed in 1956 by Turner *et al.* [63]. It can accommodate an unstructured mesh and the grid nodes are exclusively used to produce an arbitrarily high order of accuracy representation of the solution on smooth grids [35]. It works with an equivalent integral form of the governing equations, commonly accomplished based on the weak formulation. As this method uses an integral formulation and an unstructured grid, it is preferable for flows featuring complex geometry and is particularly suitable for non-Newtonian fluids. The finite element methods have a very rigorous mathematical foundation but can be shown to be mathematically equivalent to the finite volume method for certain cases and have a higher numerical expense.

Finite Volume Method

The Finite Volume Method (FVM) was first employed in 1971 by McDonald [64] for 2D flows and directly uses the integral formulation of the Navier-stokes equations. It discretizes the domain into control volumes on which the surface integral is calculated. The accuracy of the discretization depends on the schemes used to define the control volumes. As part of this methods there are two different schemes used to define the shape and position of the control volume: the cell-centred scheme and the cell-vertex scheme.

The cell-centred scheme has the control volumes identical to the grid cells and the flow variables are stored at the centre of the cells (shown in Figure 2.2(a)). The variables are calculated using the average of the fluxes computed from the values of the cells to the left and to the right.

The cell-vertex scheme stores the variables at the grid points and can either have the control volume as the sum of the cells sharing a grid point (overlapping control volumes shown in Figure 2.2(b)) or the volume centred around a grid point (dual control volumes shown in Figure 2.2(c)) [35]. For the overlapping scheme the control volumes are the cells but the variables are calculated at the vertex based on the surrounding cells. The dual control volume scheme stores all variables at the node, with the control volume constructed based on the midpoints of the cells surrounding the node, shown in Figure 2.2(c).

Comparing the two schemes, the cell-centred scheme depend strongly on the smoothness of the grid which can cause numerical errors that does not effect the vertex-centred schemes. However, both schemes can reach second or higher order accuracy if the grid is sufficiently smooth. The dual control volume scheme experiences difficulties at the boundary of solid walls as the node is on the wall which leads to discretization errors compared to the cell-centred scheme. For unstructured grids the cell-centred scheme

leads to approximately six times as many control volumes using tetrahedral and approximately three times as many when using a mixed grid compared to the cell-vertex scheme. This suggests the cell-centred is more accurate, although it calculates the variables from approximately half the number of points and the additional control volumes result in additional computational expense, providing no clear advantage. The cell-centred scheme requires approximately twice as much memory as it needs to store more flow variables. Using hexahedral grids the two schemes are computationally equivalent.

The FVM is very flexible and can be implemented on structured and unstructured grids. It can be shown to be equivalent to both the FDM and FEM methods for certain cases. Due to its flexibility it is the most widely used discretization process.

2.2 Rotor models

This section details the rotor models used as part of this thesis including a porous disc and actuator methods. It begins with descriptions of each rotor model used in this work and their underpinning theory. Followed by their implementation within the commercially available optimized Computational Fluid Dynamics (CFD) codes ANSYS-CFX [65] and ANSYS-Fluent [66].

2.2.1 Porous disc

A porous disc is one of the simplest models used to represent (renewable energy) turbines. These commonly feature predefined momentum losses. Similar approaches can also be described using analogous equations such as momentum sinks and drag discs. All approaches feature the same diameter as the turbine with a thin depth/thickness. The disc needs a thickness to avoid singularities caused by discontinuities in the pressure and velocity fields.

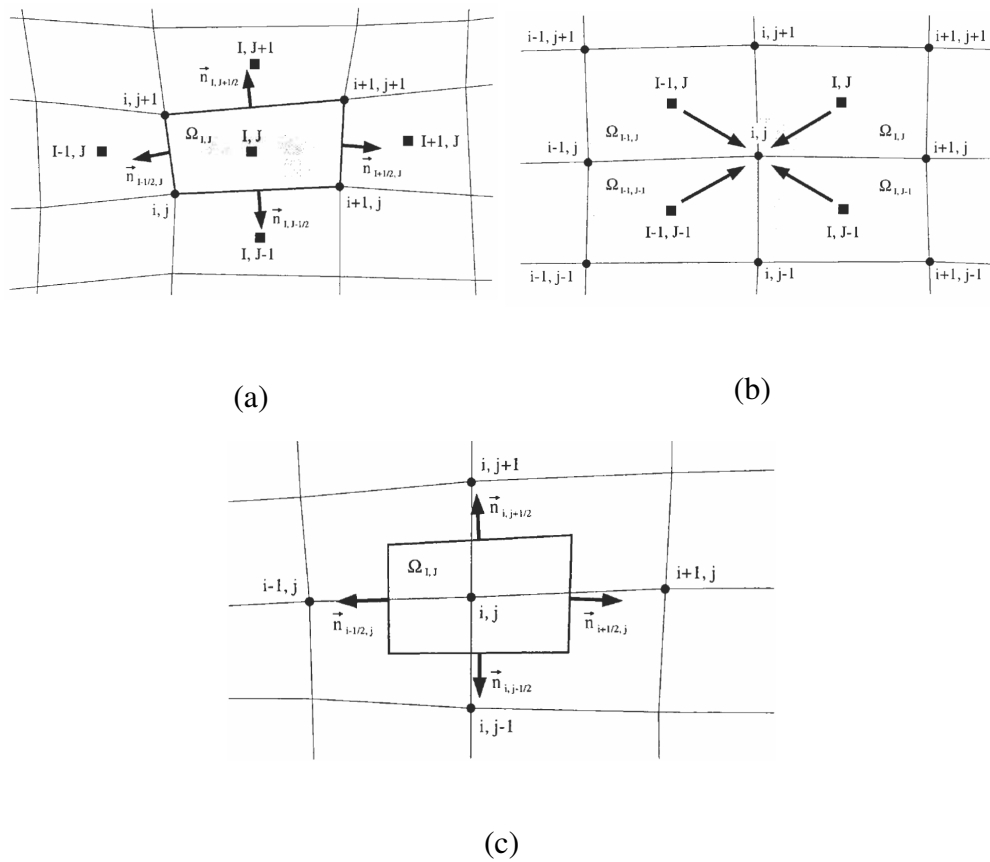


Figure 2.2: Control volumes of (a) the cell-centred scheme, (b) the cell-vertex scheme (overlapping) and (c) the cell-vertex scheme (dual control volumes) [35]

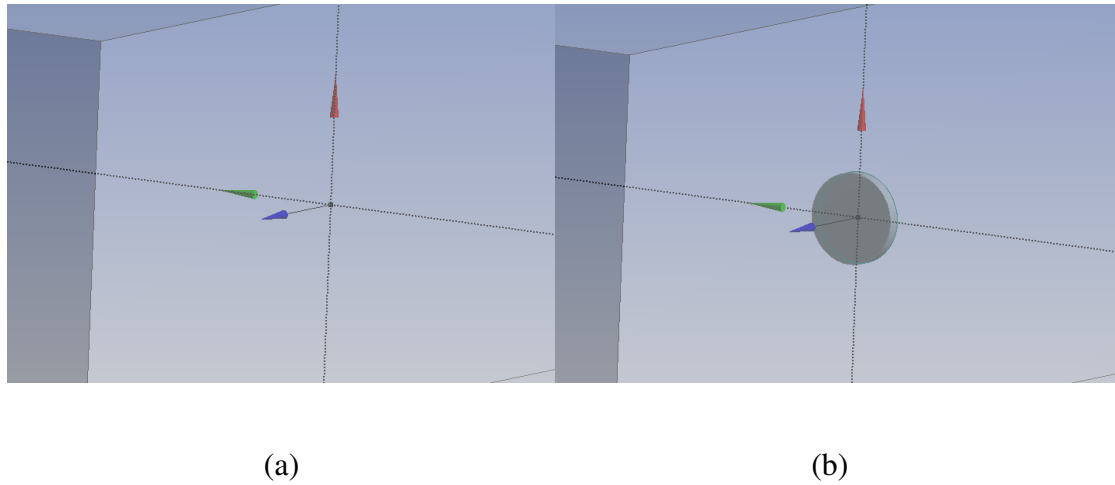


Figure 2.3: Geometry of two methods used to define disc location a) algebraically b) geometrically

Implementation

There are two methods that can be used to define the disc location: either algebraically as part of the solver set-up, which is described in subsection 2.2.2 or geometrically by creating the disc as part of the geometry. Figure 2.3 shows the difference in geometry for these two methods. If the disc is constructed geometrically then the shape and size of the disc needs to be defined before the domain is discretized. It is then possible to define the disc as a subdomain or cell zone for the source terms to be applied to.

ANSYS-CFX

The subdomain concept is used within ANSYS-CFX to define porous media. There are multiple ways to impose a porous loss, for example using permeability and/or a loss coefficient for (an)isotropic loss media. Within this thesis the loss coefficient and directional loss model were used to model an isotropic momentum loss. In ANSYS-CFX the directional loss model adds a momentum source term to the flow, given by:

$$S = -K \frac{\rho}{2} u |u| \quad (2.45)$$

where K is defined by the user and referred to as the *resistance coefficient* within ANSYS-CFX, ρ is the density and u is the velocity. The resistance is applied as a loss across the disc thickness and so specified by the user as $\frac{K}{d}$, where d is the thickness of the disc. The equation features $u|u|$ to define the source term as a vector in the direction of the flow.

ANSYS-Fluent

ANSYS-Fluent uses *cell zones* analogous to the aforementioned subdomain used in ANSYS-CFX. A cell zone can be used to define a porous media which is modelled using an additional momentum source term, shown in equation (2.46), which is divided into two components: a viscous loss term (linear) and inertial loss term (quadratic).

$$S_i = - \left(\sum_{i=1}^3 C_1 \mu u_i + \sum_{i=1}^3 C_2 \frac{1}{2} \rho u_i |u| \right) \quad (2.46)$$

$$S_i = -C_2 \frac{1}{2} \rho u |u| \quad (2.47)$$

Where S_i is the source term for the i th momentum equation, μ is the fluid viscosity, u is the velocity and C_1 and C_2 are prescribed matrices. The momentum sink contributes to the pressure gradient in the porous zone, creating a pressure drop that is proportional to the fluid velocity squared in the cell [54]. For a simple homogeneous porous media in one direction, the permeability term can be eliminated ($C_1 = 0$) [54], equation (2.46) becomes equation (2.47) which is analogous to equation (2.45) used by ANSYS-CFX. Similarly, the resistance is applied as a loss across the disc thickness and so specified as $\frac{C_2}{d}$, where d is the thickness of the disc.

2.2.2 Actuator disc method

The most common way to represent the rotor is by using actuator methods, where the blades are represented by body forces defined on either a disc, line or surface. The Actuator Disc Method (ADM) represents a time averaged rotor using forces distributed over a disc with the same dimensions and volume as the swept volume of the rotor. There are a number of variations of the ADM within the literature including constantly and variably loaded discs, as well as variations with and without rotation [67][68][69]. The forces acting on the flow are determined by the aerofoil characteristics and the local flow velocities. The aerofoil characteristics of thrust (C_T), lift (C_L) and drag (C_D) coefficients (discussed in subsections 3.1.1 and 3.1.3) are commonly determined from 2D tabulated data based on the local angle of attack (α), which is defined by equation (2.48), and the Reynolds number (§§1.5.2). The relative velocity of the flow to the aerofoil (U_{rel}) is defined by equation (2.50) with the angle between the relative velocity and the rotor plane (ϕ) given by equation (2.49) and shown in Figure 2.4.

$$\alpha = \phi - \gamma \quad (2.48)$$

$$\phi = \tan^{-1} \left(\frac{V_z}{\Omega r - V_\theta} \right) \quad (2.49)$$

$$U_{rel} = \sqrt{V_z^2 + (\Omega r - V_\theta)^2} \quad (2.50)$$

Where γ is the local pitch angle, r is the radius, V_z is the axial velocity, Ω is the rotational speed of the rotor defined by the user and V_θ is the tangential velocity.

There are a number of variations, each of which defines the force and source terms used slightly differently. The base term of each variation is defined using equation (2.51). It is possible to define the disc using the thrust coefficient [70][71][72] to create a uniformly loaded disc using equation (2.52) defined as a force per unit volume.

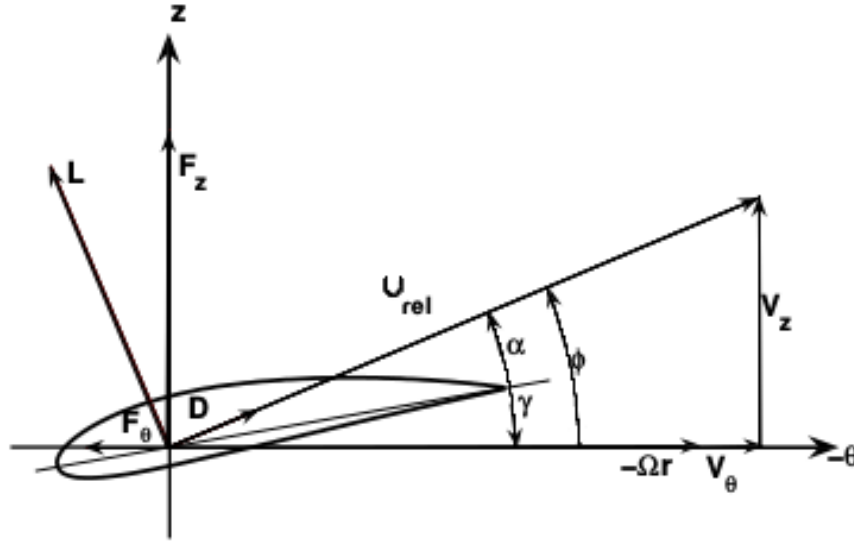


Figure 2.4: Aerofoil cross-section showing force vectors

A non-uniformly loaded or variably loaded disc can be defined using equation (2.53) where the variation is created by including the chord length (c) of the blades; creating a variation with radial position which is constant over each annulus. However, it is more common to define the disc based on the lift [73] or lift and drag coefficients [74][75] as shown in equations (2.54)-(2.56) respectively.

$$f = \frac{1}{2}\rho U_{rel}^2 \quad (2.51)$$

$$D_{ADUT} = \frac{1}{2}\rho U_{rel}^2 C_T B = f C_T B \quad (2.52)$$

$$D_{ADVT} = \frac{1}{2}\rho U_{rel}^2 C_T B c = f C_T B c \quad (2.53)$$

$$D_{ADL} = \frac{1}{2}\rho U_{rel}^2 C_L B c = f C_L B c \quad (2.54)$$

$$D_{ADLD} = \frac{1}{2}\rho U_{rel}^2 B c (C_{LeL} + C_{LeD}) \quad (2.55)$$

$$= f B c (C_{LeL} + C_{LeD}) \quad (2.56)$$

Where ρ is the density of air, U_{rel} is the relative velocity of the rotor, C_T is the thrust coefficient, B is the number of blades, c is the chord length, C_L is the lift coefficient, C_D is the drag coefficient and e_L, e_D are unit vectors used to define the direction of lift and drag respectively. The subscript abbreviations stand for Actuator Disc Uniform Thrust (ADUT), Actuator Disc Variable Thrust (ADVT), Actuator Disc Lift (ADL) and Actuator Disc Lift and Drag (ADLD).

Whichever definition term (D_n given in equation (2.52) - (2.56)) is used, it is then averaged over each annulus given in equation (2.57) for 3D or 2D by neglecting d in equation (2.57). The inclusion of lift (C_L) and drag (C_D) coefficients and their unit vectors (e_L, e_D) allows for rotational effects to be included by adding tangential forces as well as axial forces to the disc. It has been shown that the inclusion of rotation significantly improves predictions [68][69][76]. Porté-Agel *et al.* [77] showed that non rotational methods over predict turbulence intensity at the centre and under predict it at the top of the wake. The force per volume is commonly applied to the flow in cylindrical coordinates as a source term [73], as shown in equations (2.58)-(2.60), within the Navier-Stokes equations as discussed in section 1.5.

$$D_{AD} = \frac{D_n}{2\pi r d} \quad (2.57)$$

$$S_x = D_{AD}(C_L \cos \phi + C_D \sin \phi) \quad (2.58)$$

$$S_\theta = D_{AD}(C_L \sin \phi - C_D \cos \phi) \quad (2.59)$$

$$S_r = 0 \quad (2.60)$$

Where D_n is the disc definition term (given in equation (2.52) - (2.56)), r is the radius, d is the depth of the rotor, C_L is the lift coefficient, C_D is the drag coefficient, ϕ

is the angle between U_{rel} and rotor plane, defined in equation (2.49).

Tip loss correction

Use of a disc creating the assumption of an infinite number of blades neglects the fact that towards the edge of the disc the air tends to flow around the tip of the blade surface, thus reducing lift and hence power extraction at the tip. This is known as the tip loss effect and is commonly addressed using a factor referred to as the tip-loss correction factor or tip-loss factor. There have been a number of different factors and methods suggested within the literature [78][79][80]. It is suggested that the correction is applied to either the circulation, induced velocities, thrust coefficient or airfoil coefficients [79].

The best known correction factor is Prandtl's tip-loss function or correction factor [81], given in equation (2.61), which corrects the induced velocities which affect the loads indirectly. However, it leads to a slight over-prediction of the tip loads when using two-dimensional data with BEM, which is due to a three-dimensional effect of the blade geometry that is not taken into account [80]. Another popular tip correction method is Glauert's correction, given in equation (2.62). There are a number of semi-empirical correction factors presented in the literature, such as Xu and Sankar [82], Lindenburg [83] and Sant [84], which were based on the NREL phase VI experiment [85] (§§3.2.1). The most popular correction was presented by Shen *et al.* [78] and given in equation (2.63). Each tip-loss correction is applied in different ways. The most commonly used method is to apply it to the definition equation of the disc given in equation (2.51) or to the aerodynamics coefficients [73].

$$F_P = \frac{2}{\pi} \arccos \left[\exp \left(-\frac{B}{2} \frac{R-r}{R \sin(\phi)} \right) \right] \quad (2.61)$$

$$F_G = \frac{2}{\pi} \arccos \left[\exp \left(-\frac{B}{2} \frac{R-r}{r \sin(\phi)} \right) \right] \quad (2.62)$$

$$F_S = \frac{2}{\pi} \arccos \left[\exp \left(-g \frac{B}{2} \frac{R-r}{R \sin(\phi)} \right) \right] \quad (2.63)$$

$$g = \exp[-c_1(B\lambda - c_2)] + c_3 \quad (2.64)$$

Where F_P , F_G and F_S are correction factors, $c_{1,2,3}$ are constants with c_1, c_2 fitted from experimental data and c_3 empirically such that $(c_1, c_2, c_3) = (0.125, 21, 0.1)$.

Implementation in ANSYS-CFX

This section describes how the Actuator Disc Method (ADM) can be implemented in ANSYS-CFX. Similar to the porous disc there are two methods that can be used to define the actuator disc location: either algebraically, which is described in this section or geometrically (§§2.2.1).

It is possible to define the disc location algebraically within the software code; for ANSYS-CFX this can be done using ANSYS-CFX Expression Language (CEL). The main advantage of defining the disc within the code is that the rotor parameters can be modified with ease, without the need to vary the domain or mesh. This is particularly useful when running multiple simulations of different rotor sizes and/or different yaw angles. One way to define an actuator disc using CEL is through the use of the built-in step function. The step function is defined¹ by equation (2.65). The function is defined as 0.5 at $x = 0$ to avoid a discontinuous jump at the boundary. It should be noted that

¹There is some discussion as to the function's value at x equals zero. The step function is commonly defined as a discontinuous function with a value of either 1 or 0. This definition could be problematic for CFD simulations creating a discontinuity at $x = 0$ and as such the value is defined as 0.5; as this is the value obtained by the Fourier series of the step function; and is defined as such in this thesis and within ANSYS-CFX.

the step function within ANSYS-CFX only works using dimensionless quantities.

$$H(x) = \begin{cases} 1 & \text{for } x > 0 \\ 0 & \text{for } x < 0 \\ 0.5 & \text{if } x = 0. \end{cases} \quad (2.65)$$

Using the step function it is possible to define the location of the disc using equations (2.66)-(2.69). These equations define a cylindrical volume with an internal value of one and an external value of zero (also known as a cylindrical volumetric indicator function [86]). This volume is used to define which nodes to apply the source terms to, as described in section 3.5.1.

$$\mathfrak{R} = R_R \times R_T \quad (2.66)$$

$$R_R = H(R - R_r) \quad (2.67)$$

$$R_r = \sqrt{Y_R^2 + X_R^2} \quad (2.68)$$

$$R_T = H(Z_R) \times H(d - Z_R). \quad (2.69)$$

Where \mathfrak{R} is the function defining the volume of the rotor, R_R is the function defining the rotor area, R_r is the variable rotor radius, R_T is the function defining the rotor thickness, $H(x)$ is the step function, R is the radius of the rotor, $(X, Y, Z)_R$ is the local coordinate system of the rotor and d is the depth of the rotor.

The forces can be calculated within CEL or using external software [87] and imported into ANSYS-CFX. If the forces are calculated within CEL then additional variables are required, specifically the tabulated variables C_T , C_L , C_D , c and blade twist (ϕ). It is possible to define these variables using ANSYS-CFX user functions and interpolation functionality. Forces are applied in ANSYS-CFX by adding momentum source terms. If the force is represented in cylindrical coordinates all three components are

defined as shown in equations (2.70)-(2.72):

$$S_z = D_{AD}(C_L \cos \phi + C_D \sin \phi) \mathfrak{R} \quad (2.70)$$

$$S_\theta = D_{AD}(C_L \sin \phi - C_D \cos \phi) \mathfrak{R} \quad (2.71)$$

$$S_r = 0, \quad (2.72)$$

where D_{AD} is a force as described in subsection 3.5.1, C_L is the lift coefficient, C_D is the drag coefficient, ϕ is the angle between U_{rel} and rotor plane and \mathfrak{R} is the function defining the volume of the rotor shown in equation (2.66).

Implementation in ANSYS-Fluent

Within ANSYS-Fluent the disc can be defined in a similar manner to ANSYS-CFX. The difference between the two is that ANSYS-Fluent does not use CEL to define expressions and functions. Instead ANSYS-Fluent uses its own User-Defined Functions (UDFs). UDFs are written in C programming language and compiled into ANSYS-Fluent [88]. UDFs utilize *DEFINE* macros and other predefined macros and functions supplied by ANSYS-Fluent which access ANSYS-Fluent solver data and performs other tasks [88]. It is possible to create a UDF using analogous expressions to those detailed in section 2.2.2 to implement the ADM within ANSYS-Fluent. It should be noted that to the author's knowledge, there is no inbuilt step function, so it needs to be defined as part of the UDF.

2.2.3 Actuator line method

The main problem/limitation of the actuator disc method is that it is unable to produce tip vortices due to the way the forces are evenly distributed. The Actuator Line Method (ALM) was created by Sørensen and Shen [89] to overcome this limitation.

The ALM works in the same way as the actuator disc except that instead of distributing the force over a stationary disc, it is defined as rotating lines, known as Actuator Lines (AL), using a smoothing function to avoid singularities. The ALM is described by equation (2.74) where the smoothing function is commonly defined by equation (2.75) as seen in the references [74][76][89].

$$D_{AL} = \frac{1}{2} \rho U_{rel}^2 c (C_L e_L + C_D e_D) \quad (2.73)$$

$$F_{\epsilon} = D_{AL} \otimes \eta_{\zeta} \quad (2.74)$$

$$\eta_{\zeta}(b) = \frac{1}{\zeta^3 \pi^{3/2}} \exp \left[-\frac{b}{\zeta^2} \right] \quad (2.75)$$

Where ρ is the density of air, U_{rel} is the relative velocity of the rotor, c is the chord length, C_L is the lift coefficient, C_D is the drag coefficient, e_L , e_D are unit vectors used to define the direction of lift and drag respectively, η_{ζ} is a smoothing function, ζ is a constant that serves to adjust the strength of the function and b is the distance between the grid point and the initial force point.

Implementation in ANSYS-CFX

The Actuator Line Method (ALM) works in the same way as the actuator disc except that the force is distributed over rotating lines. Similarly to the disc, the lines can be constructed either geometrically (as part of the domain) or algebraically. If the lines are constructed geometrically either the domain or mesh must move accordingly. Although a moving domain approach may be easier to implement, it is more computationally expensive and has a lower accuracy [87] compared to defining the lines algebraically, which reduces computational expense both in terms of mesh construction and solution time.

As the ALM is a transient method, the time step needs to be considered. Troldborg

[74] showed that the movement of the blade tip during one time step should not exceed one grid spacing. Therefore, the time step size is restricted by the tip speed ratio of the rotor and grid spacing used at the tip. Only the tip is considered as it is the fastest moving part of the blade.

Within ANSYS-CFX refining the disc volume into lines can be constructed using CEL in a similar way to the ADM. The lines each need to be defined in their own rotating coordinate system [87], shown in equations (2.76) and (2.77) with equations (2.78) and (2.79) used to evaluate the blade position and rotational speed respectively.

$$Y_{TransN} = y - R_r \sin(\beta_n) - \frac{c}{2} \sin(\beta_n + 90) \quad (2.76)$$

$$X_{TransN} = x - R_r \cos(\beta_n) - \frac{c}{2} \cos(\beta_n + 90) \quad (2.77)$$

$$\beta_n = \beta_i - \beta \quad (2.78)$$

$$\beta = \frac{2\pi}{60} \Omega t \quad (2.79)$$

Where $n = \{1, 2, 3\}$ represents the blade number, R_r is the variable rotor radius, c is the chord length (the offset distance from the leading edge being half this), β_i is the initial position of the blade, Ω is the rotational speed of the rotor and t is the time.

Using these coordinate systems it is possible to define the lines, shown in equation (2.80) which is combined with expression (2.66) to create the volume of the blades. This volume is used to distribute the forces over the blades in a similar way to the smoothing function previously mentioned. D_{AL} from equation (2.73), is averaged over the volume of the blades, as shown in equation (2.81), to distribute the force per length.

$$L_n = H(c(r) - \sqrt{Y_{TransN}^2 + X_{TransN}^2}) \quad (2.80)$$

$$F_{AL} = \frac{D_{AL}}{3dc(r)} \quad (2.81)$$

Where $n = \{1, 2, 3\}$ represents the blade number, $c(r)$ is the chord length, $H(x)$ is the step function and d is the rotor depth.

The force per volume is defined using a momentum source in cylindrical coordinates shown in equation (2.82)-(2.84) similar to the reference [89].

$$S_z = F_{AL}(C_L \sin \phi + C_D \cos \phi) \mathfrak{R} \times L_n \quad (2.82)$$

$$S_\theta = F_{AL}(C_L \sin \phi - C_D \cos \phi) \mathfrak{R} \times L_n \quad (2.83)$$

$$S_r = 0 \quad (2.84)$$

Where C_L is the lift coefficient, C_D is the drag coefficient and ϕ is the angle between U_{rel} and rotor plane, defined by equation (2.49) and \mathfrak{R} is the function defining the volume of the rotor shown is equation (2.66).

Implementation in ANSYS-Fluent

Within ANSYS-Fluent the lines can be defined in a similar manner to ANSYS-CFX. ANSYS-Fluent uses User-Defined Functions (UDFs) as described in subsection 2.2.2. It is possible to create a UDF using analogous expressions as detailed in subsection 2.2.3 to implement the ALM within ANSYS-Fluent.

Chapter 3

Literature review

This chapter consists of a literature review concentrating on work which considers turbine wakes and their analysis. It begins with a brief review of basic turbine theory including control volume analysis, followed by the main large scale experiments. The next sections focus on numerical analysis ranging from semi-empirical models to full CFD analysis and the rotor models used within them. For other reviews see references [22, 67, 74, 90, 91, 92].

3.1 Theory

This section describes some of the theoretical work conducted into turbines and their wakes. These theories consider idealized turbines to reduce their complexity, allowing for limits and generalizations to be considered and calculated.

3.1.1 One-dimensional momentum theory

The first wind turbine theories were adapted from work regarding propellers of ships and helicopters. The first people to look at wind turbines were Rankine [93] and Froude [94] in the late 19th century. Early approaches used control volume analysis, where

a defined volume of space (a control volume) is analysed, commonly by calculating the flow at the boundaries. This is commonly referred to as the one-dimensional (1D) momentum theory within the wind energy literature. It assumes a control volume made up of stream tubes. The flow is parallel in these tubes. The wind turbine is represented as an actuator disc, which intersects the tubes and is a discontinuous pressure/velocity step, as shown in Figure 3.1 from reference [95]. This model relies on a number of assumptions:

- Homogeneous, incompressible, steady fluid flow
- No frictional drag
- Static pressure far up and down stream is equal to the undisturbed ambient pressure
- Uniform disc and thus, a uniform thrust and infinite number of blades
- Only axial flow and thus, a non-rotational wake

Using these assumptions and the Bernolulli equation away from the disc, it is possible to calculate a number of variables including the power, power coefficient, thrust and thrust coefficient given by equations (3.1)-(3.4) respectively. Power is a measure of the energy generated by the turbine and the thrust is the axial force applied by the turbine to the flow. For more details on this method and its derivation see references [10, 11, 95].

$$P = \frac{1}{2} \rho A_r u^3 4a(1-a)^2 \quad (3.1)$$

$$C_P = \frac{Power}{\frac{1}{2} \rho A_r u^3} = 4a(1-a)^2 \quad (3.2)$$

$$T = \frac{1}{2} \rho A_r u^2 4a(1-a) \quad (3.3)$$

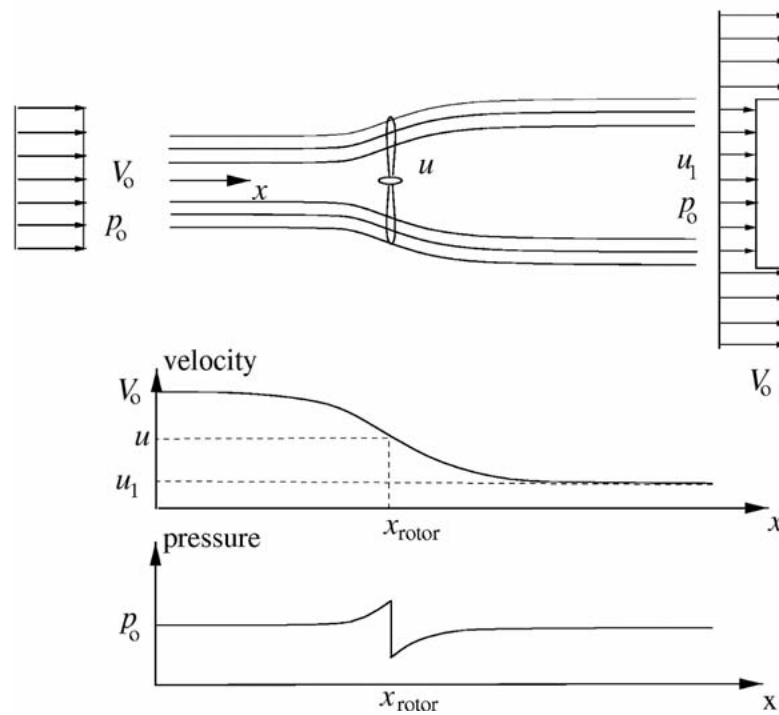


Figure 3.1: 1D momentum theory

$$C_T = 4a(1 - a) \quad (3.4)$$

$$a = 1 - \frac{u}{U_0} \quad (3.5)$$

Where P is the power, ρ is the density, A_r is the rotor sweep area, u is the axial velocity, a is the axial induction factor, C_P is the power coefficient, T is the thrust, C_T is the thrust coefficient and U_0 is the free stream velocity.

3.1.2 Betz limit

The maximum power coefficient (C_p) can be derived by taking the derivative and setting it equal to 0. Equation (3.6) shows the derivative after some algebra; giving $a = \frac{1}{3}$ and a maximum $C_p = \frac{16}{27} = 0.5925$, showing that the maximum efficiency of a wind turbine is 59.3%. C_T has a maximum of 1 when $a = 0.5$ and downstream velocity

equals zero and at maximum power $C_T = \frac{8}{9}$.

$$\frac{dC_p}{da} = 4(1-a)(1-3a) = 0 \quad (3.6)$$

This is the theoretical maximum and is commonly known as the Betz limit after the work done by Betz in 1920 [96], although it has been suggested that this is incorrect [97][98][99]. Bergey [97] suggested that it should be known as the Lanchester-Betz limit after the work done by Lanchester in 1915 [100]. Kuik [98] has further suggested that it should be referred to as the Lanchester-Betz-Joukowsky limit after the work by Joukowsky [101]. More recently it has been argued by Okulov & Kuik [99] that it should be referred to as the Betz-Joukowsky limit as Lanchester did not directly accept Froude's work [94] and defined the limit as $\frac{16}{27}Q^2$ where $1 < Q < 2$ and suggested $Q \approx 1.5$. In practice there are many factors not considered in this limit such as wake rotation, finite number of blades and aerodynamic drag.

3.1.3 Ideal Horizontal Axis Wind Turbine (HAWT)

The 1D momentum theory, described in section 3.1.1, was in one dimension and included no wake rotation. This is unrealistic as all wind turbines produce a rotational wake, which rotates in the opposite direction to the blades due to the generation of torque. The rotation of the wake causes less energy to be extracted by the turbine and hence, more kinetic energy remains in the wake. This added rotation to the wake is expressed using the angular or tangential flow induction factor, a' . The relationships between a and a' can be expressed as $a' = \frac{1-3a}{4a-1}$. Including the rotation allows the tip speeds ratio to be defined as $\lambda = \frac{\Omega R}{u}$, where Ω is the rotational speed of the blade. Actual wind turbines are not discs, but rotors made of aerofoil blades which move by generating a pressure difference on the upper and lower surfaces, creating lift. A lift force is defined as a force perpendicular to the oncoming wind as shown in Figure 3.2

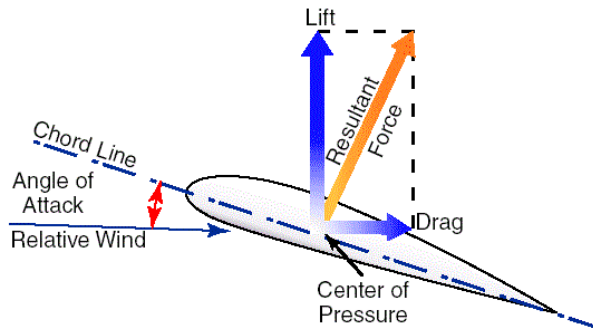


Figure 3.2: Aerofoil forces

¹ and the 2D lift coefficient is defined in equation (3.7).

$$C_l = \frac{\text{Lift force per length}}{\text{Dynamic force}} = \frac{\frac{L}{l}}{\frac{1}{2}\rho u^2 c} \quad (3.7)$$

Where ρ is the density, u is the velocity, c is the chord length, L is the lift force and l is the span.

Another important aspect of aerofoils is drag, which is defined as parallel to the direction of the wind as shown in Figure 3.2 ¹. It is caused by the viscous friction forces on the surfaces as well as the pressure around the blade. The 2D coefficient is defined by equation (3.8).

$$C_d = \frac{\text{Drag force per length}}{\text{Dynamic force}} = \frac{\frac{D}{l}}{\frac{1}{2}\rho u^2 c} \quad (3.8)$$

Where ρ is the density, u is the velocity, c is the chord length, D is the drag force and l is the span.

¹<http://www.free-online-private-pilot-ground-school.com/aerodynamics.html>

3.2 Previous experimental work

This section will outline the main physical experiments that have been undertaken. A key problem with field experiments is that it is impossible to know the entire flow field as wind is very unsteady, continually changing in direction, magnitude and turbulence intensity. The surrounding terrain also has an effect on any results. The alternative is to use wind tunnel tests where the flow conditions and terrain can be defined. However, these also experience problems, the main one being scale (as wind tunnels are far too small for a full wind turbine). The geometry is easily scalable but the flow is not, specifically the Reynolds number (discussed in section 6.3). This means most wind tunnel experiments use Reynolds numbers far lower than real world conditions.

A large number of experiments have been conducted, but they have generally been too specific in nature, concentrating on their own individual aims and objectives, taking only limited readings and results [17]. This has a limiting effect on the ability of others to make accurate comparisons. Although this thesis will not discuss in detail previous experimental work there are a number of good review articles available in the literature. The main articles are Vermeer *et al.* [17] and Crespo *et al.* [102] with a smaller section in [74]. Vermeer *et al.* [17] goes into detail about various experiments, including both near and far wake studies. Crespo *et al.* [102] focuses predominately on the far wake and covers work from 1963 until 1999. Troldborg [74] covers more recent work and concentrates on the far wake, but does have a section on the near wake as well.

There are two large scale experiments that have recently been conducted that must be noted, as follows.

3.2.1 NREL Unsteady Aerodynamics Experiment (UAE) project

The first and largest of these was the National Renewable Energy Laboratory (NREL) Unsteady Aerodynamics Experiment (UAE) project [103]. This project was made up

of a number of stages including an extensive 10-year field experiment phase [104]. One of the most important phases was phase VI, which consisted of placing the UAE 10m diameter wind turbine in the 24.4m×36.6m (80ft×120ft) NASA-Ames wind tunnel [85]. The experiment provided accurate and reliable measurements with a high spatial and temporal resolution for approximately 1700 different wind turbine conditions. This experiment was critical for a number of reasons; namely it was the first full scale wind tunnel experiment to be conducted, providing a key source due to the quantity and quality of data collected. This information has already been used in a large number of comparison studies, most notable in its own blind comparison study [105]. This comparison was used to test uncertainties in wind turbine modelling, with all participants given the same data about geometry and inflow conditions. All participants submitted their results before NREL compared and published the results. The models were divided into 4 categories: performance codes, aeroelastic codes, wake codes and CFD. This study showed a wide range of results, even for the supposedly simple situation with no yaw or stall. Yaw is the turbine's orientation where zero yaw describes a turbine perpendicular to the flow. Stalled flows feature reduced lift, caused by significant separation of the air from the blade surface. Even with no yaw or stall, the wind turbine power was predicted ranging from 25%-175% of the measured value [105]. This increased to 30%-275% in stall conditions [105]. Although there was no obvious loser in the comparison (as all models showed inconsistencies) there was one outstanding model which was a CFD model, although its application was limited to only none yaw conditions.

3.2.2 Model EXperiments In COntrolled conditions (MEXICO) project

The EU FP5 project *Model EXperiments In COntrolled conditions* commonly known as the MEXICO project [106] used a 4.5m diameter fully instrumented wind turbine which was setup in the 9.5×9.5m test section of the Large Scale Low Speed Facility (LLF) facility of the German-Dutch Wind tunnel Organization (DNW). The key thing about this experiment was the extensive flow field mapping using the stereo Particle Image Velocimetry (PIV) technique. Its aim was to create a database of measurements to validate and/or improve design and analysis models.

The data obtained in the MEXICO project has been used for different numerical studies featuring full rotor models [107][108][109][110][111], lifting line models [112][113], actuator surface models [114] and actuator line models [115][116] as well as comparative studies [117][118][119]. Carrión *et al.* [111] produced a clear table showing code, solver and geometry utilized in previous numerical studies. All full rotor CFD model simulations were conducted without inclusion of any wind tunnel geometry. Bechmann *et al.* [108] and Sørensen *et al.* [109] modelled the whole rotor and found good agreement with respect to the experimental data for axial flow. Sørensen *et al.* [109] also investigated yaw flow and found large discrepancy in the wake which was attributed to the exclusion of the nacelle and its wake in their simulations. Lutz *et al.* [110] conducted simulations of one blade as well as the whole rotor featuring the tower and nacelle, demonstrating their effect on the wake. Stoevesandt *et al.* [107] also included the nacelle although they used a shortened version in their simulations. Grasso & Garrel [112] and Micallef *et al.* [113] ran lifting line simulations on axial and yaw flow conditions, finding good agreement with the experiential data. Micallef *et al.* [113] found their method was quite sensitive to input aerofoil data and that the BEM was unsuitable for this purpose. Shen *et al.* [115][116] used the ALM

and LES to simulate the MEXICO rotor within the wind tunnel and in free air. Two sets of aerofoil data as well as different turbulence models were investigated. In general, good agreement was found although it was concluded that the original 2D aerofoil data were not suitable and that a larger thrust than the pressure measurements predicted is required. Réthoré *et al.* [120][121] compared results from actuator disc and full rotor simulations with and without the tunnel to show the significance of the wind tunnel. They found both the full rotor and actuator disc model could not match both the blade loading and velocity measurements at the same time which is in agreement with Shen *et al.* [115][116].

3.2.3 Mexnext project

These two large scale experiments produced a large quantity of data, far too great for any one organization to process. Thus the International Energy Agency (IEA) Wind Task 29 Mexnext project² was created. Its purpose was to analyse and evaluate the measurements and information from both the MEXICO and NASA-Ames projects. Mexnext (Mexnext-I) ran for 3 years from June 1 2008 until the end of 2011 [117]. It found that CFD models predicted the loads better than engineering codes, which under predicted the loads for stalled conditions [117][118][119].

3.3 Previous numerical work

This section gives an overview of numerical methods which are commonly known as Engineering methods. These methods have been developed from and rely on empirical data (for input and/or calibration) and are popular, as they do not require a lot of computational resources.

²www.mexnext.org

3.3.1 Blade models

One of the first engineering models was called the Blade Element theory or BE theory. It analysed the forces at a section of the blade as a function of its 2D geometry. This idea was later combined with 1D momentum theory into the strip theory, better known as the Blade Element Momentum (BEM) theory. It is generally attributed to Glauert in 1935 [122]. The BEM theory assumes the blade is divided into small blade elements, which are all independent of each other (no radial motion). These elements all use 2D aerodynamic aerofoil data, calculated using local flow conditions. The momentum side of the theory works by assuming that the pressure/momentum loss in the rotor plane is caused by the airflow passing through the rotor plane. This theory is used to determine the aerodynamic forces and induced velocity near the rotor in an iterative manner. It is very well known and widely used even today due to its accuracy and speed.

3.3.2 Vortex wake methods

Vortex wake models calculate the flow field as vortices and are commonly coupled with a lifting method to represent the blades. There are a number of lifting methods that have been used to model a wind turbine rotor: the lifting line, the lifting surface and the lifting panel. These methods are only briefly mentioned, for more detail see the references [17][22][91]. Each of these methods model the blade as some arrangement of distributed vortex elements. The lifting line method is the simplest model, representing the blade as bound vortex lines along which the local vortex strength is related to the local angle of attack. The lifting surface method represents the blades as a surface providing more detail. A variation on this method is the lifting panel method, which has been used extensively in the aircraft industry with only a few wind turbine applications. The 3D nature of the lifting surface and panel methods is an advantage over the line method, although this does come at a computational expense.

There are two types of vortex wake method: prescribed wake and free wake. The prescribed wake approach relies on measured or empirical input to define the initial conditions and limits. The free wake approach allows the vortex elements to convect and deform freely under the influence of the velocity field. This added freedom increases the computational expense and can lead to instability and convergence problems. The vortex wake method is good at predicting unsteady flow and yaw misalignment.

3.3.3 Wake models and computer programs

There have been a large number of wake specific models and computer programs, of which many have already been reviewed [17][22][102] and only the key ones will be noted here. Wake models focus on the far wake where the geometry and features of the rotor are only indirectly felt.

Wind-farms were first modelled using roughness elements and wake superposition techniques featuring both linear [123] and squared linear [9] superposition. These methods were very simple, using wake data from experiments and individual wake models. The first individual wake models were the kinematic models which were based on self similar velocity deficit profiles from experimental and theoretical work. From these models more specific computer programs were developed. The program EVMOD [124][125] was developed using an eddy-viscosity method, modified by an empirical-based function to account for the lack of equilibrium. Garrad Hassan later developed this method for wind-farm applications into EVFARM [126].

The computer program UPMWAKE was developed by Crespo *et al* [127][128] using a parabolic approximation. This program does not rely on the self-similarity assumption and allows the wake to be non-uniform, providing a more realistic prediction over EVMOD. An elliptical version of this program was developed by Crespo *et*

al. [129] but no fundamental difference was found. UPMWAKE has been extended to wind-farm applications in the UPMPARK program [130] and to account for the anisotropic effects of turbulence in the UPM-ANIWAKE program [131].

The problem with all engineering models is they employ a large number of assumptions and rely on empirical data for their development, calibration and input. Due to their reliance on empirical data these models are often limited by the data they have available to them. This input is also the main source of error in many calculations and situations. To reduce this error it requires using as few assumptions as possible and limiting the reliance on empirical data.

3.4 Previous computational work

The computational work detailed in this section differs from section 3.3 as it relates to Computational Fluid Dynamics (CFD). This section outlines the types of software codes currently being employed, followed by the methods used to solve the Navier-Stokes equations and some of their limitations. The section ends discussing the main methods used to model the rotor.

3.4.1 Software/codes

Due to the complex nature of the Navier-Stokes equations and the numerical methods developed to solve them, fluid flow simulations are commonly run on High Performance Computers (HPC) using specially developed CFD codes³. Some of these codes are multipurpose codes, designed to solve the Navier-Stokes equations for a wide range of problems. However, others are designed for specific applications such as FLOWer [110] and Helicopter Multi-Block (HMB) [111]; or they are developed for specific methods such as EllipSys3D which was written purely for curvilinear grids

³<http://www.cfd-online.com/Wiki/Codes>

[132]. CFD codes are very difficult to write and require verification and validation to determine their reliability and accuracy. Due to the time and effort required many are considered in-house codes and are not available on the open market such as EllipSys3D. That said, there are still many codes commercially available³ and some open source codes available such as OpenFOAM⁴. There are many advantages and disadvantages of using both in-house and commercially available codes. One main advantage of in-house codes is greater flexibility to change the source code compared to commercial codes, although this is offset by a larger number of users which can provide greater technical support.

Key codes used within the wind turbine wake sector are currently:

- EllipSys3D - an in-house code that was developed by Michelsen [133, 134] and Sørensen [135] and is a general purpose, multi block code with a finite volume discretization of the Navier-Stokes equations in general curvilinear coordinates. The variables are evaluated at the cell centers to enable computations using complex geometrical meshes. It is currently the most prominent code being used within the literature to model wind turbine wakes with multiple PhD theses relying on it [31][74][75][132][136].
- Ansys-CFX [65] - a commercially available general-purpose code which has been applied to a broad range of industries and applications. It has been used to simulate single blades [137][138] full rotors [139] and porous discs [140][141]. More recently it has been used to model wakes using actuator methods [1][2][3][87].
- Ansys-Fluent [66] - a commercially available general-purpose finite volume code used to model turbulence, heat transfer, and reactions and has several solvers and discretization types available. It has been used for several wind turbine studies

⁴<http://www.openfoam.org/>

featuring single blades [142][143][144], full rotors [145] as well as actuator discs [146][147].

- OpenFOAM - a free, open source CFD software package produced by OpenCFD Ltd. It offers users complete freedom to customize and extend its existing functionality. It has been used to simulate individual turbines such as the MEXICO rotor [107] as well as wind farms [148].

There are other codes, but these are only being used by individual researches or institutions.

3.4.2 Reynolds-Averaged Navier-Stokes

The Reynolds-Averaged Navier-Stokes (RANS) method has been the most commonly used approach for wind turbines. This is mainly due to its speed of calculations as previous mentioned (§§1.5.3 and §§2.1.1). There are different turbulence models used, although the most commonly used in the literature for turbines wakes are the 2 equation models k - ϵ , k - ω and k - ω SST. RSMs are rarely used due to their higher computational cost [91]. When people first started applying CFD to turbine problems this was the only approach available to them due to limited computer power, which today is no longer the case.

The k - ϵ model

The k - ϵ model [28][45], described in subsection 2.1.1, is one of the most popular two equation models for many CFD applications. The k - ϵ model predicts a short wake which dissipates too quickly [149], as it over predicts wake recovery [31]. To combat this problem a large number of modifications to the standard model have been developed. Réthoré [31] compared four different models, the El Kasmi-Masson model [150], the Adverse Pressure Gradient (APG) model, the realizability model and a wind

turbine canopy model. It was found that although some improvement was evident, none of them were adapted enough for wind turbine wakes [31]. Cabezón *et al* [151] compared three isotropic variations of the k - ϵ model with the anisotropic Reynolds Stress Method (RSM) (mentioned in subsections 2.1.1 and 2.1.1) as well as UPM-PARK and UPMANIWAKE described in section 3.3.3. It was found that the standard k - ϵ model under-estimates the wake deficit and although the modified models were acceptable in the far wake they needed to be tuned for different cases [151].

The k - ω model

The k - ω model, detailed in Wilcox [24] and described in section 2.1.1, is an alternative model and performs better under adverse pressure gradients and flows featuring separation. Given this the k - ω model does not outperform the k - ϵ model in any obvious way as both models under predict wake effects [152].

The k - ω SST model

The k - ω shear stress transport model normally written k - ω SST or SST k - ω model is a combination of the standard k - ω and k - ϵ models defined by Menter [29][49] and discussed in section 2.1.1. It uses the k - ω definition in the inner part of the boundary layer and gradually switches to the k - ϵ definition outside the boundary layer. This formulation is becoming the main turbulence model used today particularly for modelling turbine wakes [67].

3.4.3 Problems

The k - ω SST model also has problems with accuracy similar to the k - ω and k - ϵ models it is based on. The problem with these models is that they are based on the Boussinesq

hypothesis [30], also called the Boussinesq eddy-viscosity assumption or the Boussinesq approximation which is discussed in section 2.1.1. The Boussinesq hypothesis is considered inadequate and invalid for flows featuring sudden changes in mean strain rate, rotation and 3D effects [24] all of which feature in wind turbine wakes. Réthoré [31] makes a detailed study of the k - ϵ model describing its limitations and associated failing in wind turbine wakes and states that it is invalid for the majority of the wake region up to 10 diameters downstream. Where the Boussinesq hypothesis is invalid the turbulence models over predict the eddy-viscosity, reducing the length of the wake.

It is still possible to use RANS methods without relying on the Boussinesq Hypothesis by using the Reynolds Stress Model (RSM), discussed in section 2.1.1. RSMs model all components of the Reynolds stress tensor, making it much more resource intensive. It is able to model the anisotropic nature of the wake more accurately than the other RANS turbulence models within the wake [151]. However, RSMs rely on similar assumptions and without the eddy-viscosity term for stability it can suffer from numerical problems. Although without using the eddy viscosity RSMs are able to model anisotropic turbulence.

3.4.4 Large Eddy Simulations

The Large Eddy Simulation (LES) method (detailed in section 2.1.2) is being used more and more for wind turbine applications due to the increase in computer power and availability. LES is also able to handle unsteady anisotropic turbulent flow much better than RANS, but this does come with a higher computational expense. As previous discussed, eddy-viscosity turbulence models are used as part of LES method, which means that the problems of the Boussinesq hypothesis are still encountered. Réthoré [31] showed that if cell size is taken small enough then the error made by the eddy-viscosity concept is negligible for wind turbine wakes.

As LES is computationally expensive near solid boundaries, DES of wind turbines is promising. Johansen *et al.* [153] performed a DES of a single NREL phase VI blade showing good agreement with experimental data.

3.4.5 Boundary conditions

A problem with all computational simulations is the inflow parameters. Wind turbines experience turbulent shear inflow which varies significantly with time. Early simulations used uniform, laminar inflows to reduce computational cost. More recently it has been shown how turbulence inflow [154] and shear inflow (atmospheric boundary layer) [155][156] affect flow behind the wind turbine.

For LES there are two ways of creating a turbulent inflow: using a synthesized inlet and using the precursor simulations method. The synthesized inlet as detailed in Mann [157][158] is based on creating a turbulent field by influencing the current flow. The advantage of this is that parameters such as turbulence length scale can be directly specified. This method was used by Troldborg [74][154] to create a turbulent inlet. It was inserted in one rotor diameter before the rotor to prevent decay. The flow was influenced using body forces in the momentum equation following the work by Mikkelsen *et al.* [159].

The Precursor simulation method is achieved by defining a separate simulation, which is then used as the inflow for the next simulation. The advantage of this method is that the ground effect is taken into account. However, it cannot be easily changed and adapted once created and it is computationally very expensive. This method has been used in a number of papers including references [23][148][160].

When solid boundaries are not included in the simulation directly, which is normally done through an actuator method, it has been shown that the solution does not change much when the Reynolds number is higher than 1000 [22][89][161][162]. It

was also observed that the behaviour of the wake maybe insensitive to the blades' Reynolds number [163], which is important for many rotor models that do not consider the blade geometry.

3.5 Rotor modelling

There are many ways to represent the rotor of a turbine. These range in complexity and detail starting by representing the rotor as a simple constant momentum sink, to the full rotor geometry including the tower and nacelle. The most obvious way to simulate a wind turbine is to construct a model as close to real life as possible by using the full geometry of the blade. These models are known as full rotor or direct rotor models. The main disadvantage of this method is that it needs to resolve the blade boundary layer which requires a fine mesh and large amount of computational power. Due to the computational cost it is common to represent the rotor instead of simulating it directly.

The simplest approach to rotor modelling is representing the wind turbine as a momentum sink which was the approach used in early numerical work as mentioned in section 3.3.3. This is generally done for far wake studies where the rotor geometry is less important, such as modelling wind-farms and other large features. Calaf *et al.* [70] represented wind turbines as drag discs and used LES to study the wind turbine array boundary layer. Prospathopoulos *et al.* [164] represented rotors as porous discs on the top of two different Gaussian hills and showed how the terrain affects the wakes and velocity recovery. They found that on a Quasi-3D hill the wake was still significant up to 40 diameters downwind of the turbine, which is much longer than for flat terrain. Rados *et al.* [152] represented wind turbines as momentum sinks when comparing two codes using k - ϵ and k - ω turbulent models and found no significant difference between the codes.

The most common way to represent the rotor is by using actuator methods, where

the blades are represented by body forces in the shape of either a disc, line or surface. Actuator methods have been used for many years in modelling different rotors such as helicopter rotors [165], propellers [166] and turbines [67]. This approach reduces computational expense and mesh requirements as the blades are not represented by solid bodies. Actuator methods take hours to complete compared to days or weeks for full rotor simulations [167]. However, the influence of the 3D geometry of the blade is not accounted for. There are two main types used: the actuator disc (AD) and actuator line (AL). There is also an actuator surface (AS) method, but this is a newer method and has not been developed as much.

3.5.1 Actuator disc method

The Actuator Disc Method (ADM) represents a time averaged rotor using forces distributed over a disc with the same dimensions and volume as the swept volume of the rotor. There are a number of variations of the ADM within the literature including constantly and variably loaded discs, as well as variations with and without rotation [67][68][69].

Réthoré *et al.* [168] compared the AD to Conway's analytical solution [169] and found good agreement. Réthoré & Sørensen [170] further compared it to three more analytical solutions showing good agreement and suggesting a method to reduce computational costs. The actuator disc method has been used to model stand alone wind turbines [75][136][161] and multiple wind turbines [136][171][172]. It has also been used to model terrain effects, Makridis & Chick studied two wakes over a Gaussian hill [146] as well as flow over complex terrain in a coastal region [147]. Both studies were conducted using ANSYS-Fluent and were compared with experimental data and WAsP. They found CFD predictions were within 5% of the measurements while WAsP was as much as 15% out. Alinot & Masson [173] used the AD to show the wake

structure in the atmospheric boundary layer using a modified k - ϵ turbulence model to simulate the wind turbine operating in different types of stratification. They found that a stable atmosphere produced the lowest power output and the unsteady atmosphere condition produced the highest power output. Ivanell [136] used 2D AD combined with periodic boundary conditions to simulate the Horns Revs wind-farm, showing good agreement with measurements but the power production was found to depend on the turbulence levels and the inflow angle [136][172].

3.5.2 Actuator line method

The main problem/limitation of the actuator disc method is that it is unable to produce tip vortices due to the way the forces are evenly distributed. The Actuator Line Method (ALM) was created by Sørensen & Shen [89] to overcome this limitation. The ALM works in the same way as the actuator disc except that instead of distributing the force over a stationary disc, it is defined as rotating lines, known as Actuator Lines (AL), using a smoothing function to avoid singularities.

The ALM has been used for a number of studies including detailed studies by Troldborg [74] and Mikkelsen [75]. Troldborg [74][154] used the AL combined with LES to study how different inflow conditions affect the wake of a single wind turbine. Troldborg [74] found that shear and ground presence affects the axisymmetric structure of the wake development and observed minimal wake expansion vertically down. It was also observed that with a uniform laminar inflow, the wake still becomes turbulent especially at low velocities. Ivanell [136] used the AL method to do a stability study on the wake structure.

The AL model has been useful in modelling turbine interactions, specifically interactions of a row of three wind turbines [74][174]. Troldborg [74] showed how laminar

and turbulent inflow cases were very different. In the turbulent case the wake was unstable and broke up before the second turbine. However, in the laminar case this does not happen, resulting in higher velocities at the second turbine and creating higher yaw loads for the third turbine. Due to the transient nature of the ALM it is commonly used with LES [74][77][154], although it has also been used with DNS [162]. Ivanell *et al.* [162] used DNS on a third of the wake to provide detailed information on the wake structure without ambient turbulence.

The ALM has been used in a number of comparison based papers to evaluate the ADM [75][77][175]. Mikkelsen [75] compared the AD, AL and BEM methods at simulating flow through coned rotors and yaw flow. It was found that the AD and AL were able to model the coned and yawed rotor although the AD was found to be poor at high yaw, with the BEM method being poor at both.

3.5.3 Actuator surface

The actuator line method was further extended into the actuator surface method by Shen *et al.* [176][177]. The surface method represents a blade as a plate surface, instead of a single line over which the forces are distributed. This requires more information. Instead of the sectional lift and drag coefficients c_l and c_d used by the AD and AL, the surface method requires knowledge of pressure and skin friction. An Actuator surface hybrid model has been developed which replaces the blades with their mean surfaces and a pressure jump [176][177][178]. The actuator surface model has been used to model the NREL rotor [179][180] and MEXICO rotor [114].

3.5.4 Full Rotor

The full rotor or direct rotor method, directly models the rotor and the blades exactly. The inclusion of the blade geometry means that compressible effects may be important

at the blades tips which could require that the compressible Navier-Stokes equations be solved. They are very accurate, but extremely computationally expensive as the inclusion of the blade geometry requires a fine moving/sliding [145] or overset mesh [132][155] to capture the blade boundary layer.

There have been a number of studies using this technique. The first was done by Sørensen & Hansen [181] and used the k - ω SST model. To reduce the computational expense of this method some studies only simulate one blade [137][138][142][143][144][153]. One advantage of full rotor studies is they allow for the inclusion and investigation of features such as the tower and nacelle, as well as any interactions between them and the rotor. A number of studies have made use of this to investigate the interactions between the rotor and the tower [132][182] and nacelle [145]. Zahle [132][182] conducted a study of the NREL phase VI rotor both with and without the tower, and found good agreement with the experimental data. He was able to show the affect of the rotor on the tower's shedding frequency. Zahle & Sørensen [156] have used the full rotor and an overset grid method to investigate the effect of including ground effects and shear inflow on a wind turbine. It was shown that including the ground effects without a shear inflow increased the power prediction by 0.4%; adding a shear inflow increased this further to 5.5% [156].

The main purpose of the full rotor model studies are generally towards comparison and evaluation of simpler models. Réthoré *et al.* [167] compared the actuator disc and full rotor models with the k - ω SST model in uniform and shear inflows. The study showed the computational expense of using the different techniques, with the actuator disc taking hours to converge whereas the full rotor model took months to converge. It also showed that (at least for uniform inflow conditions) the difference between the models is relatively small and does not justify the extra computational expense. Réthoré *et al.* [175] went one step further and compared the AD and AL with a full rotor simulation in the near wake region. It was found that there were small structures

created in the full rotor simulation that have a significant impact on the generation of turbulence, which the AD and AL are unable to predict. However, this study did not use a turbulent inflow which may have affected the overall impact.

Due to the large computational cost associated with the full rotor model, simulations using this approach are commonly restricted to only one blade or at most, a single rotor. However, there is a project to conduct a full wind farm simulated using the full rotor model [183] although to simulate 48 turbines requires a 3840 core supercomputer and approximately 300 million cells.

Chapter 4

Methods

This chapter details the five CFD studies carried out in this thesis to achieve the objectives set out in section 1.2. The studies increase in complexity and novelty. The first four studies in sections 4.1–4.4 were conducted to verify (benchmark) and develop the modelling methods described in section 2.2. They feature comparisons with previous work including experimental and numerical data. Finally, section 4.5 details novel work investigating the effect rotor diameter has on wind turbine interactions and power generation.

4.1 One-dimensional momentum theory study

The first study featured comparison with the best known theoretical model of flow about a turbine, namely the 1D momentum theory as discussed in section 3.1.1 and illustrated in Figure 4.1. The theory and hence this study featured a uniform disc without rotational effects. Only the porous disc and uniform actuator disc model, defined with the thrust coefficient (C_T), were used detailed in subsection 4.2.3.

As comparison does not require any form of special domain or mesh construction, the domain configuration defined in section 4.2 was used. The CFD simulations were

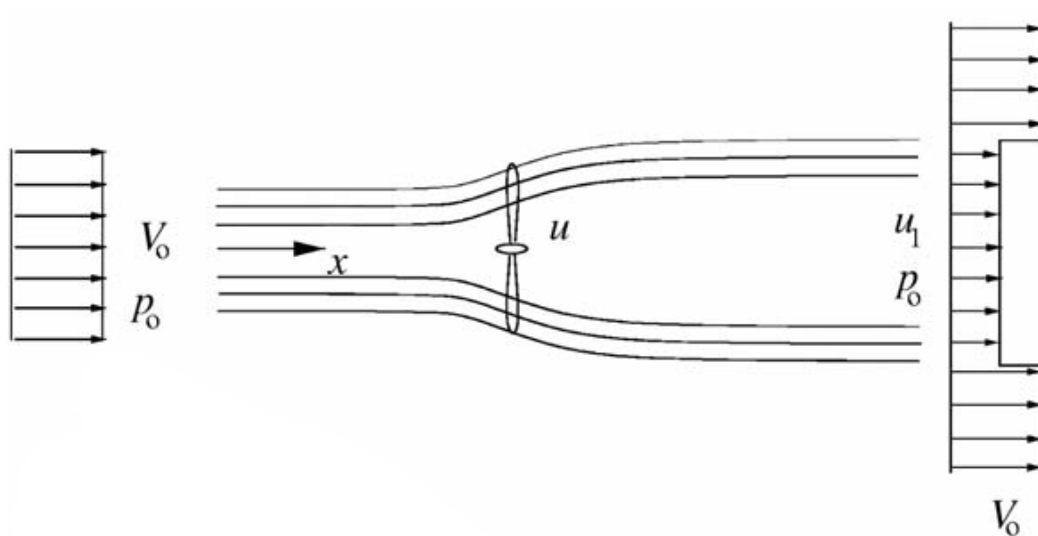


Figure 4.1: 1D momentum theory

conducted using the steady-state Reynolds-Averaged Navier-Stokes (RANS) equations together with the k - ω SST turbulence model [29]. ANSYS-CFX was used to calculate the solution using a mixed hybrid mesh, constructed with 6.2 million cells. Such a high mesh density was used for this study as the simulation was conducted as part of the porous disc study, described in Section 4.2.

4.2 Porous disc study

This study was a comparison with previous numerical [140][141] and experimental [184][185] studies. The previous experiments [184][185] were conducted in a water channel measuring $21\text{m} \times 1.37\text{m}$ with a depth of 0.3m . Three 0.1m diameter discs of various porosities were placed into the channel. The different porosities were used to represent turbines with different thrust coefficients (C_T), which were measured using a pivot arm mounted onto a load cell. The water velocities were measured at various locations using an Acoustic Doppler Velocimeter (ADV) at a sample rate of 50Hz and the data was averaged over 3 minutes. The previous numerical studies chosen

for comparison, are described in references [140][141]. These used ANSYS-CFX to reproduce analogous experimental data [185]. These studies were chosen because they were conducted using the same software as in the work presented in this thesis, hence providing a benchmark with which to verify current modelling methods.

The numerical simulations in this study were calculated using ANSYS-Workbench, specifically ANSYS-CFX using the steady-state solution of the Reynolds-Averaged Navier-Stokes (RANS) equations [18], together with the $k-\omega$ SST turbulence model [29]. This model was chosen over the $k-\epsilon$ model based on the literature and some preliminary simulations which showed that the $k-\omega$ SST model performs better in flows featuring adverse pressure gradients [24] in terms of the accuracy to predict the flow properties. The $k-\omega$ SST model was also used in the benchmark studies [140][141].

The model domain was defined using the dimensions of the experimental channel set-up [185]. It featured a 2m long inlet, a 3m outlet and a 0.3m deep-water column along with a 0.1m diameter disc with a thickness of 0.001m at the centre. The flow was assumed to be symmetrical. Allowing a symmetry plane to be created through the centre of the disc, dividing the domain in half to create a width of just 0.685m as opposed to the 1.37m width of the experimental channel; therefore reducing the computational expense. As part of this study, three discs were simulated with two different sets of boundary conditions to represent a channel and a duct. The disc was defined with a diameter of 0.1m, a thickness of 0.001m and a uniform momentum loss across the disc in the longitudinal (z -)direction. As part of this study three discs were simulated with two different sets of boundary conditions to represent a channel and a duct, each with two different inlets totaling 12 simulations.

4.2.1 Mesh

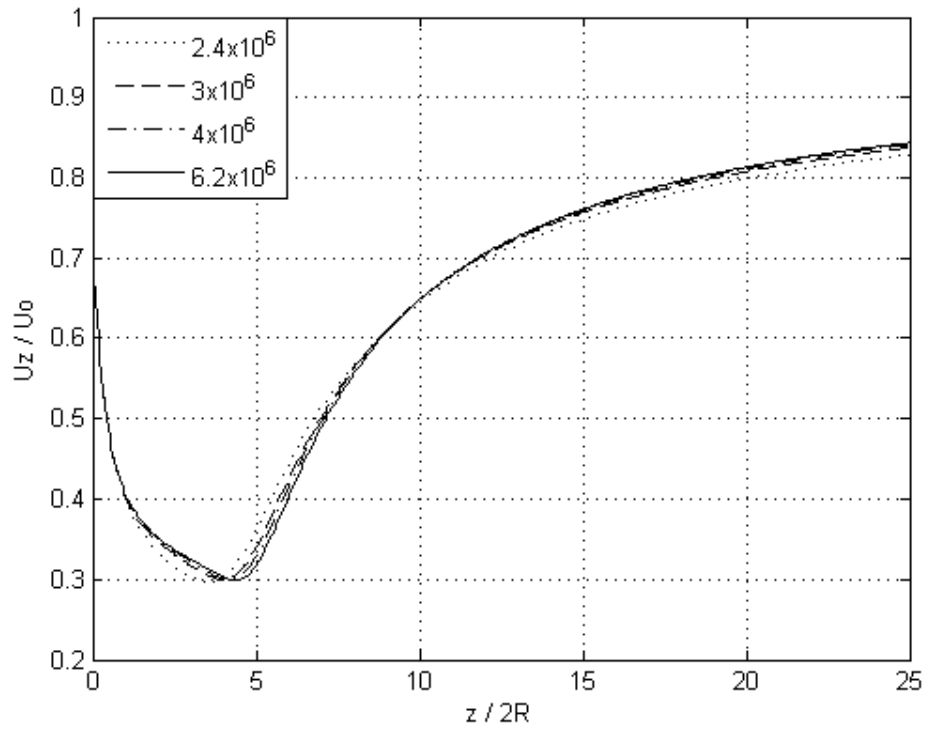
In this study a mixed hybrid mesh was constructed consisting of various mesh densities ranging from 2.4 to 6.2 million cells. The majority of the domain was constructed out of tetrahedral cells with a structured inflation zone of wedge cells at the boundary of the floor and symmetry plane. The data presented corresponds to a mesh density of approximately 6.2 million cells and 2 million nodes unless otherwise stated. Figure 4.2 shows the velocity profiles of various mesh densities along the centre line behind the disc and at 7 diameters (7D) downstream of the disc. There was very little difference between the predictions of the four different mesh densities showing little advantage in refining the mesh. Figure 4.2a demonstrates a realistic velocity recovery beyond the peak velocity drop just before $z/2R = 5$. Figure 4.2b shows that the main differences between the different mesh densities are within the floor boundary layer and at the peak velocity deficit.

4.2.2 Boundary conditions

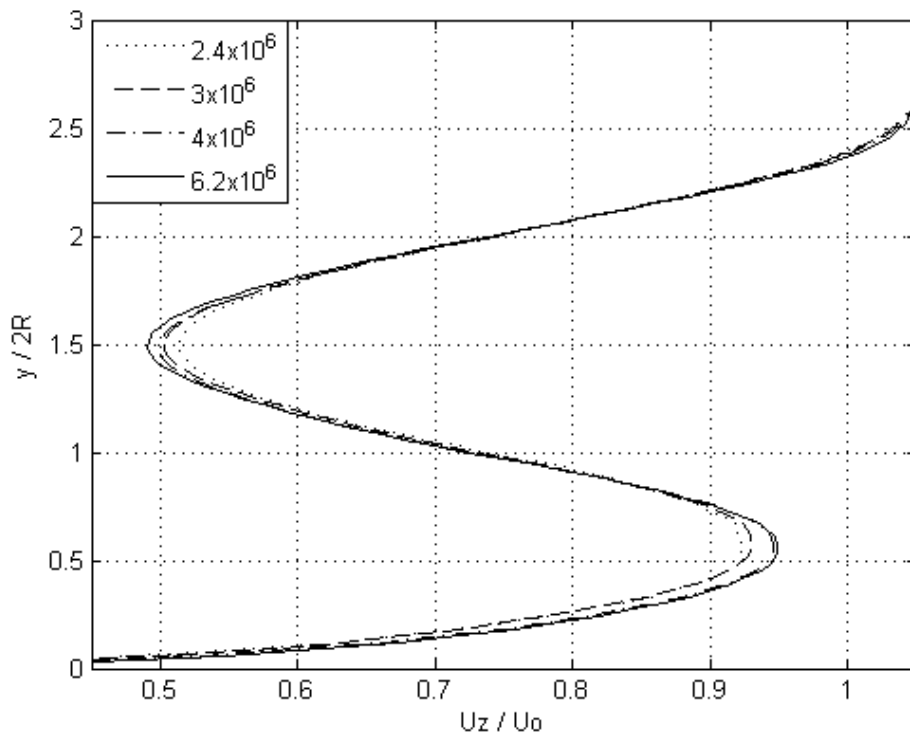
The inlet velocity was defined by equation (4.1) in the same manner as the numerical study [141] and based on the empirical data [185]:

$$U_{inlet} = 2.5U^* \ln\left(\frac{y_w U^*}{\nu}\right) + A \quad (4.1)$$

where U_{inlet} is the inlet velocity across the width of the domain, U^* is the friction velocity, y_w is the depth of the water, ν is the kinematic viscosity and A is a boundary layer model constant. Curve fitting methods were used to define U^* and A . The numerical paper [141] used values of $U^* = 0.00787\text{m/s}$ and $A = 0.197\text{m/s}$ which were also used in this study. Figure 4.3 shows the inlet velocity used in this work and the experimental study [185], normalized with a free stream velocity (U_0) of 0.331m/s for



(a)



(b)

Figure 4.2: Normalized velocity profiles showing different mesh densities (a) along the centre line and (b) 7 diameters downstream of the disc

the experimental study [185] and $U_0 = 0.33\text{m/s}$ in this work. The vertical height was also normalized with the diameter of the disc ($2R$).

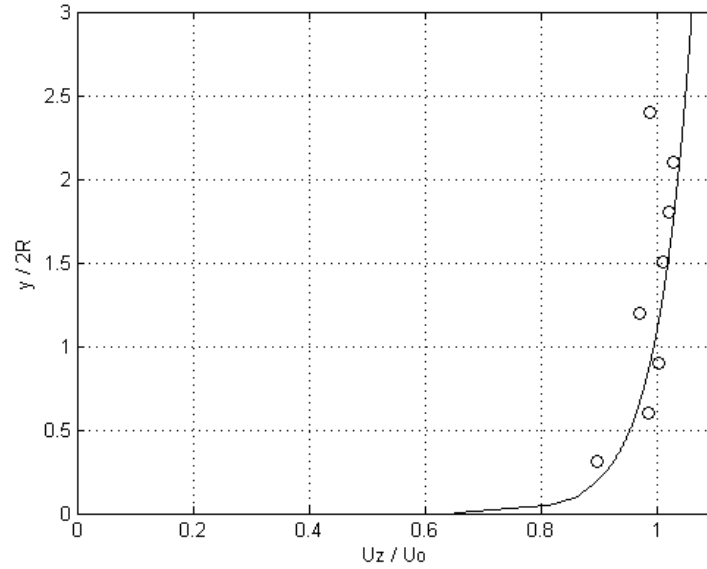


Figure 4.3: Normalized velocity at the inlet of this study (solid line) and experimental data (o) [184]

The turbulence intensity, which is defined by equation (4.2), was described in two different ways to define two simulations referred to in this study as inlet 1 and inlet 2. Both inlets were set with a turbulence intensity of 5% at the inlet to produce agreement with the experimental data [185] for $y/2R > 0.5$. The difference between the inlets is that inlet 2 was also defined with a length scale of 0.3 (height of the domain). Both these approaches are different to the reference [141] which defined the turbulent kinetic energy and eddy dissipation.

$$I \equiv \frac{u'}{\bar{U}} \quad (4.2)$$

$$u' \equiv \sqrt{\frac{2}{3}k} \quad (4.3)$$

$$\bar{U} \equiv \sqrt{U_x^2 + U_y^2 + U_z^2} \quad (4.4)$$

In equations (4.2)-(4.4) I is the turbulence intensity, u' is the root-mean-square of the turbulent velocity fluctuations, \bar{U} is the mean velocity and k is the turbulent kinetic energy and $U_i = [x, y, z]$ is the velocity in the x, y, z directions.

The outlet was defined as a static pressure outlet with a relative pressure of 0 Pa. The floor and far side of the domain was defined as a non-slip wall. In this study two separate benchmark models were produced featuring different boundary conditions at the top or roof of the domain; the first featuring an opening creating a channel and the second featuring a non-slip wall creating a duct. These boundary condition sets were analogues of those in the references [140][141]. Although a free-surface approach could be considered more suitable, as the experiment was carried out in a channel featuring water and air interactions, it was shown to only produce a 0.2% depth change at the disc [141].

4.2.3 Resistance

The resistance was defined in the simulations using the resistance loss coefficient in ANSYS-CFX. The work described in this study and previous numerical studies [140][141] used identical coefficients of 1, 2 and 2.5 in separate simulations to represent the three different porous discs used in the experimental study [185]. The coefficients were derived based on the thrust coefficient measured in the experimental data and were estimated using equation (4.5) which is a theoretical relationship between C_T and K [141].

$$C_T = \frac{K}{(1 + 0.25K)^2} \quad (4.5)$$

4.2.4 Code comparison

This section details a code comparison study between ANSYS-CFX and ANSYS-Fluent. Although both codes are owned by the same parent company ANSYS they were developed separately, and calculate the Navier-Stokes equations differently. On first appearances the two codes differ in their implementation, with ANSYS-CFX using ANSYS-CFX Expression Language (CEL) and ANSYS-Fluent using its own User-Defined Functions (UDFs) to customize simulations. The main difference between the two codes is actually their method of discretization of the Navier-Stokes equations as ANSYS-CFX uses vertex-centered scheme and ANSYS-Fluent uses a cell-centered scheme. The difference between the two schemes is how and where the flow variables are calculated and stored as discussed in subsection 2.1.5.

Both codes were used to simulate analogous models of a porous disc within a water channel, specifically the disc had a resistance loss coefficient of 2 which is called the inertial loss coefficient within ANSYS-Fluent. The predictions of both codes converged to a root-mean-square residual of 1×10^{-5} and have been compared to the experimental data [185].

4.2.5 Cell type study

This section describes a comparative study which investigated the differences between linear and quadratic mesh cells (i.e. without and with mid-side nodes shown in Figure 4.4) [35][186]. The study was conducted using the domain and set-up described in section 4.2 using inlet 1. The difference between linear and quadratic cells is the number of nodes on each cell, specifically quadratic cells feature mid-side nodes as shown in Figure 4.4. As part of the study ten different meshes were created, five with linear cells and five with quadratic cells as shown in Table 4.1. Table 4.1 shows the large difference in the number of nodes between the difference cell densities.

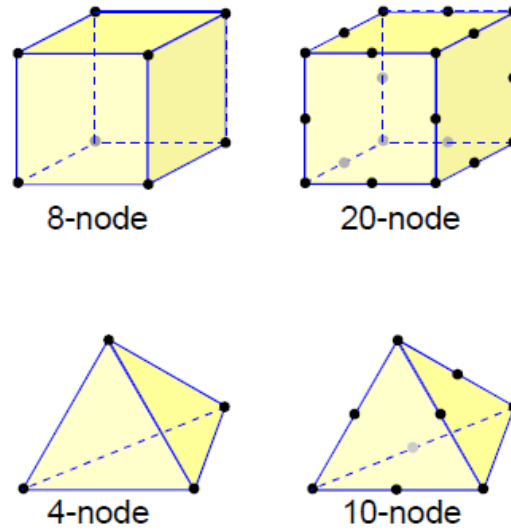


Figure 4.4: Difference in cell type

Cells (million)	Nodes linear (million)	Nodes quadratic (million)
1.36	0.466	2.64
1.57	0.513	2.96
2.42	0.694	4.22
3.44	0.959	6.08
4.38	1.38	7.81

Table 4.1: Mesh densities using linear and quadratic cells



Figure 4.5: Representation of the blade used in the MEXICO project where the red zones represent the transition zones between aerofoils

4.3 Actuator disc study

This study reproduces the EU FP5 project ‘Model EXperiments In Controlled COnditions’ or ‘MEXICO’ project as discussed in subsection 3.2.2 and detailed in the reference [106]. The experiment was conducted using a three bladed 4.5m diameter wind turbine set up in the $9.5 \times 9.5\text{m}^2$ open test section of the Large Scale Low Speed Facility (LLF) wind tunnel of the German Dutch Wind tunnel Organization (DNW). Data were collected over five sections of the blades, providing loads and pressure measurements with the flow field determined using Particle Image Velocimetry (PIV) measurements. The blades were constructed out of three different aerofoils: DU 91-W2-250 at the root of the blade; RISØ A1-21 at mid span; NACA 64-418 at the outer part of the blade; as shown in Figure 4.5. For more details on the geometry see reference [106].

In this study, simulations were conducted using the actuator disc (AD) model and results were compared to the experimental data, as well as previous numerical studies [120][121]. The numerical simulations were calculated using ANSYS-CFX to obtain a solution of the Reynolds-Averaged Navier-Stokes (RANS) equations [18] together with the $k-\omega$ SST turbulence model [29].

The geometry of both the wind turbine and wind tunnel requires Non Disclosure Agreements (NDA) and as such any figure within this document showing them has been slightly altered and should not be considered accurate. A representation of the wind tunnel is shown in Figure 4.6. It should be mentioned that a separate NDA is needed for the exact geometry of the collector and nozzle, which was not obtained

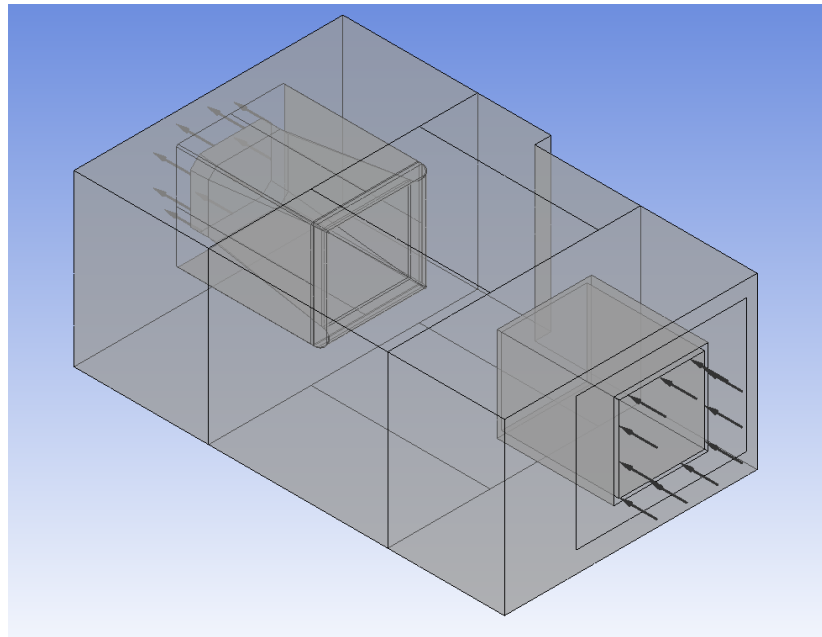


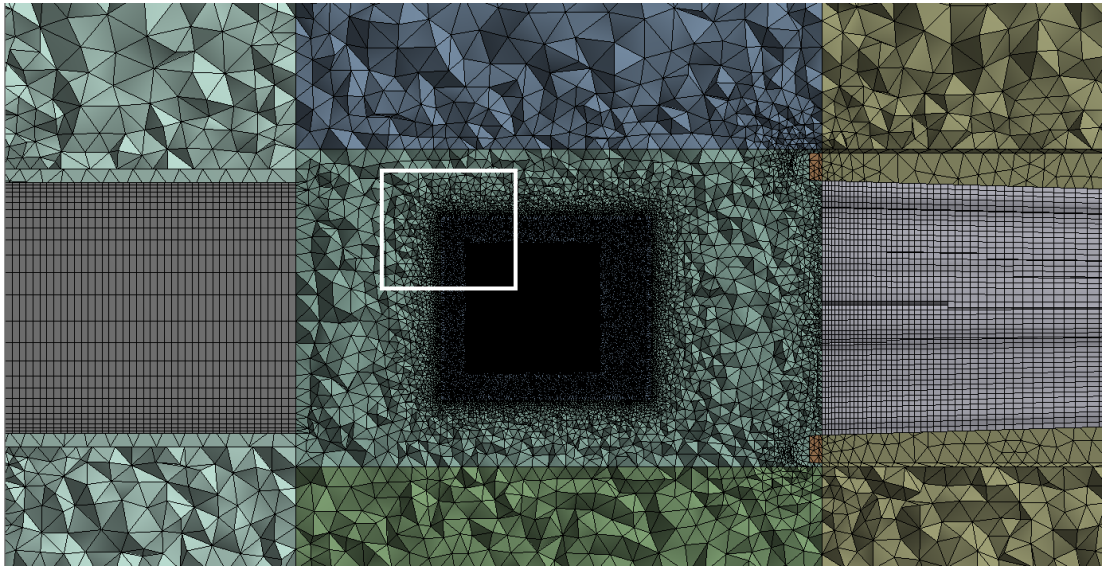
Figure 4.6: Mexico study wind tunnel

for this study. Instead a representation was created using a straight square nozzle and collector (Figure 4.6).

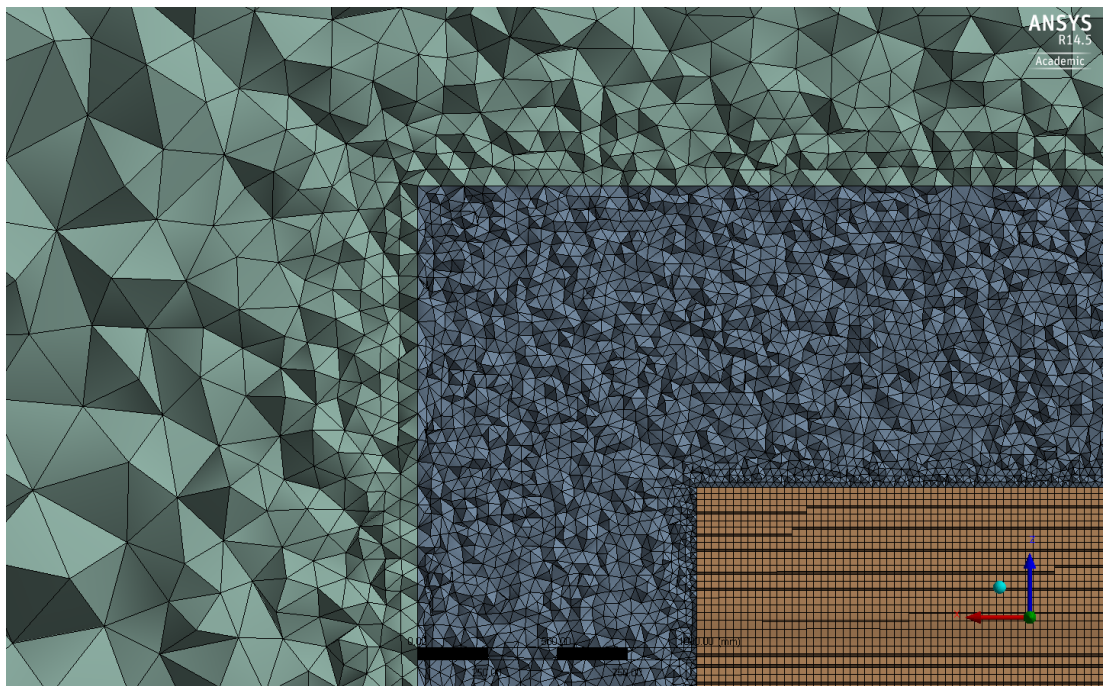
4.3.1 Mesh

As part of this study two mixed hybrid meshes of 15 million cells (8.8 million nodes) and 32 million cells (11.5 million nodes) were created with tetrahedral and hexahedral cells. The meshes consisted of a fine hexahedral refinement zone centered about the turbine hub, with a cell size of approximately 25mm. This zone was surrounded by a fine tetrahedral transition region containing cells of approximately 75mm and 50mm for the coarse and fine mesh respectively, before coarser outer regions as shown in Figure 4.7. The collector and nozzle regions were meshed using a swept hexahedral mesh, each with 50 divisions with a bias towards the walls.

Figure 4.8 shows the velocity through the centre of the domain with the 15 million cell mesh (dashed line), 30 million cell mesh (solid line), numerical study (o) [120]



(a)



(b)

Figure 4.7: Mesh used in the actuator disc study (a) cross-section through the domain and (b) detailed view

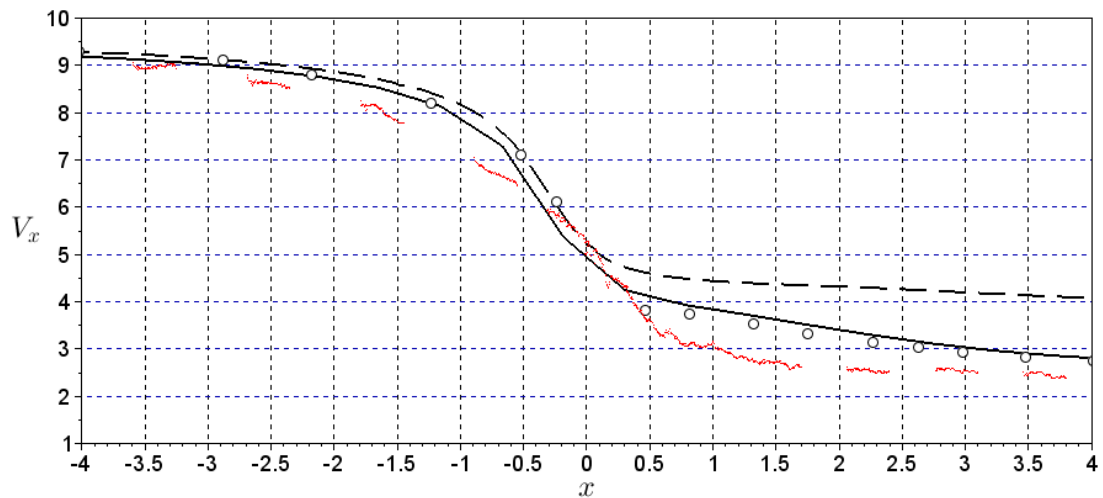


Figure 4.8: Centre line velocity for the 10m/s inlet with the 15 million cell mesh (dashed line), 30 million cell mesh (solid line), numerical study (o) [120] and experimental data (.) [106]

and experimental data (.) [106]. It shows that the 15 million cell mesh under-predicts the velocity drop at the rotor and that the 30 million cell mesh is closer to the other data and will be used for the rest of this study.

4.3.2 Boundary conditions

Three inlet velocities of 10m/s, 15m/s and 24m/s were used as part of the experiment [106]. Preliminary simulations showed that these inlet velocities produced a higher velocity profile than was reported in the experiment. Due to this, slightly modified inlet velocities were used in this study, which were taken from the experimental data. Velocities of 9.3m/s, 14.44m/s and 23.77m/s were used, as these were the average of the first velocities given in the experimental data just after the inlet and far upstream from the turbine. The density of the air was also defined based on the average reading taken during the experiment, of 1.24kg/m^3 .

The walls of the wind tunnel, including the nozzle and collector, were defined as free slip walls to reduce computational expense. Preliminary simulations showed that

the different walls had little effect on the results as the wall boundary layer did not develop significantly in the inlet.

In this study the AD method was used as described in subsection 2.2.2. The aerodynamic coefficients were supplied for each aerofoil profile and a smoothing expression was created in CEL to transition between the coefficients based on the radial position along the blades. The data was obtained through a NDA and so not detailed here, see reference [106] for more information.

4.4 Two turbine study

This study investigated the interactions between two wind turbines. The interactions between the first two turbines are the most important as the second turbine experiences the highest power loss [13][187][188].

There have been a number of wake interaction studies, both experimental and numerical, ranging from two turbines to full wind farms including 30 turbines [189][190][191] and 48 turbines [192] as well as infinite farms [136]. There have also been a number of comparative studies [14][15][193]. The majority of the numerical interaction studies use actuator methods such as the AD [160][189][194] or AL [174][195], although full rotor models have recently been conducted [139].

The majority of studies focus on axially aligned turbines and many studies have investigated the effect of axial or streamwise spacing on wake interactions. Choi *et al.* [139] used ANSYS-CFX with the full rotor model, including nacelle and tower, to investigate the effect of spacings ranging from 3 – 7 rotor diameters. They [139] found that the second turbine experiences a power loss of 35-65% the power of the first turbine for the given spacings. They suggested a five diameter spacing as a design criteria. Yang *et al.* [194] and Meyer & Meneveau [160] investigated infinite aligned

wind-farm configurations using the ADM and LES. Meyer & Meneveau [160] investigated the optimum spacing and included turbine cost and land cost in their calculations and determined an approximate optimum spacing of 15 diameters.

Adaramola & Krogstad [196] and Bartl *et al.* [197] both conducted experimental studies using two axially aligned 0.9m diameter turbine models at different distances. Bartl *et al.* [197] used spacings of 3 and 5 diameters while Adaramola & Krogstad [196] used 3, 6 and 9 diameters. Adaramola & Krogstad [196] found a power loss of 29-45% depending on the spacing, and that by operating the first turbine outside optimum tip speed ratio can significantly improve the second turbines performance.

Mikkelsen *et al.* [174], Troldborg *et al.* [195] and Flecher & Brown [198] investigated the effect of streamwise (axial) and crosswind (lateral) displacement on wake interactions, simulating full and half wake interactions. Mikkelsen *et al.* [174] and Troldborg *et al.* [195] used the ALM in their studies. Troldborg *et al.* [195] investigated the influence of turbulence intensity on wake structure of full and partial wake interactions. Mikkelsen *et al.* [174] investigated the optimal pitch settings of the turbine experiencing wind shear. Flecher & Brown [198] used the Vorticity Transport Model (VTM) to investigate the wake structure. They found a turbine 6 diameters apart may experience a power loss of 40-50% and that partial wake interactions cause significant unsteadiness in the wake and fatigue reducing the life of the blades.

Multiple studies have investigated the difference between aligned and staggered turbine layouts [189][190][199]. Wu & Porté-Agel [189] used the ADM with and without rotation and found that a staggered layout has more homogeneous velocity profile as well has higher velocity and lower turbulent intensity thus greater efficiency than an aligned layout. Chamorro *et al.* [190] conducted an experimental study in a wind tunnel using model turbines with a rotor diameter of 0.15m in a staggered layout. Their analysis showed that a staggered layout has a 10% increase in power output.

Terrain effects on wake interactions have been investigated. Makridis & Chick

[146] used ANSYS-Fluent to investigate the effects of positioning two wind turbines on top of different hills. Ozbay [199] investigated the effect hills have on wake interactions using a wind tunnel and roughness elements (spires) and found that wake effects were reduced if the turbine was placed on top of a hill with a moderate slope (12°).

Tidal turbine interactions have also been investigated. Turnock *et al.* [200] used ANSYS-CFX and the ADM to investigate the effect of lateral spacings using 2, 4 and 6 diameters and added a turbulence source term. They agreed with wind turbine studies that a staggered layout configuration is beneficial. O'Doherty *et al.* [201] used ANSYS-Fluent to investigate tidal contra-rotating turbine rotors spaced 1, 2 and 3 diameters apart and found the initial wake recovery is predicted to be faster than a single turbine, although full recovery is the same.

4.4.1 Current work

Every wind-farm is individual, with different turbine size and layout as well as velocity profiles, not to mention the terrain. The literature shows that the worst case scenario is an axially aligned full wake interaction, and that the highest velocity deficit and power loss is experienced by the second turbine [13][187][188]; and so that is the configuration chosen in this thesis.

This study features two 10m NREL phase VI turbines [85] but with three blades, axially aligned at three and six diameters apart, as they seemed to be the most widely used spacing within the literature. Two previous studies, an experimental [197] and a numerical [195] study, were chosen for comparison as they feature turbines spaced three and six diameters apart. As each study uses different turbines and velocities, this study will compare the results using normalized data in terms of free stream velocity and turbine size. The numerical simulations were calculated using ANSYS-CFX to

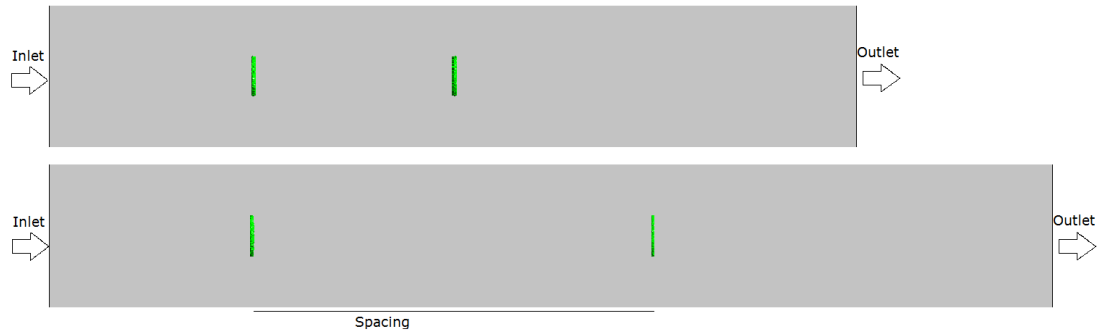
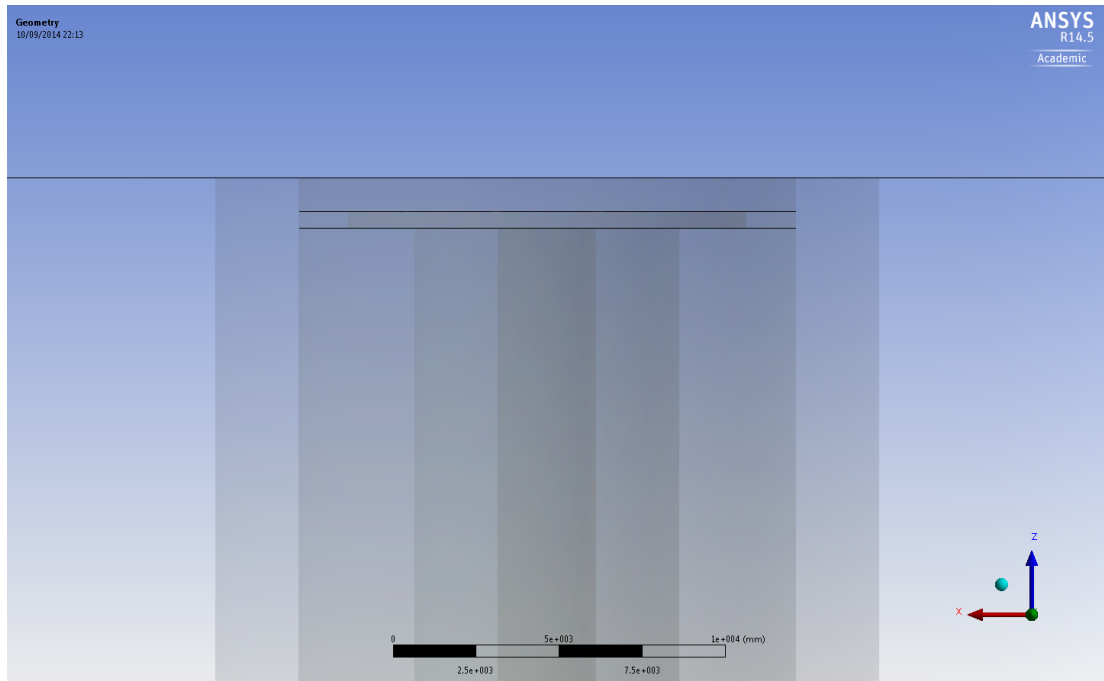


Figure 4.9: Two turbine domain with 3 diameter spacing on top and 6 diameter spacing on the bottom

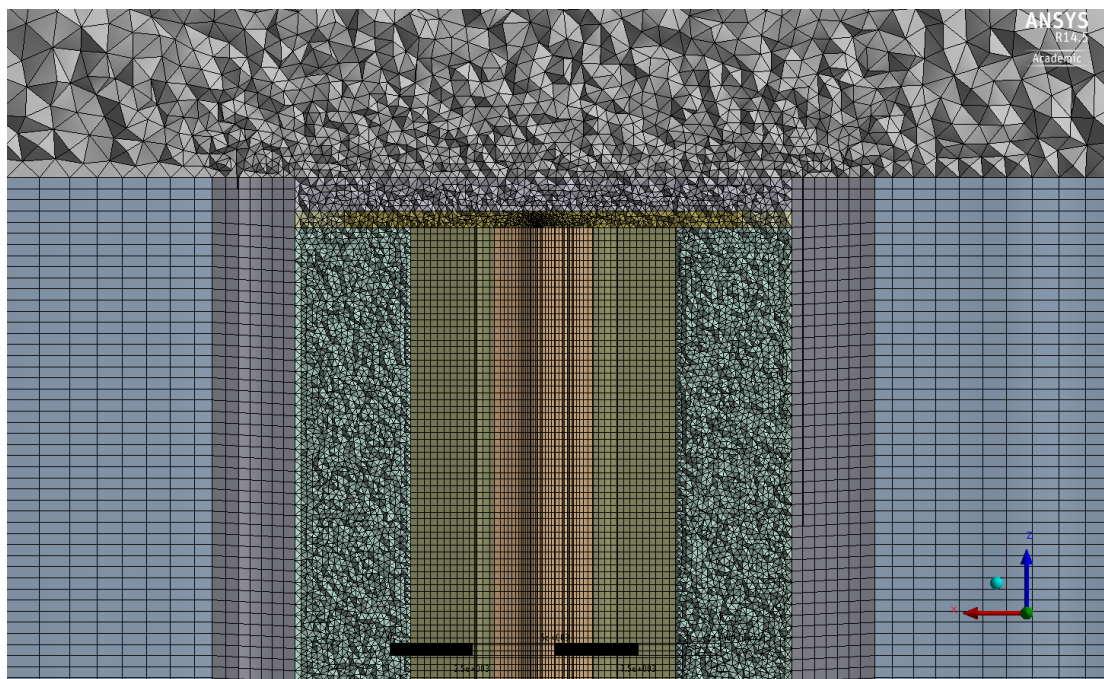
obtain a solution of the Reynolds-Averaged Navier-Stokes (RANS) equations [18] together with the $k-\omega$ SST turbulence model [29]. A cylindrical domain was created with an inlet placed three diameter ($30m$) in front of the first turbine and an outlet placed six diameter ($60m$) behind the second turbine as shown in Figure 4.9. The ground effect was not included as it would incur an unnecessary additional computational cost and previous work has showed that including the ground effects without a shear inflow only increased power production by 0.4%, and adding a shear inflow increased this further to 5.5% [156].

4.4.2 Mesh

This particular study used a mixed hybrid mesh with unstructured tetrahedral cells in the shear layer region at the edge of the wake and structured hexahedral cells everywhere else, as shown in Figure 4.10 which shows how the mesh was divided into different zones of refinement. A mesh study was conducted on the six diameter domain using five different mesh densities ranging from 2 million to 80 million cells (5 million to 15 million nodes). The mesh densities were created by varying the refinement within the tip region of the wake as shown in Table 4.2.



(a)



(b)

Figure 4.10: Mesh refinement zones

Nodes (million)	Cells (million)	Tip refinement
5	22	-
6	29	0.2m
11	37	0.2m
12	54	0.15m
15	80	0.125m

Table 4.2: Various mesh densities and tip refinement.

Figure 4.11(a) shows the velocity profiles of the five different meshes at 70m downstream of the first turbine and Figure 4.11(b) shows a more detailed view of the maximum velocity deficit showing the small difference between the different mesh densities. The velocities are within 5% of each other, with the greatest difference between the coarsest two meshes of 22 million and 37 million cells. Figure 4.12 shows the velocity difference between the 22 million and 37 million cell mesh along the yz plane through the centre of the domain. It shows that the main difference is within the second wake but it is only approximately 2% of the free stream velocity. The greatest difference is at the disc location mostly due to the differences in the mesh causing a slightly different force smoothing on the second turbine. Table 4.3 shows the differences in computational time while using 20 partitions divided between four 2.66GHz Intel Xeon X5550 computers, which were part of UCLan’s High Performance Computer (HPC) Wildcat cluster¹.

The mesh with 22 million cells and 5 million nodes was chosen for the remainder of the study, with a six diameter spacing, as the difference between the five mesh densities was small in terms of the velocity profile (within 5% as shown in Figure 4.12) and it was determined that the other meshes densities were not worth the additional computational expense as shown in Table 4.3. The simulations featuring a three diameter spacing were conducted with a similar dimensioned domain resulting in an overall

¹www.hpcavf.uclan.ac.uk

Nodes (million)	Cells (million)	Wall clock time	File size
5	22	< 1hour	2.4GB
6	29	≈ 1 hour	3.1GB
11	37	1.5 hours	5GB
12	54	2 hours	6GB
15	80	3 hours	8GB

Table 4.3: Computational time for various mesh densities

shorter domain reducing the cell and nodes to 17 million cells and 3 million nodes.

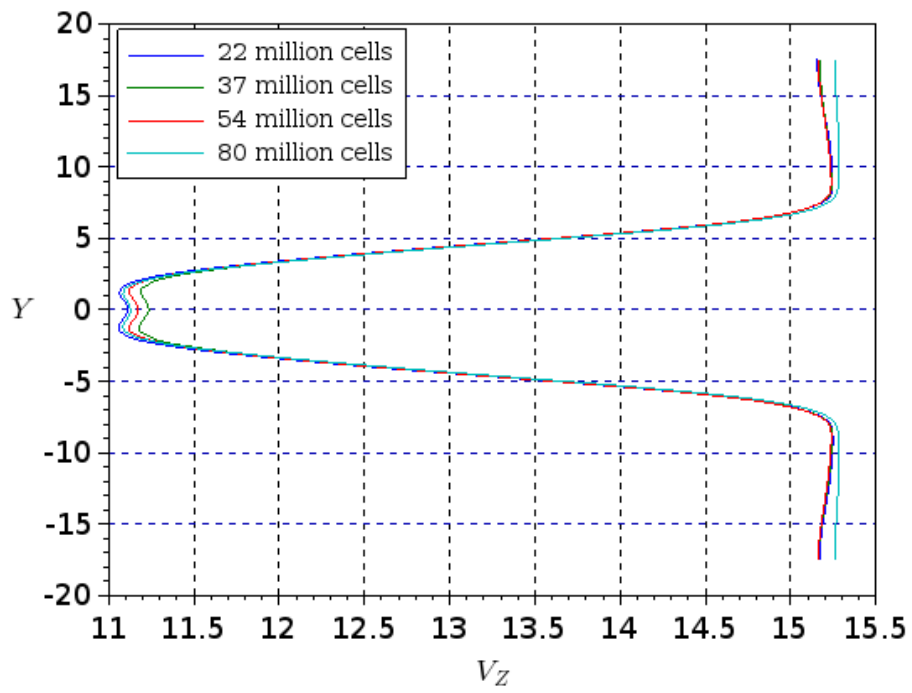
4.4.3 Boundary conditions

For this study four wind speeds of 7m/s, 10m/s, 15m/s and 20m/s were simulated as these represent important speeds, such as cut in and rated speeds, and there are significant data from NREL Phase VI project [85] for these speeds. The inlet was defined with a constant velocity and turbulence intensity of 5%. The walls of the domain were defined as free slip walls and the outlet was defined as a static pressure outlet with a relative pressure of zero.

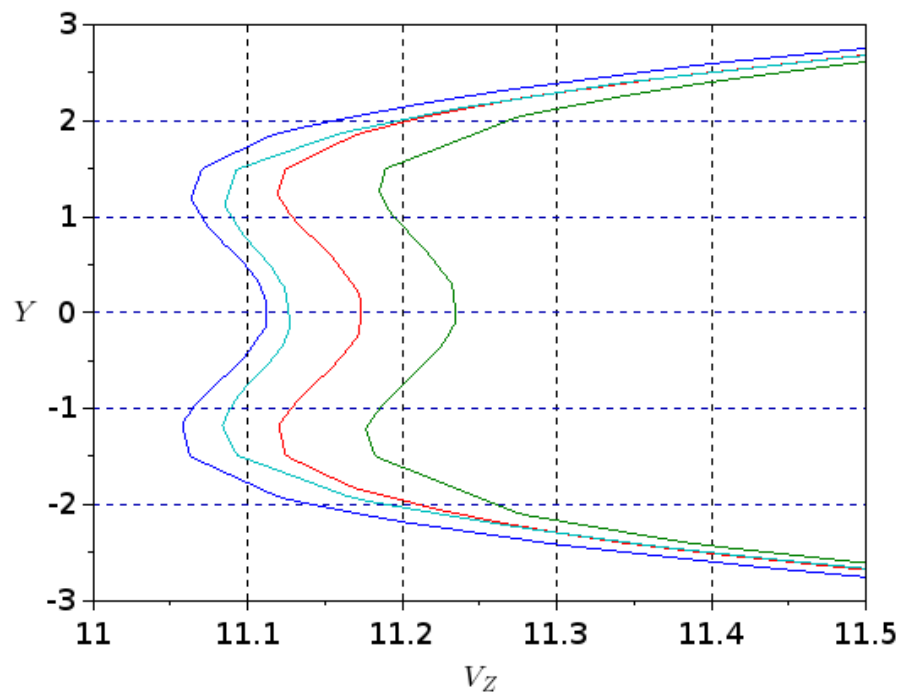
The actuator disc is used in this study for both turbines as described in subsections 2.2.2 and 3.5.1, with the force exerted calculated using equations (2.70)-(2.72). The aerodynamic coefficients used (such as lift and drag) were taken from the NREL Phase VI project data [85]. The actuator disc was used instead of the actuator line due to the reduced computational resources required and the number of simulations desired.

4.4.4 Repeatability study

A repeatability study was conducted as part of this study, where the mesh generation and solution were calculated multiple times using the same parameters. For this study the mesh containing 22 million cells and 5 million nodes was used with a wind speed of 15m/s, as this wind speeds showed the greatest variation in the single actuator study



(a)



(b)

Figure 4.11: Mesh comparison (a) 70m behind the first turbine and (b) detail view of the velocity deficit

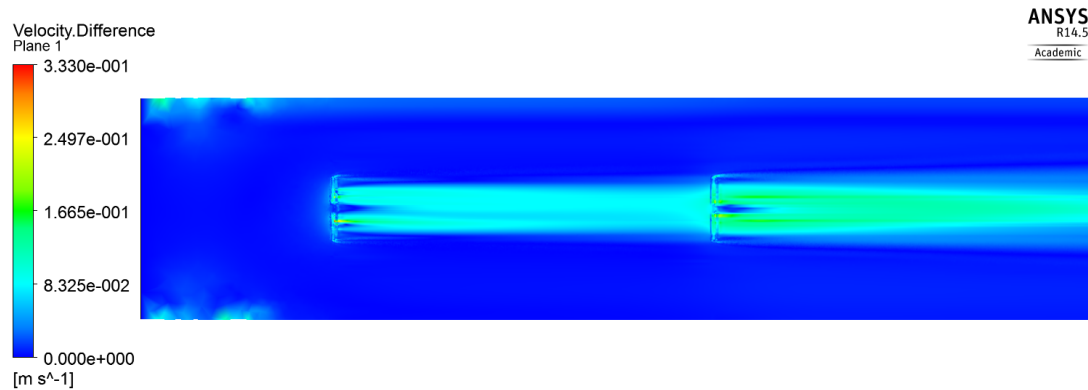


Figure 4.12: Velocity difference between the 22 million and 37 million cell mesh densities

(§5.3). The study involved defining the mesh and boundary conditions of four separate simulations and clearing all generated data before recreating the mesh and calculating each simulation individually.

4.5 Rotor diameter study

This study investigated the influence rotor diameter size has on wind turbine wakes and the aerodynamic performance on a downwind turbine. It has been proposed by Steinbuch *et al.* [202] and Johnson & Thomas [203], as well as shown experimentally by Adaramola & Krogstad [196], that the second turbine's performance can be significantly improved by operating the first turbine outside optimum tip speed ratio. This would require monitoring and learning by trial and error [203] to get the most out of the wind-farm. It would be more beneficial if the same effect could be achieved without the constant need for monitoring. Chowdhury *et al.* [8] showed that a wind-farm featuring different size turbines could produce 10% more power than one with identical turbines. This particular study [8] was limited to a single case using an analytical flow model [204]. Due to this it is necessary to conduct a more detailed study into how the rotor diameter effects the energy yield of a wind-farm.

To investigate the effect that rotor diameter has on wake interactions, six turbine configurations were investigated each featuring two axially aligned turbines. The first turbine featured three different diameters of 7.5m, 10m and 12.5m while the second turbine always featured a 10m diameter rotor. These turbine sizes were chosen with the 10m NREL phase VI turbine [85] as a starting point due to the amount of data and previous work available. The other sizes were chosen to represent possible size variations of full size turbines (i.e. 75m, 100m and 120m) which are currently on the market that are rated with similar power allowing for wind-farms to be constructed using different rotor diameters without significant loss of power.

The turbines in this study are all based on the 10m NREL phase VI turbine [85] with three blades. All aerofoil coefficients and sizes are extrapolated from the original 10m NREL phase VI turbine [85]. This study has investigated an axially aligned layout featuring two spacings of 30m and 60m for the same reasons as described in section 4.4. Apart from the different rotor diameters all other aspects are in line with the two turbine study as described in section 4.4.

Chapter 5

Results

This chapter details the results obtained from the five studies detailed in Chapter 4.

5.1 One-dimensional momentum theory results

This section details the results of the comparative study carried out between CFD simulations carried out using ANSYS-CFX and the one-dimensional momentum theory, as described in section 4.1.

The porous disc and actuator disc methods have been compared with the one-dimensional (1D) momentum theory, as described in subsection 3.1.1 and the reference [95], specifically the pressure and velocity profiles along the centre line of the rotor. The 1D momentum theory, also known as the simple actuator theory, is an application of the momentum equation applied to an idealized turbine. It uses control volume analysis to consider an infinitely thin frictionless disc with a constant momentum sink within an inviscid and incompressible fluid. Figure 5.1(a) shows the pressure and velocity profiles given by the 1D momentum equation. Figure 5.1(b) shows the pressure and velocity profiles produced by a constantly loaded actuator disc without rotation, defined using the thrust coefficient (C_T). The overall profiles are in good agreement,

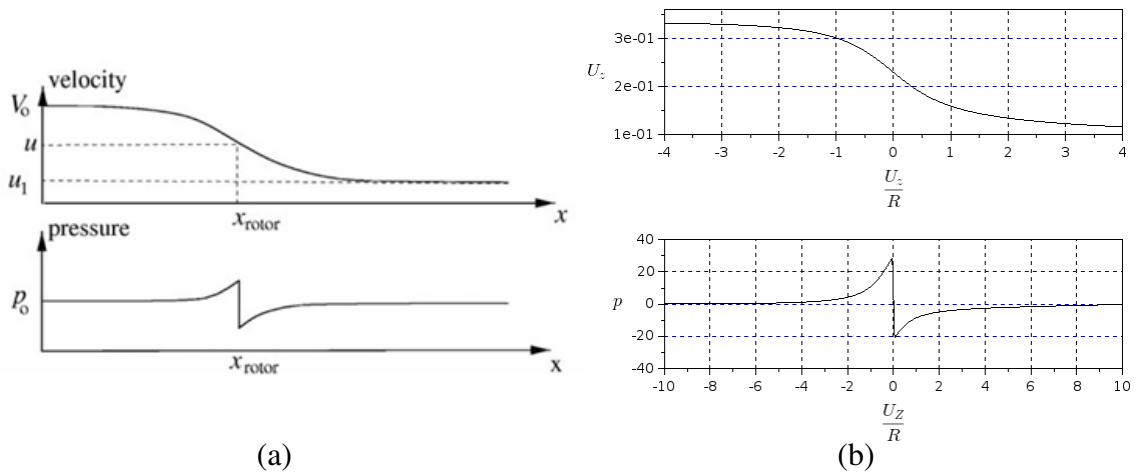


Figure 5.1: Pressure and velocity profiles along the centre line of the rotor given by (a) the 1D momentum theory and (b) the actuator disc method

with only the magnitudes of the plot changing, depending on the C_T value and the characteristics of the disc as expected.

5.2 Porous disc Results

This section details the results of the porous disc study which was detailed in section 4.2. Simulations were carried out of a porous disc within a water channel and compared to the results obtained by previous numerical [140][141] and experimental [184][185] studies. The experimental data [184][185] was measured using an Acoustic Doppler Velocimeter (ADV).

All the data presented in this study was produced using ANSYS-CFX and calculated with a root-mean-square residual of 1×10^{-5} applied to the RANS equations, which was in line with the reference [141]. The velocities were compared to both previous numerical and experimental results which were normalized using the free stream velocity of the flow described between $0.5 < y/2R < 2.5$ at the inlet which was 0.331m/s in the experimental study [185], 0.337m/s in the reference [141] and 0.33m/s

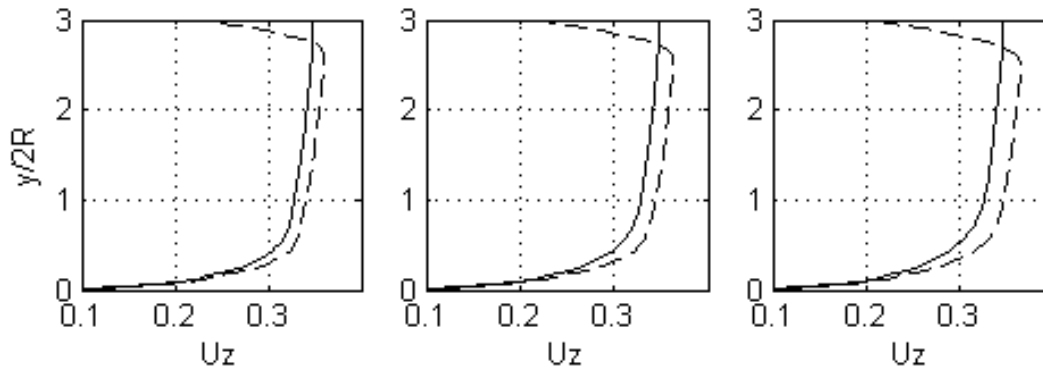


Figure 5.2: Velocity profile with no disc of the channel flow (solid line) and the duct flow (dashed line) at 24m, 31m and 40m from the inlet

in the work described in this study. This range was used as there was no experimental data beyond this range. The vertical height was also normalized using the diameter of the disc ($2R$).

5.2.1 Influence of the boundary conditions

Before detailing the results of the wake study, a comparison of the effects of the boundary types is needed. To do this the same domain and mesh was setup excluding the momentum loss to observe how the velocity profiles develop without the influence of the discs. Figure 5.2 shows the differences between the channel (solid lines) and duct (dashed lines) velocity profiles as they develop through the domain. The figure shows how the channel flow is almost unchanged as the inlet was defined with a channel velocity profile. The duct profile changes significantly as expected with the additional wall boundary causing a sharp decrease in velocity at the top of the domain which forces the central velocity to increase to maintain the same mass flow rate.

5.2.2 Wake predictions

The experimental study [185] conducted experiments using discs with different porosity measurements to represent different values of the thrust coefficient (C_T). C_T is a non

dimensional variable used to describe a rotor's characteristics. The greater C_T value the greater the wake expansion and turbulence levels within the wake due to increased momentum deficit. The C_T values of the porous discs in the experimental study [185] were measured using a pivot arm attached to a load cell. The thrust coefficient can be described numerically using equation (5.1). It requires the thrust (T) to be estimated which can be achieved in a number of ways. In the reference [141] the thrust coefficient was estimated from the results using equation (5.2) to define the thrust. However in this work, as in the reference [140], the thrust was calculated using equation (5.3),

$$C_T = \frac{T}{\frac{1}{2}\rho U_0^2 A_r} \quad (5.1)$$

$$T = \frac{\rho}{2} K U_r |U_r| A_r \quad (5.2)$$

$$T = \Delta p A_r \quad (5.3)$$

where T is the thrust, ρ is the density, U_0 the free stream velocity, A_r is the disc area, K is the resistance coefficient, U_r is the velocity at the rotor and Δp is the change in pressure over the centre of the disc.

Table 5.1 shows the C_T values of the previous experimental and numerical studies compared to the values calculated in this study. It shows that the channel simulations conducted as part of this study have the closest C_T values compared to the experimental data. It also shows that the C_T values predicted by the duct simulations have the least agreement with the experimental data [185].

Figure 5.3 shows the velocity profiles along the centre line of the domain and shows good agreement for all simulations in terms of the velocity characteristics. The velocity deficit is over-predicted when compared to the numerical [141] and experimental data [185] for inlet 1, which has a delayed velocity recovery and appears to be offset from

Disc number	Study			
	Experimental [185]	Numerical [141]	Channel	Duct
1	0.61	0.65	0.60	0.64
2	0.86	0.91	0.86	0.93
3	0.97	0.98	0.93	1.00

Table 5.1: Thrust coefficient results to 3 s.f.

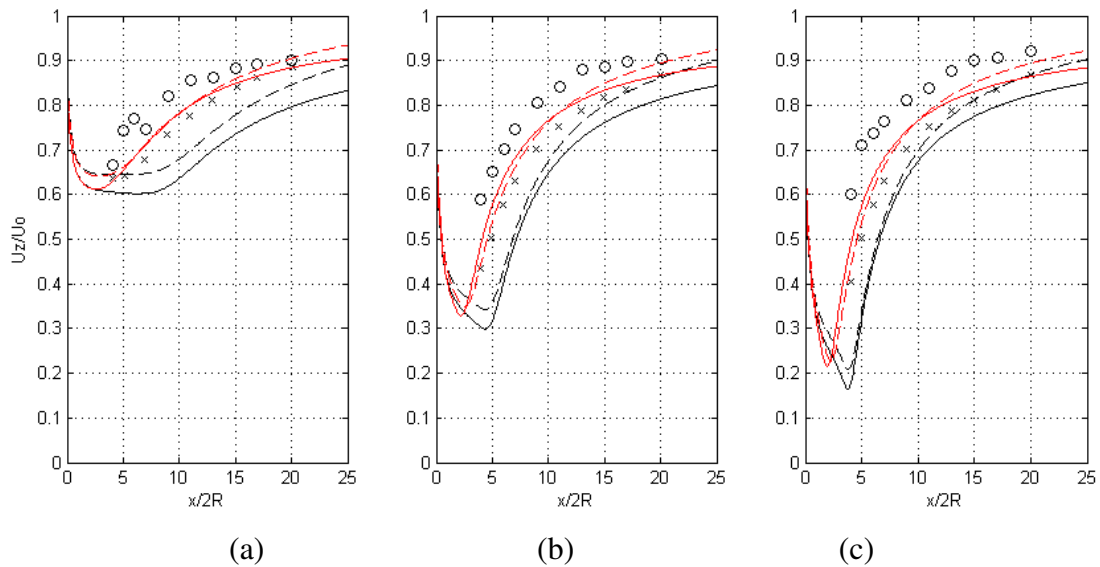


Figure 5.3: Velocity along the centre line showing the channel (solid line), duct (dashed line), numerical (x) [141] and experimental data (o) [185] for the C_T values of a) 0.61, b) 0.86 and c) 0.97 for the experimental study [185]. The inlet 1 simulations are shown in black and inlet 2 simulations are in red

the other data sets. Inlet 2 shows a much better prediction of the experimental data [185] and both inlets show the duct had increased velocity recovery than the channel simulation (discussed in §§6.1.3).

Figure 5.4 shows the turbulent intensity along the centre line of the domain and the difference between inlet 1 and 2 (described in §§4.2.2), with inlet 1 having a lower starting turbulence intensity and subsequent peak. Both inlets show very little change in turbulent intensity just behind the rotor and then an almost linear increase up to the maximum intensity. This increase is most likely due to the presence of the wake edge shear layer, with the maximum turbulent intensity indicating the merger of the

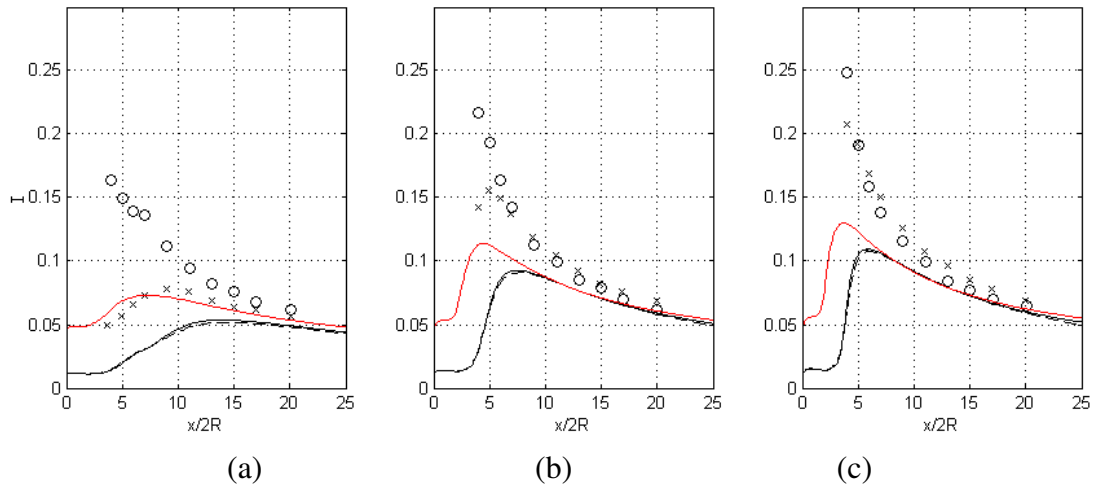


Figure 5.4: Turbulence intensity along the centre line showing the channel (solid line), duct (dashed line), numerical (x) [141] and experimental data (o) [185] for the C_T values of a) 0.61, b) 0.86 and c) 0.97 for the experimental study [185]. The inlet 1 simulations are shown in black and inlet 2 simulations are in red.

layers and subsequent end of the near wake region (discussed in §§6.2.1). The near wake region of the flow, which is defined behind the disc up until the wake edge shear layers meet at the centre line of the wake, creating a peak in turbulence. The near wake region varies in distance generally from 2 to 8 diameters downstream, depending on the disc geometry and flow conditions. Figure 5.4 shows that the model is able to predict the intensity accurately far down stream of the disc. Although, it is unable to predict the peak in the turbulence intensity behind the rotor both in terms of magnitude and location (discussed in §§6.2.1).

Figures 5.5 and 5.6 show the velocity and turbulence intensity profiles at various distances downstream of the disc and for the three different discs. The distances downstream correspond to 8R, 14R, 22R, 30R and 40R downstream of the disc. These locations were chosen as they coincide with the locations used in the experimental study [185].

For all profiles in Figure 5.5 agreement was achieved¹ for the majority of the profile characteristics, such as the locations of highest and lowest velocities with the main

¹at least from a qualitative viewpoint

numerical discrepancy at the maximum velocity deficit for all simulations. While the initial velocity drop is over-predicted at the centre, the free stream and floor boundary layer features are predicted well. Figure 5.5 shows that the duct simulations predicted a smaller velocity deficit at the centre of the wake and higher velocity towards the boundaries than the channel simulations (discussed in §6.1.3).

Figure 5.5 shows how the velocity deficit of the experimental data recovers more than the numerical data with inlet 1 simulations showing the least recovery. The experimental data seems to have an almost constant velocity by 22R downstream and completely recovers by 30R downstream, whereas all numerical simulations still show some velocity deficit at 40R (discussed in §6.2.1).

Figure 5.6 shows the turbulence intensity of the models in comparison with the experimental data. There is little difference between the solid and dashed lines representing the channel and duct flows respectively; with all models predicting intensities below that of the experiment data (discussed in §6.2.1). The figure shows how the experimental data peaks earlier and higher than the modelled numerical data. Beyond approximately 22R downstream of the rotor the modelled and experimental data are very close and almost the same by 40R .

5.2.3 Cell type study results

This section details the results of a comparative study which investigates the differences between linear and quadratic mesh cells (without and with mid-side nodes, shown in Figure 4.4)[35][186]. The study was conducted using inlet 1. This study compared 10 different mesh densities, shown in Table 5.2, using both ANSYS-CFX and ANSYS-Fluent. Table 5.2 shows the quadratic mesh calculations took 48-186% longer to solve than their linear equivalent.

Figures 5.7 and 5.8 shows the velocity profiles of the different mesh densities

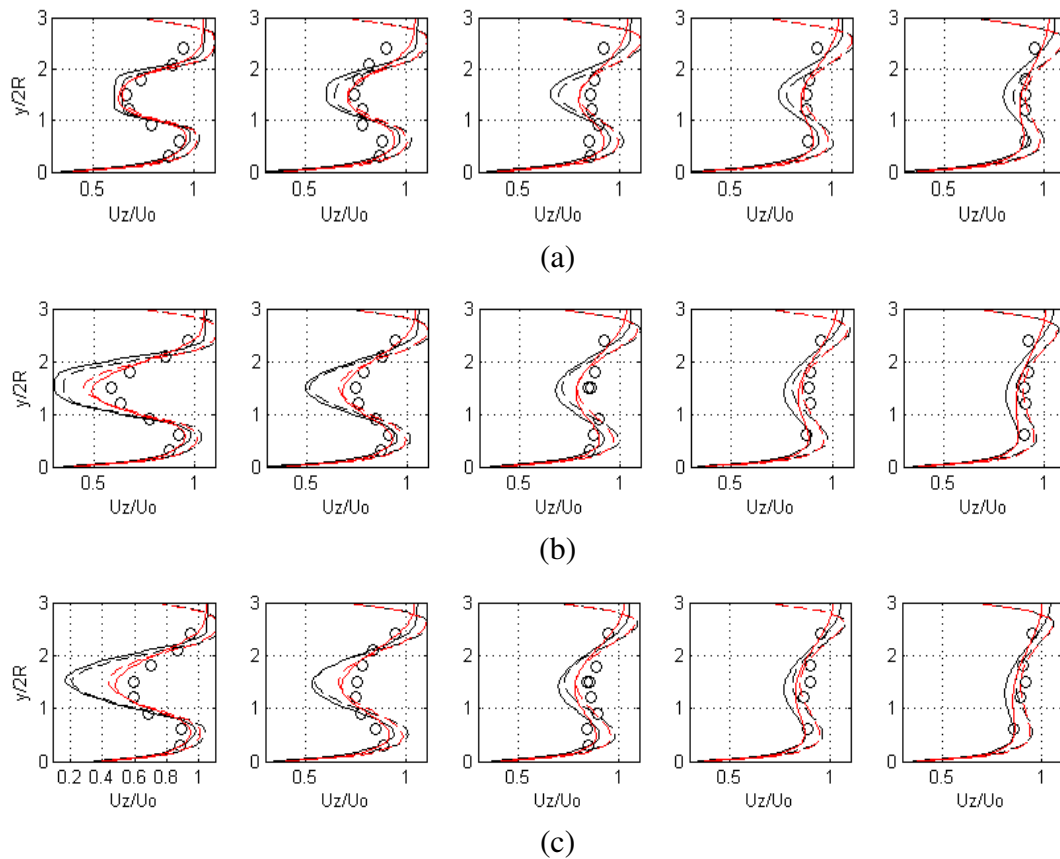


Figure 5.5: Normalized velocity of the channel (solid line), duct (dashed line) and experimental data (o) [185] at different C_T values of a) 0.61, 0.62, b) 0.86, 0.91 and c) 0.97, 0.99 for this study and the experimental study respectively [185]. The inlet 1 simulations are shown in black and inlet 2 simulations are in red. Each figure represents the distance downstream of the disc corresponding to 8R, 14R, 22R, 30R and 40R respectively

Cells $\times 10^6$	Nodes $\times 10^6$		Time [mins]		Iterations	
	linear	quadratic	linear	quadratic	linear	quadratic
1.36	0.466	2.64	11	17	63	104
1.57	0.513	2.96	13.5	20	63	105
2.42	0.694	4.22	19.5	31	62	106
3.44	0.959	6.08	21	60	54	151
4.38	1.38	7.81	30	75	54	149

Table 5.2: Mesh densities using linear and quadratic cell types

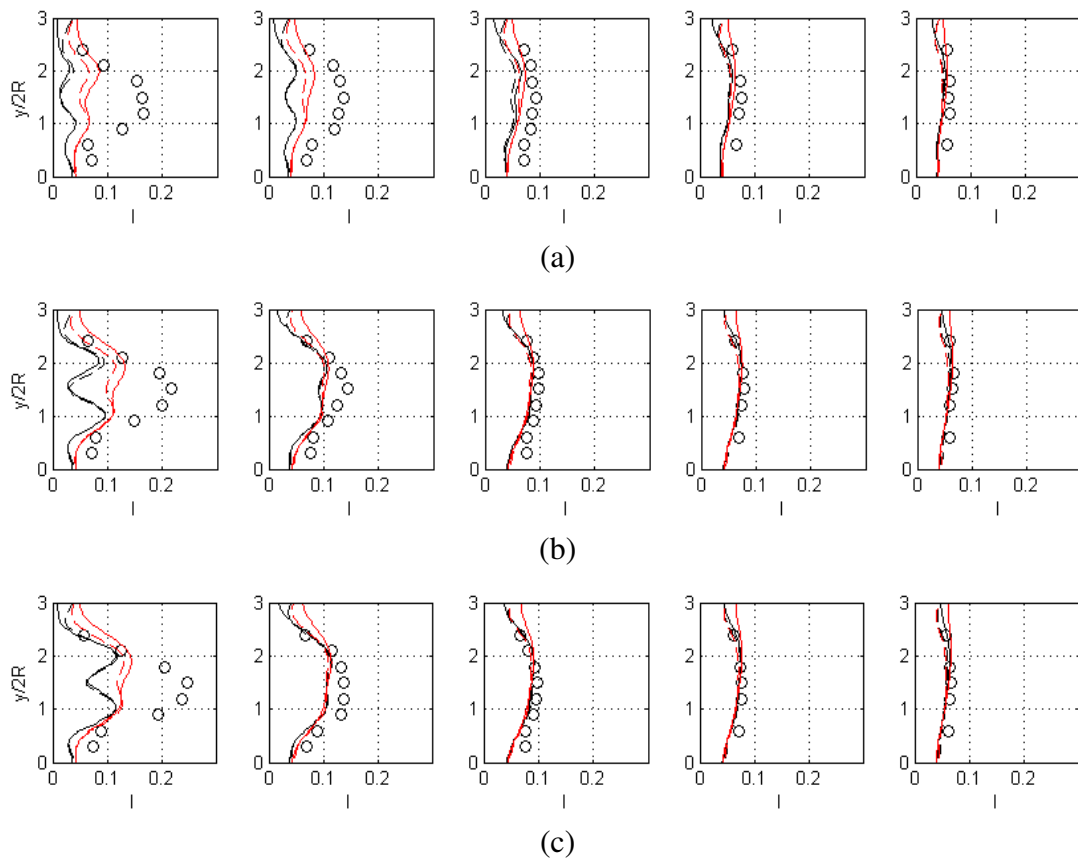


Figure 5.6: Turbulence intensity at 8R, 14R, 22R, 30R and 40R downstream of the disc, with the channel (solid line), duct (dashed line) and experimental data (o) [185] at different C_T values of a) 0.61, 0.62, b) 0.86, 0.91 and c) 0.97, 0.99 for this study and the experimental study respectively [185]. The inlet 1 simulations are shown in black and inlet 2 simulations are in red

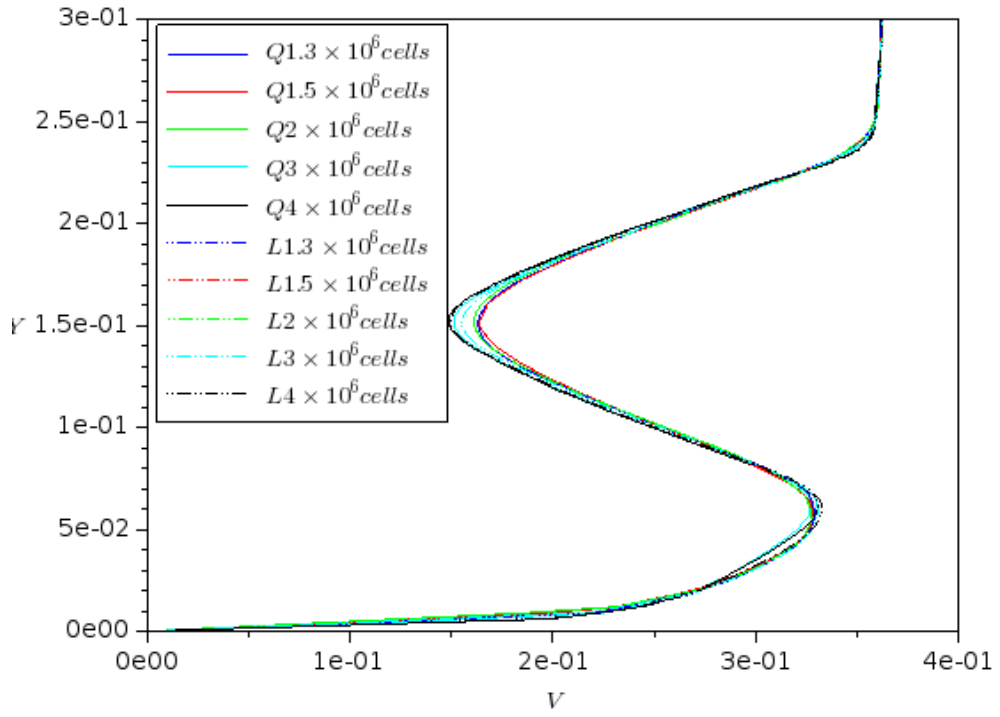
7 diameters behind the disc for both the duct and channel simulations predicted by ANSYS-Fluent. Figure 5.7(a) shows the velocity profile of all 10 mesh density. It shows that the largest variation is at the highest velocity deficit at the centre of the wake and that for each cell density there is little change in velocity profile. Figure 5.7(b) is a refined view of the velocity profiles showing that for each cell density the quadratic cell version predicted a higher velocity deficit although no quadratic cell density predicts a higher velocity deficit than a finer linear cell density. Figure 5.8 shows very similar results to the channel simulations. Figure 5.9 shows the turbulence intensity through the centre of the domain behind the disc and that there is a variation in the turbulence predicted by each mesh although this is less than 3%.

5.2.4 Code comparison results

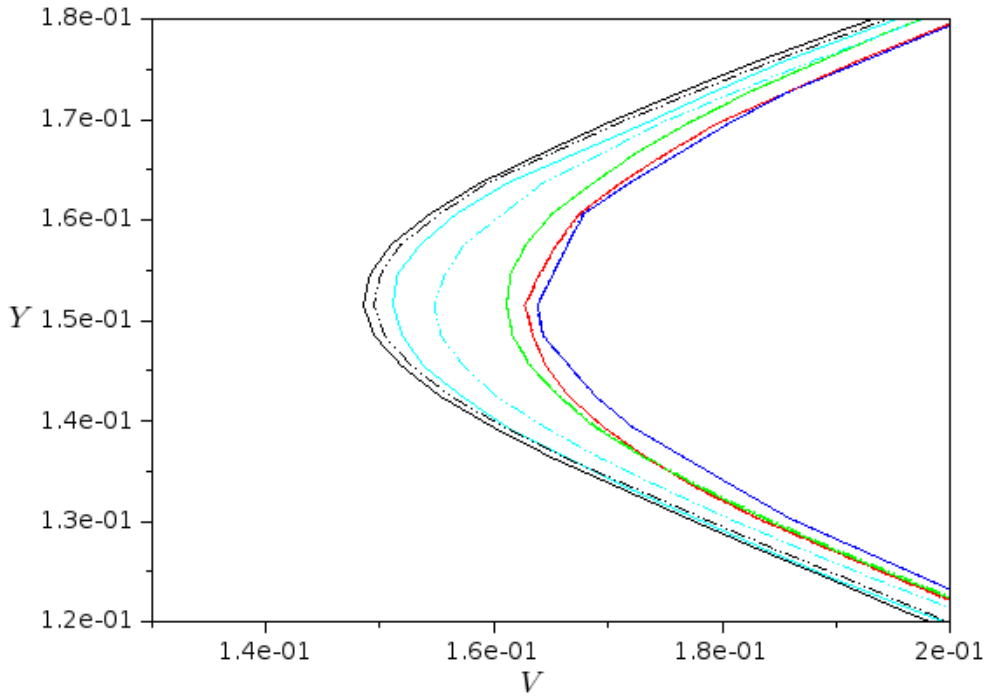
This section details the results of a code comparison between ANSYS-CFX and ANSYS-Fluent. Both codes simulated analogous models of a porous disc within a water channel, specifically the disc with a resistance of 2.

Figure 5.10 shows the normalized velocity profile through the centre of the domain of ANSYS-CFX (red) and ANSYS-Fluent (blue) simulations for the channel (solid line) and duct (dashed line) simulations as well as the experimental study (o) [185]. Figure 5.10 shows that ANSYS-CFX and ANSYS-Fluent predict a very similar velocity profile although both over-predict the velocity deficit compared to the experimental data. The similarity between the two profiles is closest just behind the disc and it diminishes as the wake develops. ANSYS-CFX predicts the highest velocity deficit of all data sets at $\frac{x}{2R} = 2$ and predicts the longest wake recovery. The duct simulation performed by ANSYS-Fluent seems to predict a velocity profile closest to the experimental data [185] within the far wake.

Figures 5.11 and 5.12 show normalized velocity profiles behind the disc at various

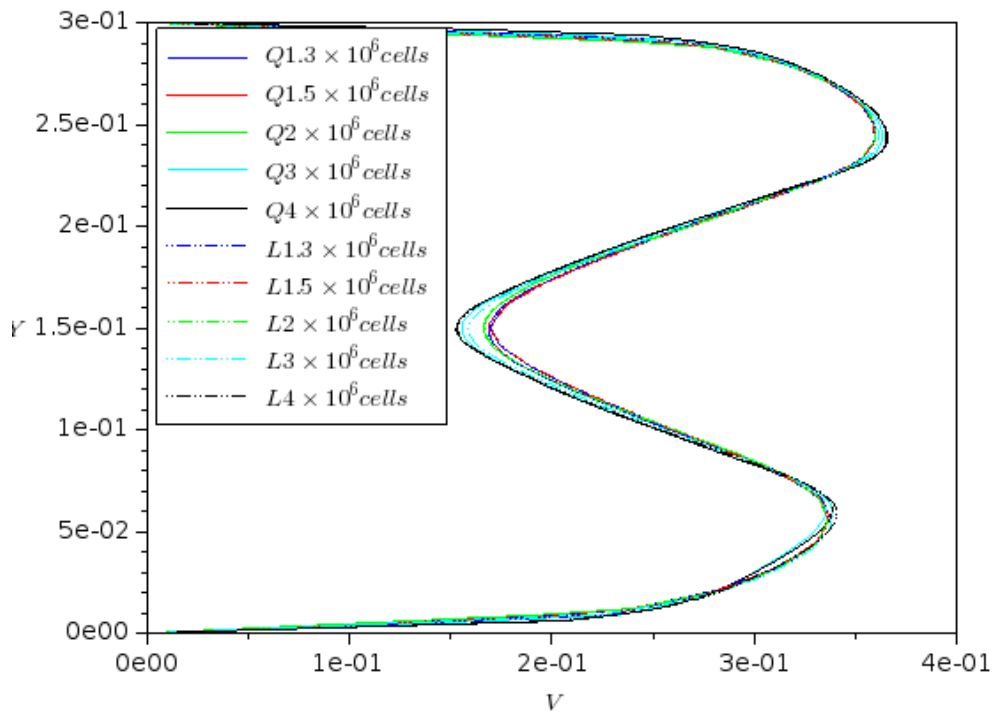


(a)

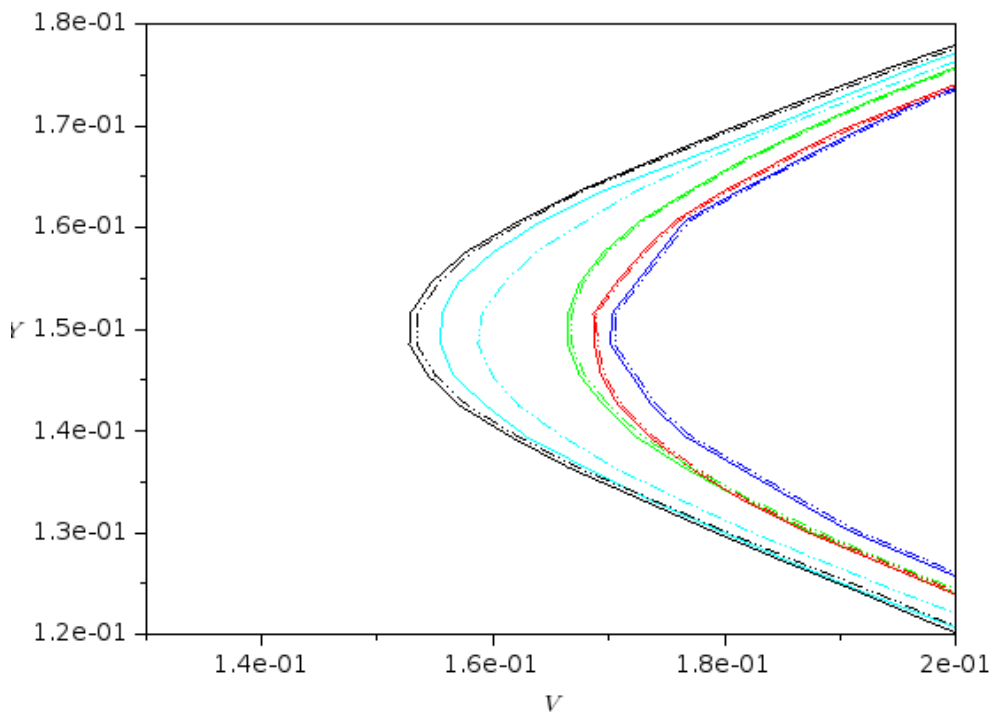


(b)

Figure 5.7: Velocity profile 7 diameters behind the disc of the channel simulations with the quadratic cells (solid line) and linear cells (dashed line)



(a)



(b)

Figure 5.8: Velocity profile 7 diameters behind the disc of the duct simulations with the quadratic cells (solid line) and linear cells (dashed line)

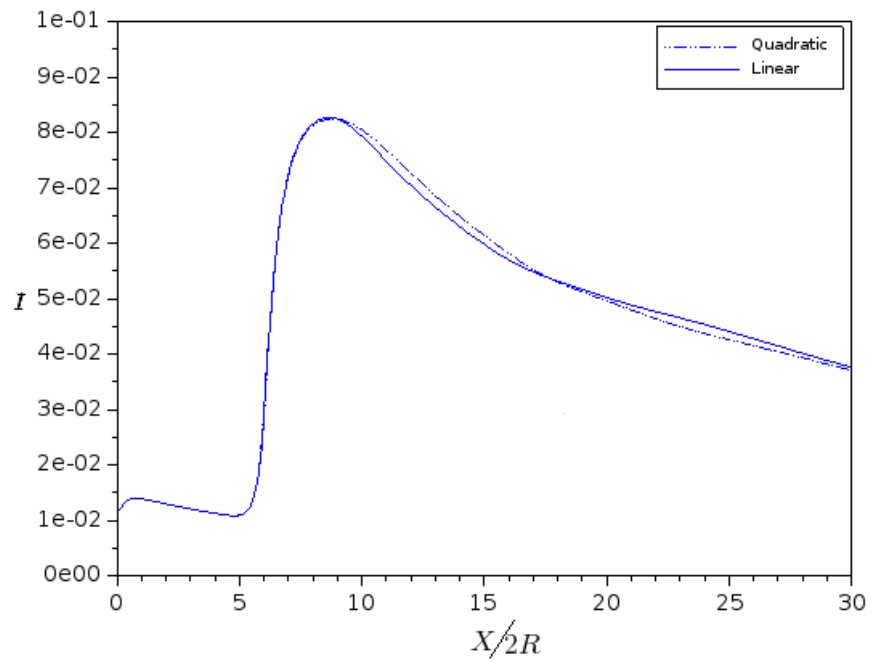


Figure 5.9: Normalized turbulence intensity behind the disc

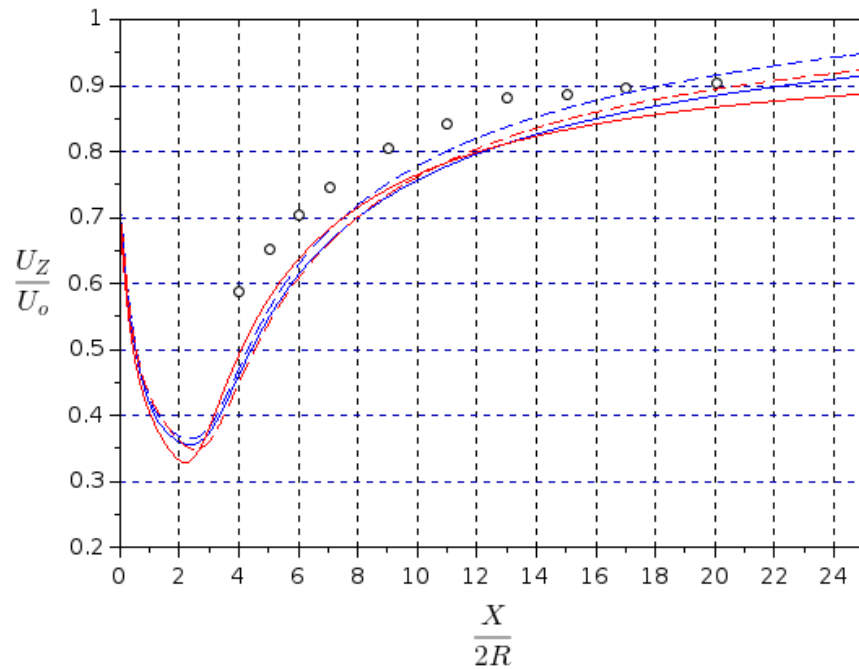


Figure 5.10: Normalized velocity profile through the centre of the domain with ANSYS-CFX (red), ANSYS-Fluent (blue) and experimental data (o) [185] for the channel (solid line) and duct (dashed line) simulations

locations. They show the results from ANSYS-CFX (red) and ANSYS-Fluent (blue) for the channel (solid line) and duct (dashed line) simulations as well as the experimental study (o) [185]. Figure 5.11 shows the velocity profile four diameters behind the disc and the difference between the channel and duct velocity profiles. ANSYS-CFX predicts a larger difference in velocity within the boundary layer of the two simulations of approximately $10\% \frac{y}{2R} = 0.5$ away from the edge. Whereas, ANSYS-Fluent predicts an almost identical velocity profile until $\frac{y}{2R} = 0.5$ when the velocities sharply diverges and predicts a higher velocity at the roof of the channel simulation. The channel simulation of ANSYS-CFX seems to be the closest to the experimental data [185] at this location. Figure 5.12 shows the velocity profiles at various locations behind the disc and that the differences between the channel and duct simulations has more of an impact downstream of the disc with the development of the boundary layer of the duct simulation. Figures 5.12(c) and 5.12(d) particularly show that as the boundary layer develops the differences between the two velocity profiles increases and extends into the wake.

Figure 5.13 shows the turbulence intensity through the centre of the domain with ANSYS-CFX (red) and ANSYS-Fluent (blue) for the channel (solid line) and duct (dashed line) simulations as well as the experimental study (o) [185]. It shows that ANSYS-CFX predicts a higher turbulence intensity than ANSYS-Fluent for $2 < \frac{X}{2R} < 8$ and that ANSYS-CFX predicts a lower turbulence intensity for the duct simulation. ANSYS-Fluent predicts near identical turbulence intensity for both channel and duct simulations. Apart from these discrepancies ANSYS-CFX and ANSYS-Fluent predicted similar turbulence intensity although both under-predict the intensity of the experimental data [185] until well into the far wake at $\frac{X}{2R} < 17$.

Figures 5.14 and 5.15 show the turbulence intensity behind the disc at various locations with ANSYS-CFX (red) and ANSYS-Fluent (blue) for the channel (solid line) and duct (dashed line) simulations as well as the experimental study (o) [185]. Figure

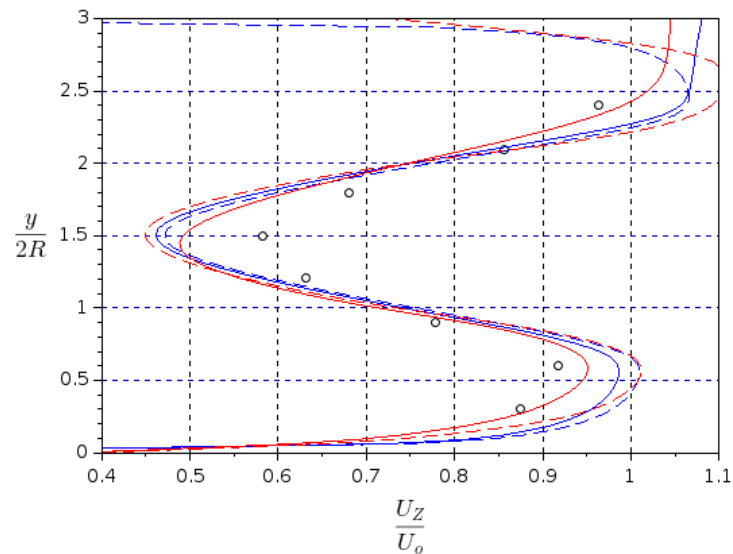


Figure 5.11: Normalized velocity profile behind the disc at $\frac{x}{2R} = 4$ with ANSYS-CFX (red), ANSYS-Fluent (blue) and experimental data (o) [185] for the channel (solid line) and duct (dashed line) simulations

5.14 shows the velocity profile four diameters behind the disc and shows that ANSYS-Fluent predicts very similar turbulence intensity for both channel and duct simulations within the roof boundary layer. ANSYS-CFX predicts similar turbulence intensity below $\frac{x}{2R} = 1$ although above this the two turbulence profiles differ with the channel simulation having a higher intensity. Both ANSYS-Fluent and ANSYS-CFX predict turbulent intensity peaks at the edge of the wake although neither predict the peak at the centre of the wake which was observed in the experimental study [185]. Figure 5.15 shows the turbulence intensity at locations further behind the disc and shows that further downstream the turbulence intensity peaks at the edge of the wake which reduces to an almost uniform intensity. The variation between the channel and duct simulations also diminish for the bottom half of the domain with a clear difference at the roof of the domain. It shows that the turbulence intensity of the experimental data [185] reduces quicker than the numerical data although at approximately $\frac{x}{2R} = 15$ all the data sets produce similar turbulence intensities.

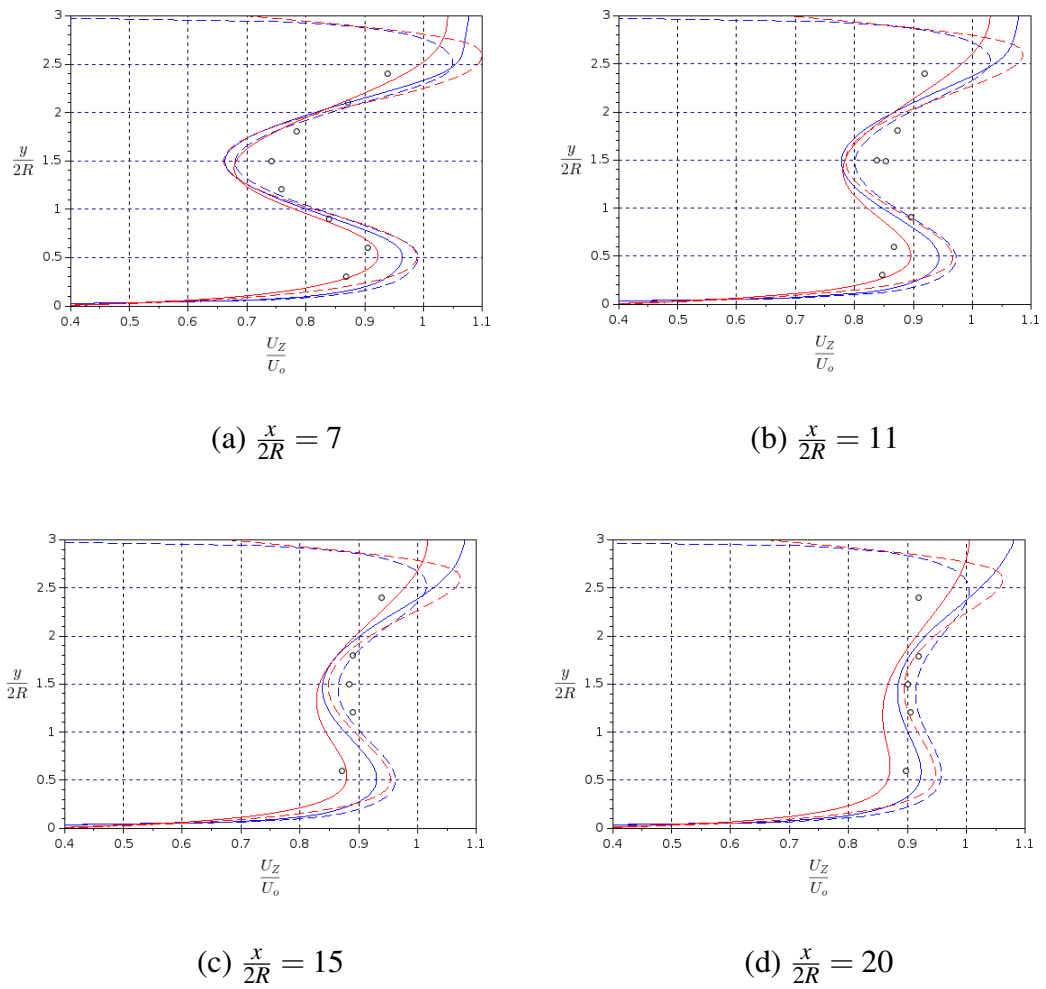


Figure 5.12: Normalized velocity profile behind the disc with ANSYS-CFX (red), ANSYS-Fluent (blue) and experimental data (o) [185] for the channel (solid line) and duct (dashed line) simulations

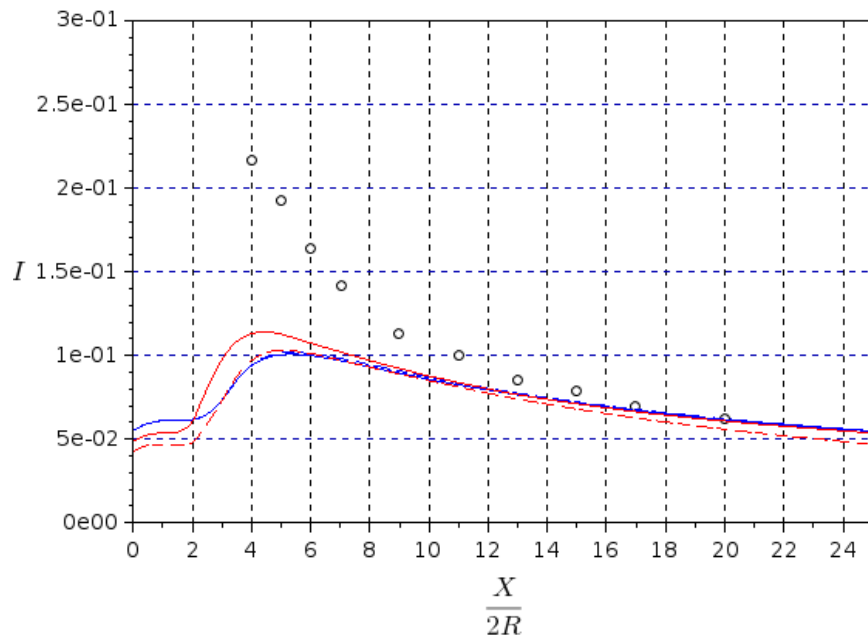


Figure 5.13: Turbulence intensity through the centre of the domain with ANSYS-CFX (red), ANSYS-Fluent (blue) and experimental data (o) [185] for the channel (solid line) and duct (dashed line) simulations

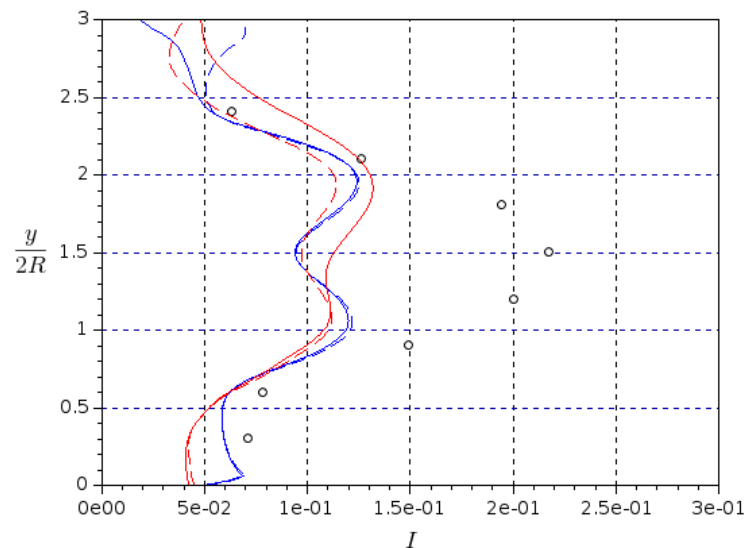
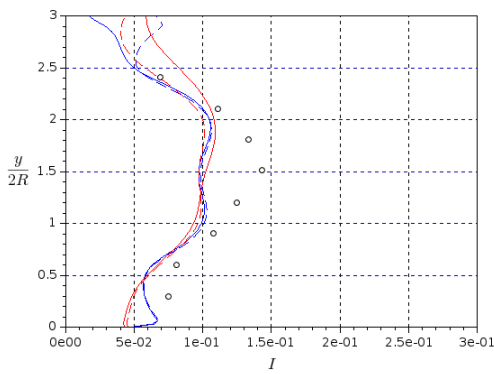
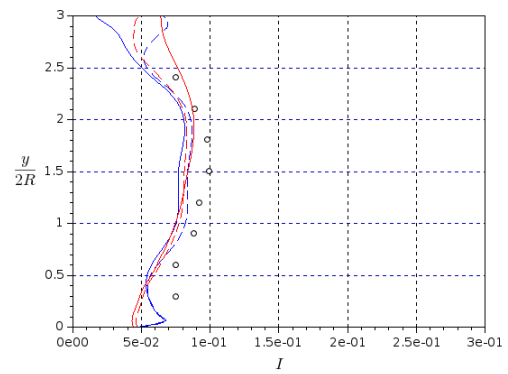


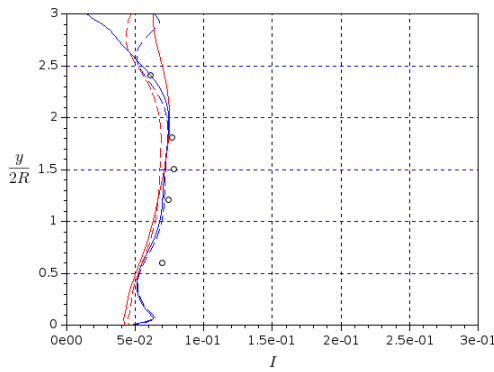
Figure 5.14: Turbulent intensity behind the disc at $\frac{x}{2R} = 4$ with ANSYS-CFX (red), ANSYS-Fluent (blue) and experimental data (o) [185] for the channel (solid line) and duct (dashed line) simulations



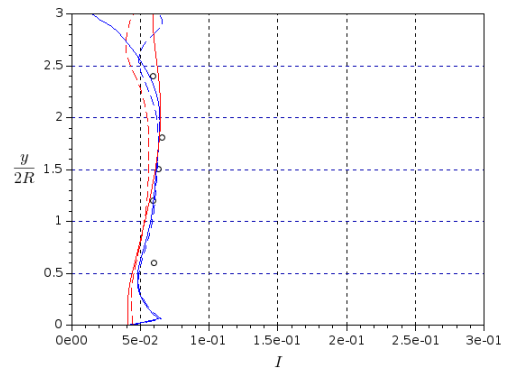
(a) $\frac{x}{2R} = 7$



(b) $\frac{x}{2R} = 11$



(c) $\frac{x}{2R} = 15$



(d) $\frac{x}{2R} = 20$

Figure 5.15: Turbulence intensity behind the disc with ANSYS-CFX (red), ANSYS-Fluent (blue) and experimental data (o) [185] for the channel (solid line) and duct (dashed line) simulations

5.3 Actuator disc study results

This study reproduced the EU FP5 project 'Model EXperiments In COntrolled COnditions' or 'MEXICO' project as discussed in section 4.3 and detailed in the reference [106]. In this section the actuator disc (AD) method, which was used to simulate the turbine, is compared with the experimental MEXICO data [118][119] and a previous numerical study [120].

Figure 5.16 shows the velocity profile through the centre of the domain at hub height offset in the horizontal (z direction) by 1.84797m or $z/R = 0.82132$. It shows the velocity for each wind speed 10m/s (blue), 15m/s (green) and 24m/s (red) for this study (solid line), previous numerical study (o) [120] and the experimental data (.) [106]. It shows that all three data sets show a similar velocity profile although the numerical studies do not have as steep a drop as the experimental data [118][119] just behind the turbine (discussed in §6.2.1). Both numerical studies under-predict the velocity deficit within the wake for all but the slowest wind speed. The data produced in this study predicts the highest velocity of all three data sets even before the turbine, shown in Figure 5.17. The greatest variation in velocity between the data sets is within the wake of the 15m/s wind speed.

Figures 5.18 and 5.19 show the normalized cross-sectional velocity profiles at various locations throughout the domain. They show the normalized data from the 10m/s simulation although the data was normalized based on the inlet velocities used as described in section 4.3. Figure 5.18 shows the velocity profile at $x/R = 0.4$ before the turbine. It shows very good agreement between the two numerical studies with the highest difference at the edge of the velocity stream.

Figure 5.19 shows the normalized velocity profiles at six locations downwind of the turbine produced by this study (blue) and previous numerical study [120]. It shows the characteristics of the velocity profiles of the two numerical studies are in good

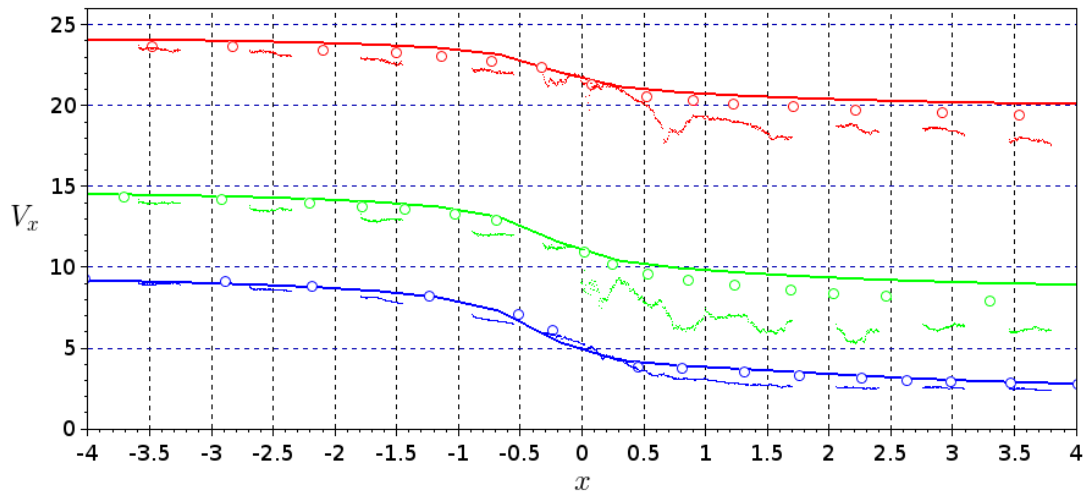


Figure 5.16: Velocity profile through the centre of the domain at $1.84797m$ or $z/R = 0.82132$ for this study (solid line), experimental data (.) [106] and previous numerical study (o) [120] for three inlet velocities

agreement for all locations. The velocity away from the wake and the wake expansion is also in very good agreement for all locations. The discrepancy between the two studies is at the velocity magnitude towards the edge and centre of the wake. This study shows a higher velocity deficit at the edge of the wake then the previous study [120] for all locations except the furthest downwind. At the centre of the wake this study predicts little to no velocity deficit but the previous study [120] predicts their highest velocity deficit here (discussed in §§6.2.2).

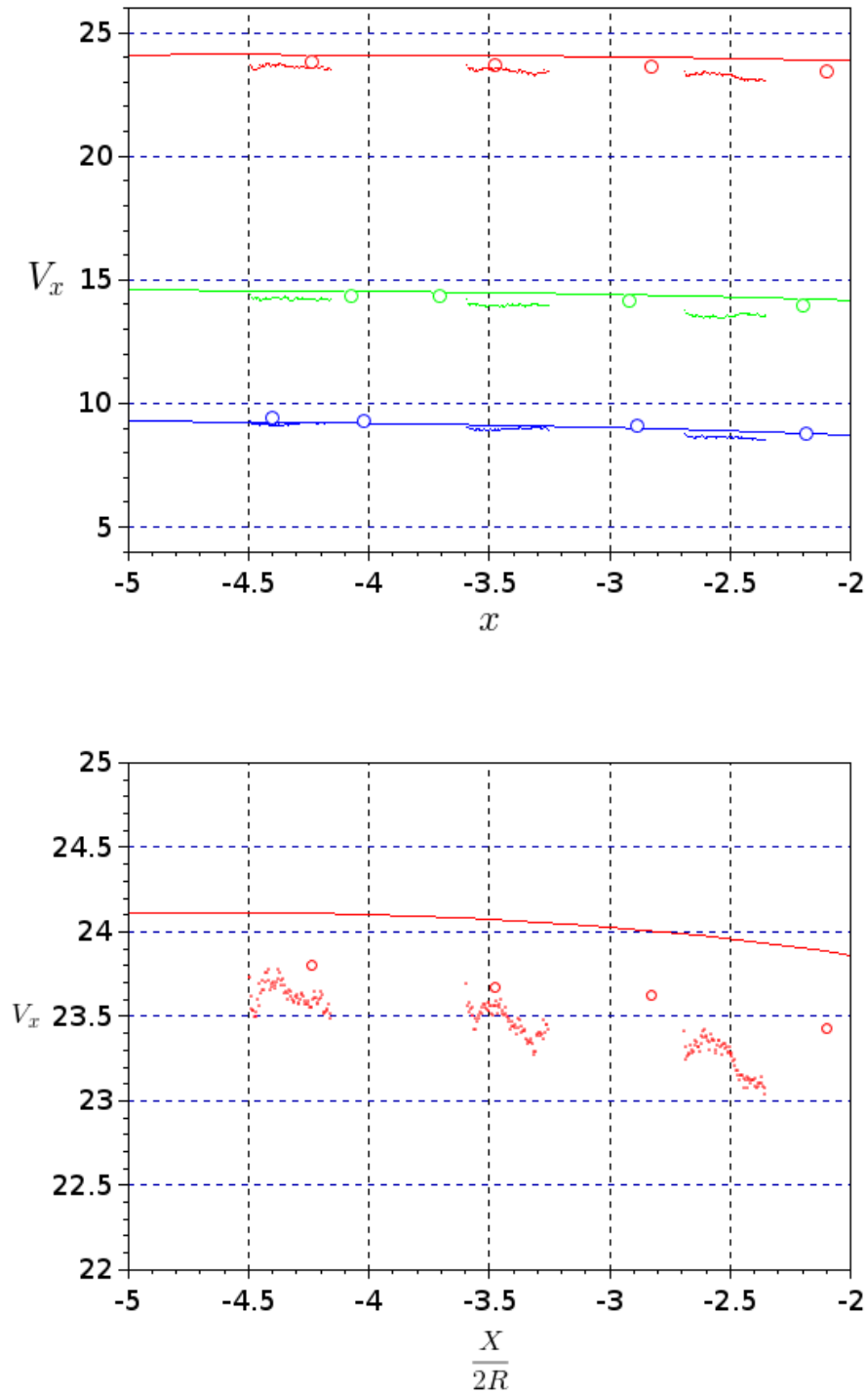


Figure 5.17: Velocity variation towards the inlet for this study (solid line), experimental data (.) [106] and previous numerical study (o) [120]

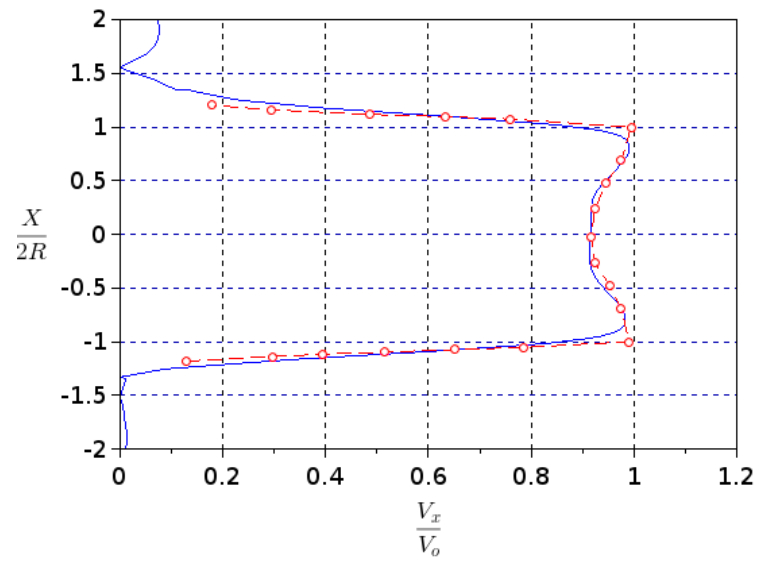


Figure 5.18: Normalized velocity profile at $x/2R = -0.4$ with this study (blue) and previous numerical study [120] (red o)

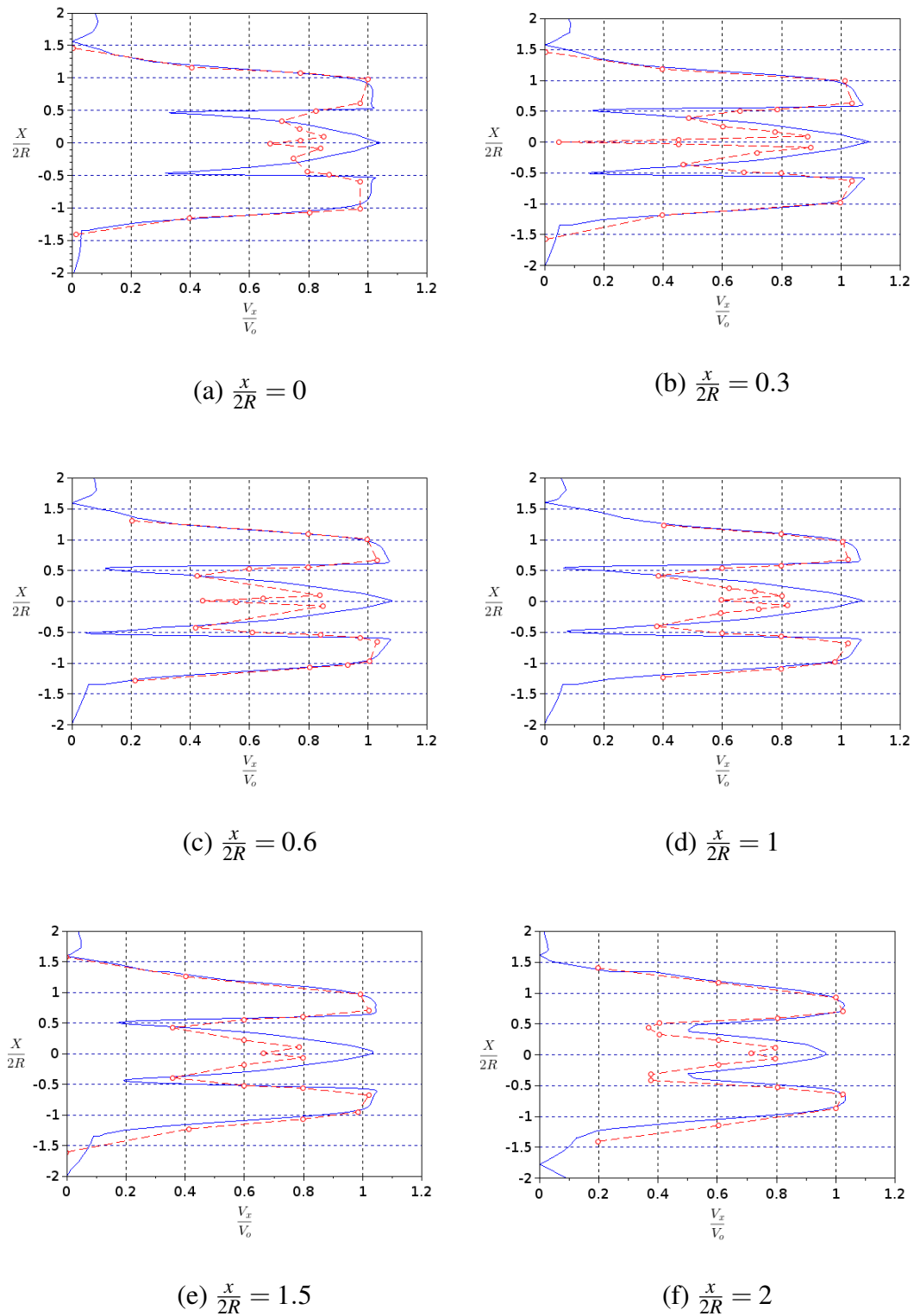


Figure 5.19: Normalized velocity profiles of this study (blue) and previous numerical study [120] (red o) at various locations

5.4 Two turbine study results

This study investigates the interactions between two wind turbines. It features two 10m NREL phase VI turbines [85] but with three blades, aligned with a spacing between them of three and six diameters. The domain, mesh and boundary conditions used in this study were discussed in section 4.4. All the data presented in this section were calculated using ANSYS-CFX with a mesh containing 22 million cells (5 million nodes) and the simulations had converged to a root-mean-square residual of 1×10^{-6} unless otherwise stated. The data produced has been compared with two previous studies, an experimental [197] and a numerical [195]. The data used for comparison are normalized based on the inlet velocity and turbine radius. Although four wind speeds have been simulated only the 7m/s simulation was compared as it is closest to the other studies [197][195] in terms of the tip speed ratio (5.5). The simulated data for the other wind speed was however used in section 5.5.

Figure 5.20 shows the normalized velocity profiles downstream of two turbines spaced 3 diameters apart where the solid line is the work described in this study, (o) and (x) represent numerical data at 5% and 10% ambient turbulence intensity [195] and (*) represents experimental data [197]. The velocity profiles are at 50m, 60m and 70m respectively downwind of the first turbine. There is good agreement between the results of this study with previous studies at 50m and 60m. There is less agreement at 70m particularly at the centre of the wake although the edge of the wake remains in good agreement.

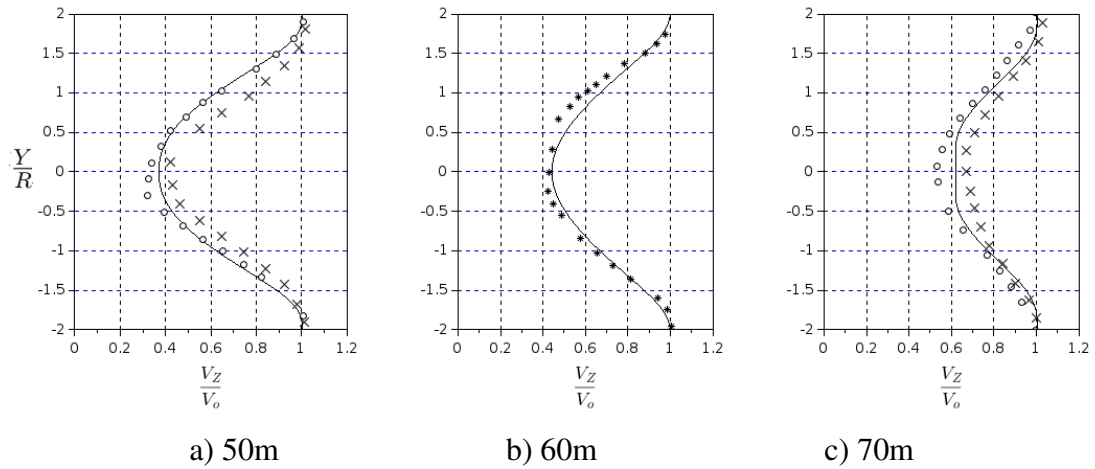


Figure 5.20: Normalized velocity profiles at 50m, 60m and 70m downstream respectively of the first turbine with this study (solid line), previous numerical data at 5% (o) and 10% (x) ambient turbulence [195] and experimental data (*) [197]

Simulation number	Cells	Nodes
1	4878311	22065456
2	4878455	22065941
3	4880487	22063055
4	4887175	22095389

Table 5.3: Mesh variation in the repeatability study

5.4.1 Repeatability study results

A repeatability study was carried out where the mesh generation and solution were calculated multiple times using the same parameters. Table 5.3 shows the mesh density of each simulation and that each mesh was similar with a variation of 8864 cells and 32334 nodes, which is a variation of less than 0.2%. Figure 5.21 shows the velocity difference between simulation 1 and 4, which had the largest mesh variation, along the yz plane through the centre of the domain and Figure 5.22 shows the region around the disc showing the highest difference is at the disc location. It shows that the variation in mesh density had little effect on the velocity field producing a maximum variation of 1%.

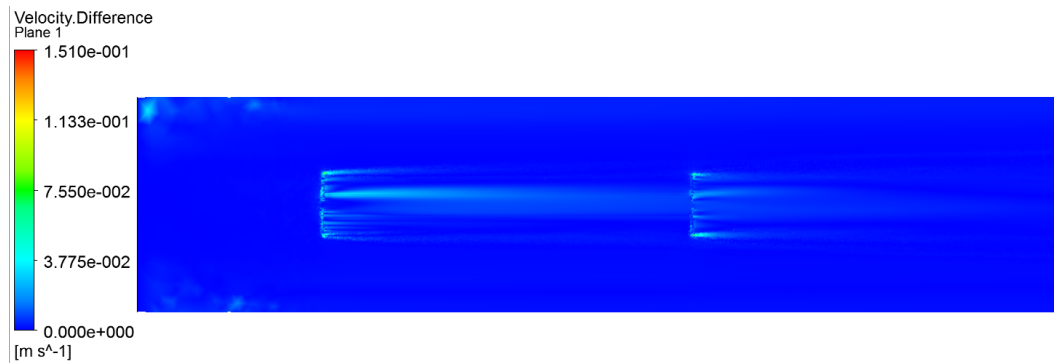


Figure 5.21: Velocity difference along yz plane between two simulations used in the repeatability study

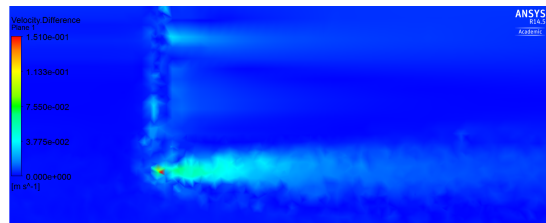


Figure 5.22: Detailed view of the velocity difference

5.5 Rotor diameter study results

This study investigated the influence rotor diameter size has on wind turbine wakes and the aerodynamic performance on a downwind turbine. The turbines in this study were all based on the 10m NREL phase VI turbine [85] with three blades. Here two aligned turbines with spacings of 30m and 60m are simulated. The first turbine features three different diameters of 7.5m, 10m and 12.5m which were 30m away from the inlet while the second turbine always featured a 10m diameter rotor. All the data presented in this section was calculated using ANSYS-CFX with a mesh containing 22 million cells (5 million nodes) and the simulations had converged to a root-mean-square residual of 1×10^{-6} unless otherwise stated. Apart from the different rotor diameters all other aspects are in line with the two turbine study as described in section 4.5.

The power of each turbine can be calculated using equation (5.4). In this study an approximate power extracted by the turbine has been calculated using the average

velocity at the rotor and a power coefficient (C_p) of 0.4, which was used as the normal range for a wind turbine is between 0.35-0.45 [205].

$$P = \frac{1}{2} \rho \pi r^2 u^3 C_p. \quad (5.4)$$

Where ρ is the air density, r is the rotor radius, u is the wind speed which in this situation is the average velocity at the rotor and C_p is the power coefficient.

To investigate the effect rotor diameter has on turbine interactions a baseline needs to be established. In this case it was the two 10m turbines simulated in section 5.4 and unless otherwise stated, any comparison is made in regard to this configuration.

5.5.1 First turbine

Before the interactions between the turbines is analysed the performance of the first turbine is considered. Figure 5.23 shows the velocity profiles at the first turbine for each wind speed with the 7.5m turbine (blue), 10m turbine (green) and 12.5m turbine (red). Table 5.4 shows the average velocity at the rotor of the first turbine. Figure 5.23 and Table 5.4 show that as the rotor diameter increases the average velocity measured at the rotor decreased as expected as more momentum is extracted from the flow.

Table 5.5 shows the approximate power extracted by the first turbine, using equation (5.4), and shows that as the rotor diameter increases so does the power extracted, as expected. Table 5.6 shows the difference in the amount of power extracted and percentage difference of the 7.5m and 12.5m turbines compared to the 10m turbine. Each rotor has a rotor diameter of 7.5m, 10m and 12.5m and hence swept area corresponding to 44.2m^2 , 78.5m^2 and 123m^2 respectively. Tables 5.4 - 5.6 show that as the rotor diameter increases the power extracted increases even though the average velocity at the rotor decreases.

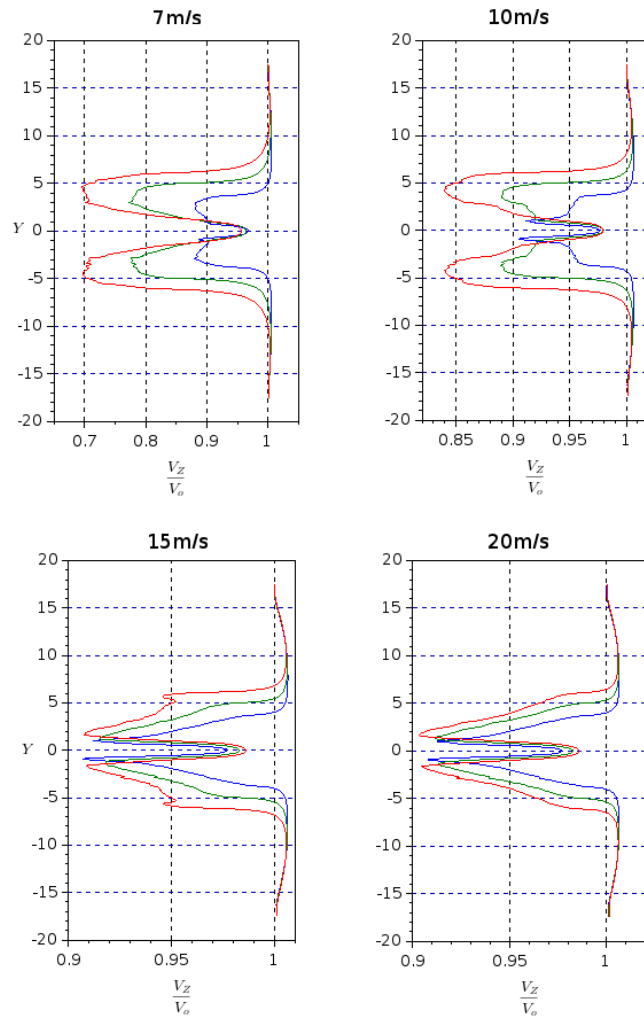


Figure 5.23: Velocity profiles at the first turbine for each wind speed of 7m/s, 10m/s, 15m/s and 20m/s respectively and the different colours represent the different turbine configurations; 7.5m turbine (blue), 10m turbine (green) and 12.5m turbine (red)

Wind speed [m/s]	Rotor size [m]		
	7.5	10	12.5
7	6.30	5.91	5.63
10	9.42	9.17	8.98
15	14.2	14.2	14.1
20	18.9	18.9	18.9

Table 5.4: Velocity at the first turbine to 3 s.f.

Wind speed [m/s]	Rotor size [m]		
	7.5	10	12.5
7	2660	3890	5250
10	8870	14500	21200
15	30400	53500	82900
20	71900	127000	199000

Table 5.5: Approximate power extracted by the first turbine to 3 s.f.

5.5.2 60m spacing wake

This subsection details the results of the 12 simulations where the spacing between the two turbines was 60m specifically looking at the wake and velocities. Figure 5.24 shows the velocity profiles at 70m downwind of the first turbine and/or 10m behind the second turbine. Each turbine configuration is shown in a different colour where the velocity behind the 7.5m turbine is blue, behind the 10m turbine is green and behind the 12.5m turbine is red. It shows that the turbine behind the 7.5m turbine experiences the smallest velocity deficit and the turbine behind the 12.5m turbine experiences the highest velocity deficit. It shows that the wake behind the 12.5m turbine is widest and the wake behind the 7.5m turbine is the narrowest. Figures 5.25 and 5.26 show the velocity profiles through the centre of the domain offset by 4m and 2m respectively showing the velocity behind the 7.5m (blue), 10m (green) and 12.5m (red) turbines. They show the velocity profiles reducing due to the turbine and then slowly recovering as expected and that the velocity recovers quicker after the second turbine compared to the first with the velocity behind the 7.5m turbine constantly higher than the other

Wind speed [m/s]	Rotor size [m]			
	7.5	% deficit	12.5	Factor
7	1240	31.8	1360	1.35
10	5670	39.0	6700	1.46
15	23100	43.2	29400	1.55
20	55000	43.3	72200	1.57

Table 5.6: Power difference of the first turbines compared with the baseline to 3 s.f.

turbines.

5.5.3 60m spacing second turbine velocity

Figure 5.27 shows the normalized velocity profiles at the rotor of the second turbine for each wind speed. It shows that the greatest velocity variation is along the blade section of the rotor approximately 4m off centre and for the 10m/s wind speed. The least variation is found around the centre of the rotor where the hub would be located approximately less than 1m from the centre. Table 5.7 shows the average velocity at the second rotor for each wind speed. Table 5.8 shows the difference in average velocity both in magnitude and percentage, of the 7.5m and 12.5m turbines compared to the 10m turbine. Tables 5.7 and 5.8 show the greatest velocity magnitude difference is at 10m/s and smallest is at 15m/s for all turbines. The greatest velocity percentage difference is at 7m/s and that increasing the wind speed decreases this percentage difference. The greatest average velocity at the rotor for each wind speed was always experienced by the turbine behind the 7.5m turbine by a minimum of 4% of the free stream wind speed.

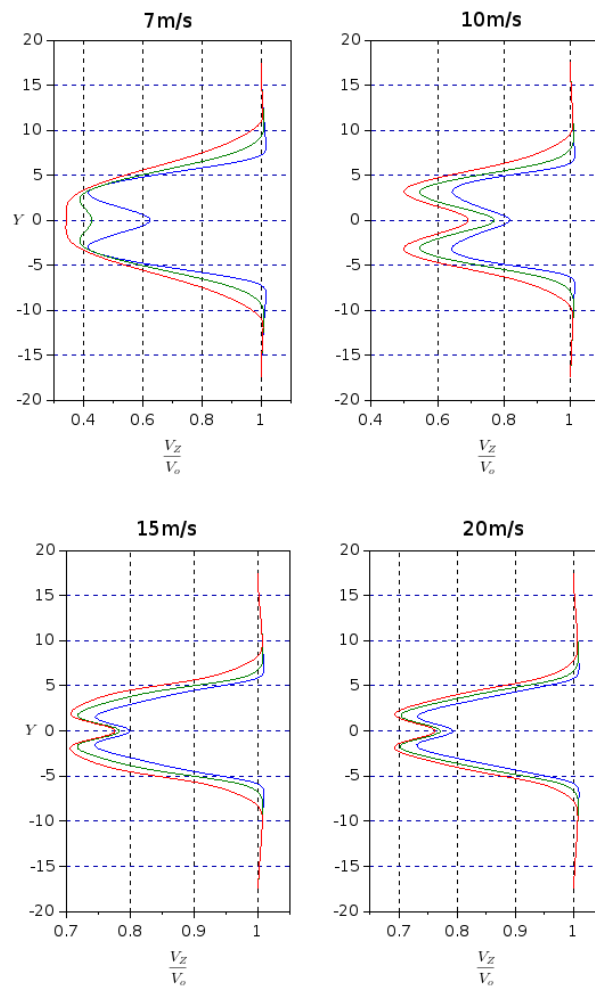


Figure 5.24: Velocity at 70m behind the first turbine for each wind speed of 7m/s, 10m/s, 15m/s and 20m/s respectively and the different colours represent the different turbine configurations; 7.5m turbine (blue), 10m turbine (green) and 12.5m turbine (red)

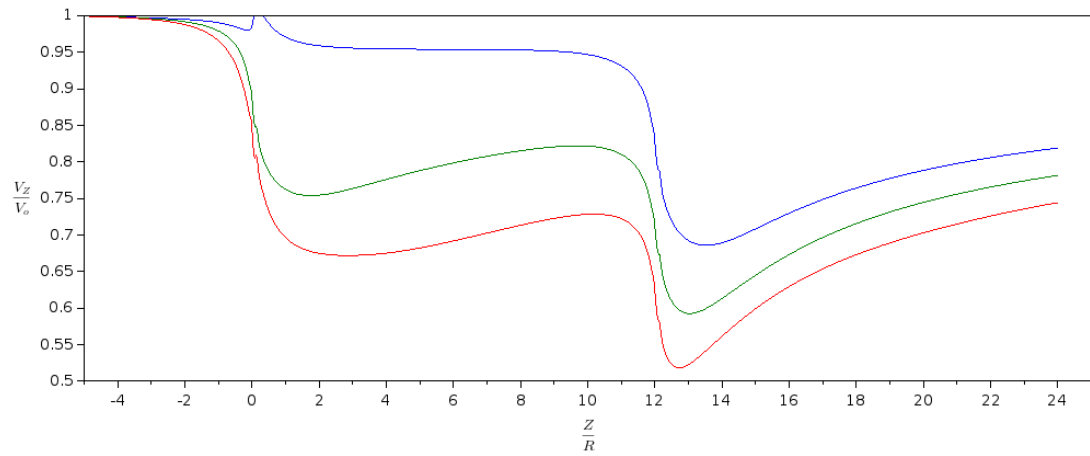


Figure 5.25: Velocity profile through the centre of the domain offset by 4m with velocity behind the 7.5m (blue), 10m (green) and 12.5m (red) turbines

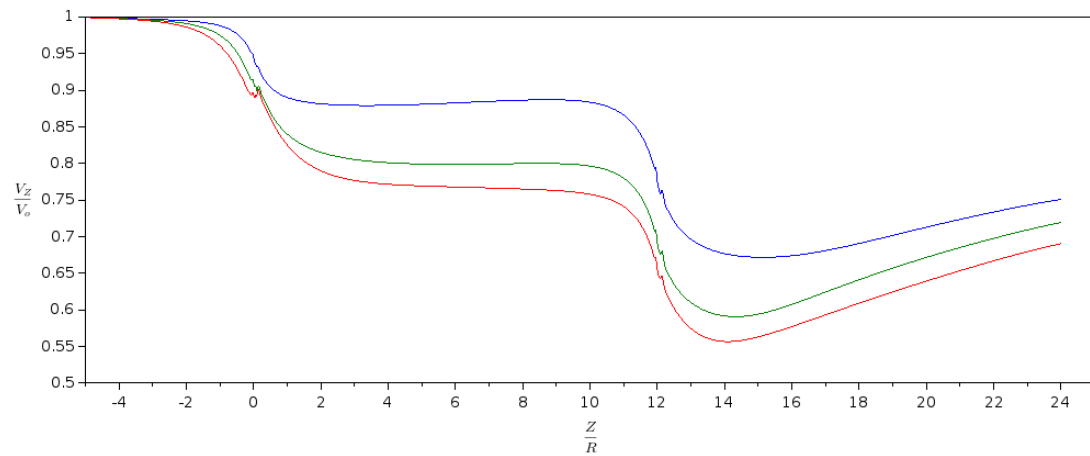


Figure 5.26: Velocity profile through the centre of the domain offset by 2m with velocity behind the 7.5m (blue), 10m (green) and 12.5m (red) turbines

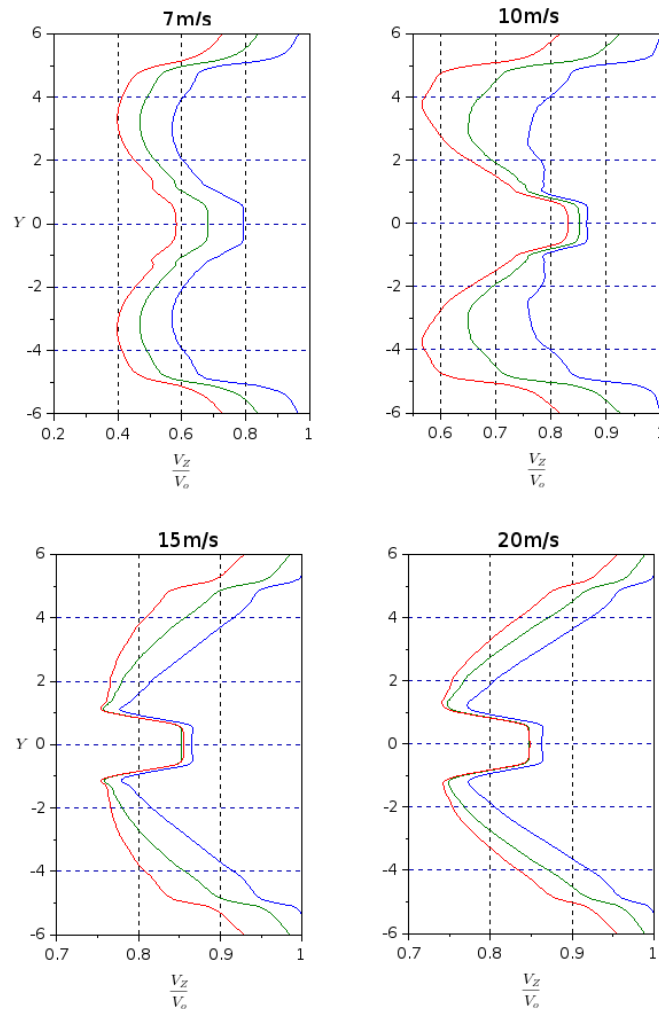


Figure 5.27: Velocity profiles at the second turbine for each wind speed of 7m/s 10m/s, 15m/s and 20m/s respectively and the different colours represent the different turbine configurations; 7.5m turbine (blue), 10m turbine (green) and 12.5m turbine (red)

5.5.4 60m spacing second turbine power

This subsection details the results of the 12 simulations where the spacing between the two turbines was 60m, specifically the power. Figure 5.28 shows the approximate power extracted by the second turbine, using equation (5.4), for each wind speed using the average velocities from Table 5.7. It shows that the greatest power is extracted by the turbine behind the 7.5m turbine and the greatest power deficit occurs at the turbine

Wind speed [m/s]	Rotor size [m]		
	7.5	10	12.5
7	4.65	4.00	3.54
10	8.07	7.35	6.88
15	12.9	12.4	12.1
20	17.2	16.6	16.2

Table 5.7: Average velocity at the second turbine to 3 s.f.

Wind speed [m/s]	Rotor size [m]			
	7.5	%	12.5	%
7	0.649	16.2	-0.460	-11.5
10	0.724	9.86	-0.463	-6.30
15	0.525	4.23	-0.277	-2.23
20	0.665	4.02	-0.322	-1.94

Table 5.8: Velocity difference at the second turbine compared to the baseline to 3 s.f.

behind the 12.5m turbine. Table 5.9 shows the difference in power in terms of magnitude and percentage of the turbines behind the 7.5m and 12.5m turbines compared to the turbine behind the 10m turbine. The greatest power difference is at 20m/s where an extra 10kW was extracted by the turbine behind the 7.5m turbine compared to the turbine behind the 10m. It shows that for all wind speeds the greatest percentage power variation is at 7m/s with the percentage decreasing as the wind speed increases. It shows that turbine behind the 7.5m turbine extracts the most power, nearly 60% more power than the turbine behind the 10m turbine and 2.28 times more power than the turbine behind the 12.5m turbine at 7m/s. Even at 10m/s the turbine behind the 7.5m turbine extracts 12.5% more power than the turbine behind the 10m turbine and 19% more power than the turbine behind the 12.5m turbine.

However, as the configuration contains two turbines, to get a fuller picture of the situation the turbines need to be considered together. Figure 5.29 shows the combined power of the first and second turbines taken from Table 5.5 and Figure 5.28 for each wind speed. Table 5.10 shows the difference in power in terms of magnitude and percentage of the turbines configurations with different diameters compared to the turbine

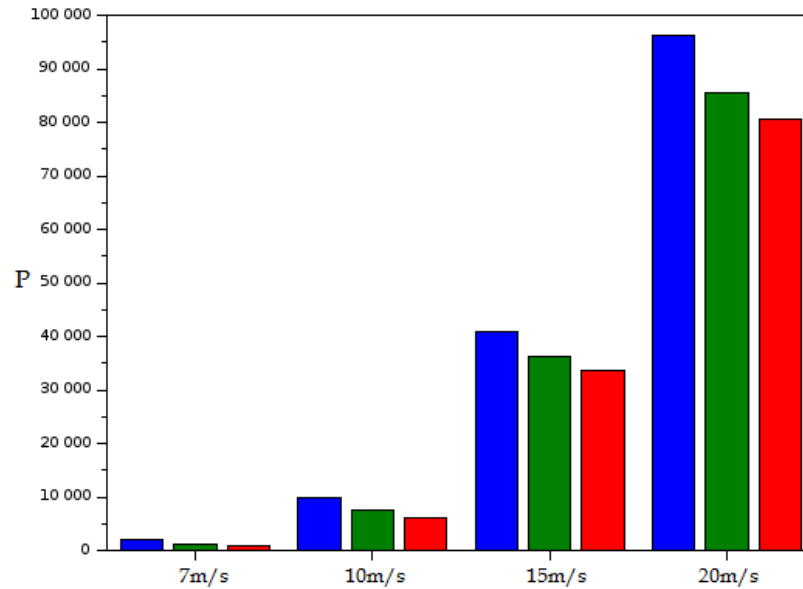


Figure 5.28: Power extracted by the second turbine (7.5m turbine (blue), 10m turbine (green) and 12.5m turbine (red)) at different wind speeds

Wind speed [m/s]	Rotor size [m]			
	7.5	%	12.5	%
7	686	57.0	-370	-30.7
10	2430	32.6	-1330	-17.7
15	4770	13.2	-2360	-6.54
20	10700	12.5	-4890	-5.72

Table 5.9: Difference in power extracted by the second turbines compared to the baseline to 3 s.f.

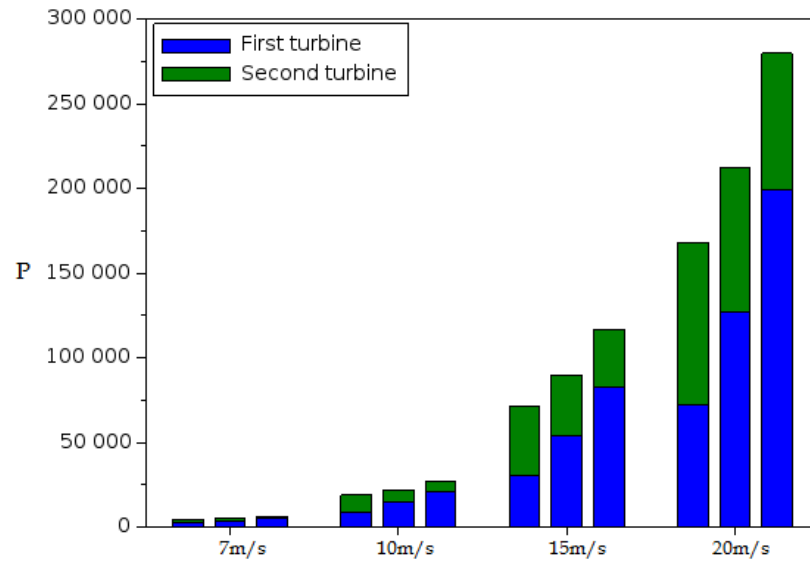


Figure 5.29: Combined power extracted by the first and second turbines at different wind speeds

Wind speed [m/s]	Rotor size [m]			
	7.5	%	12.5	%
7	- 551	-10.8	990	19.4
10	- 3240	-14.7	5370	24.4
15	- 18400	-20.5	27000	30.2
20	- 44300	-20.8	67300	31.7

Table 5.10: Comparison in the combined power extracted by the 7.5m and 12.5m configurations with the baseline configuration to 3 s.f.

layout containing just 10m turbines. Figure 5.29 and Table 5.10 show that the greatest power variation both in terms of magnitude and percentage difference occurs at 20m/s and the smallest variation occurs at 7m/s. It also shows that the 12.5m turbine configuration extracts the greatest amount of power and the 7.5m configuration extracts the least.

Table 5.11 shows the power deficit between the first and second turbines. It shows that all turbines behind the 10m and 12.5m turbines experienced a power deficit of between 30-85% depending on the turbine size and wind speed. The turbines behind the 12.5m turbine experienced the largest power deficit for each wind speed. The

Wind speed [m/s]	Rotor size [m]		
	7.5	10	12.5
7	28.8	69.1	84.1
10	-11.7	48.6	71.1
15	-34.3	32.6	59.3
20	-33.8	32.6	59.5

Table 5.11: Power deficit of the second turbine to 3 s.f.

turbine behind the 7.5m turbine has the least power deficit of 28% at 7m/s and for all other wind speeds the second turbine extracts more power than the first turbine, up to 34%.

5.5.5 30m spacing wake

The subsection details the results of the 12 simulations where the spacing between the two turbines was 30m, specifically looking at the wake and velocities. Figure 5.30 shows the velocity profiles 70m downwind of the first turbine and/or 40m behind the second turbine. Each turbine configuration is shown in a different colour where the velocity behind the 7.5m turbine is blue, behind the 10m turbine is green and behind the 12.5m turbine is red. The majority of the velocity profiles have one deficit peak representing the far wake region. Similar to the 60m situation the velocity behind the 7.5m turbine experiences the smallest velocity deficit and the turbine behind the 12.5m turbine experiences the highest velocity deficit. It shows that the wake behind the 12.5m turbine is widest and the wake behind the 7.5m turbine is the narrowest. Figures 5.31 and 5.32 show the velocity profiles through the centre of the domain offset by 4m and 2m respectively showing the velocity behind the 7.5m (blue), 10m (green) and 12.5m (red) turbines. Here very similar velocity profiles are observed to those of the 60m spacing situation, with the velocity recovering quicker after the second turbine compared to the first and that the velocity behind the 7.5m turbine is constantly higher than the other turbines.

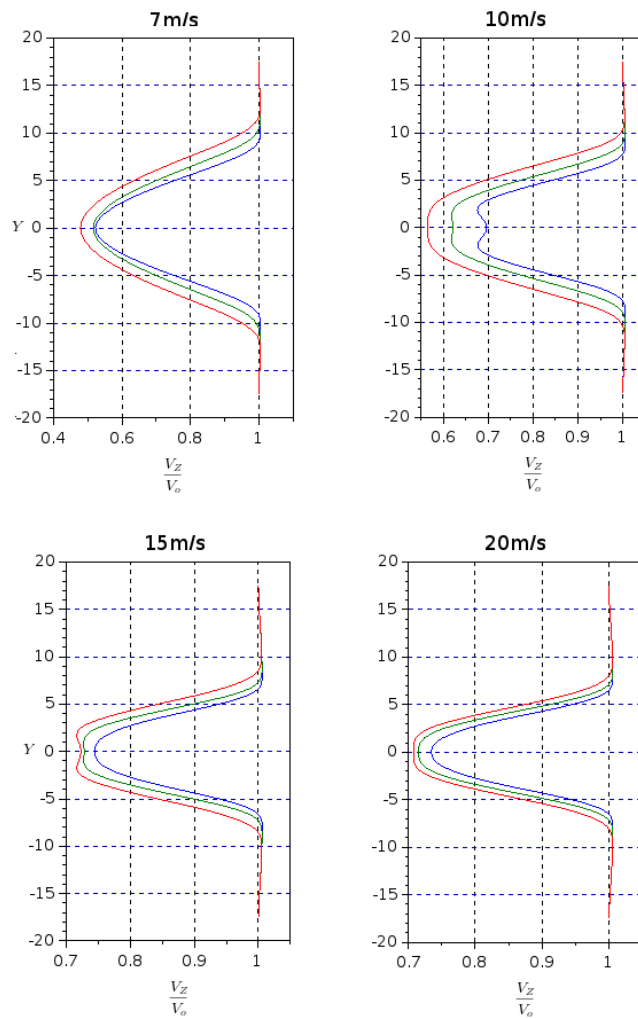


Figure 5.30: Velocity profiles 70m behind the first turbine for each wind speed of 7m/s 10m/s, 15m/s and 20m/s respectively with the different colours representing the different turbine configurations; 7.5m turbine (blue), 10m turbine (green) and 12.5m turbine (red)

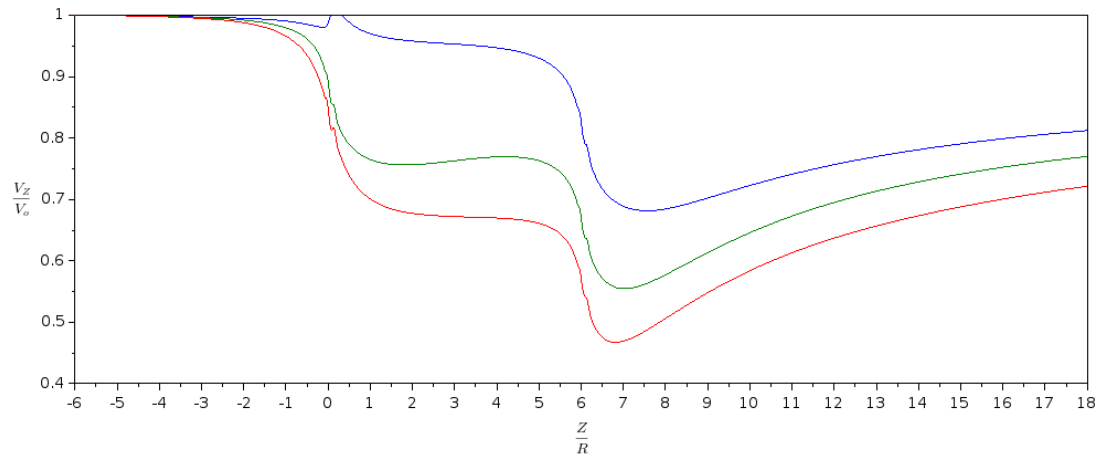


Figure 5.31: Velocity profile through the centre of the domain offset by 4m with velocity behind the 7.5m (blue), 10m (green) and 12.5m (red) turbines

5.5.6 30m spacing second turbine velocity

Figure 5.33 shows the normalized velocity profiles at the rotor of the second turbine for each wind speed. It shows that the greatest velocity variation is along the blade section of the rotor approximately 4m off centre and for the 10m/s wind speed which is similar to the 60m spacing situation. The smallest variation is found around the centre of the rotor where the hub would be located approximately less than 1m from centre. Table 5.12 shows the average velocity at the second rotor for each wind speed. Table 5.13 shows the difference in average velocity both magnitude and percentage of the 7.5m and 12.5m turbines compared to the 10m turbine. Tables 5.12 and 5.13 show the highest velocity magnitude difference is at 10m/s and smallest is at 15m/s for all turbines. The greatest velocity percentage difference occurs when $V_z = 7\text{m/s}$. The greatest average velocity at the turbine for each wind speed was experience by the turbine behind the 7.5m turbine, which was between 3.5-18% higher than that behind the 10m turbine and up to 35% higher than that behind the 12.5m turbine. Increasing the wind speed decreases this percentage difference for all turbines.

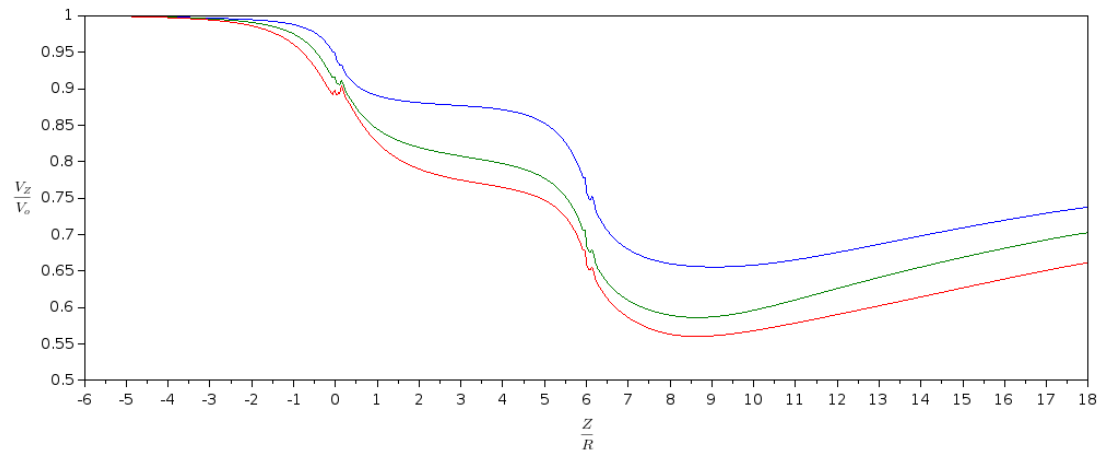


Figure 5.32: Velocity profile through the centre of the domain offset by 2m with velocity behind the 7.5m (blue), 10m (green) and 12.5m (red) turbines

Wind speed [m/s]	Rotor size [m]		
	7.5	10	12.5
7	4.54	3.84	3.38
10	7.98	7.29	6.91
15	12.9	12.4	12.1
20	17.1	16.5	16.2

Table 5.12: Average velocity at the second turbine with a spacing of 30m to 3 s.f.

5.5.7 30m spacing second turbine power

This subsection details the results of the 12 simulations where the spacing between the two turbines was 30m, specifically at the power. Figure 5.34 shows the approximate power extracted by the second turbine, using equation (5.4), for each wind speed using the average velocities from Table 5.12. It shows that the greatest power is extracted

Wind speed [m/s]	Rotor size [m]			
	7.5	%	12.5	%
7	0.698	18.2	0.469	12.2
10	0.695	9.54	0.376	5.15
15	0.464	3.75	0.223	1.80
20	0.583	3.54	0.276	1.67

Table 5.13: Velocity difference at the second turbine compared to that behind the baseline to 3 s.f.

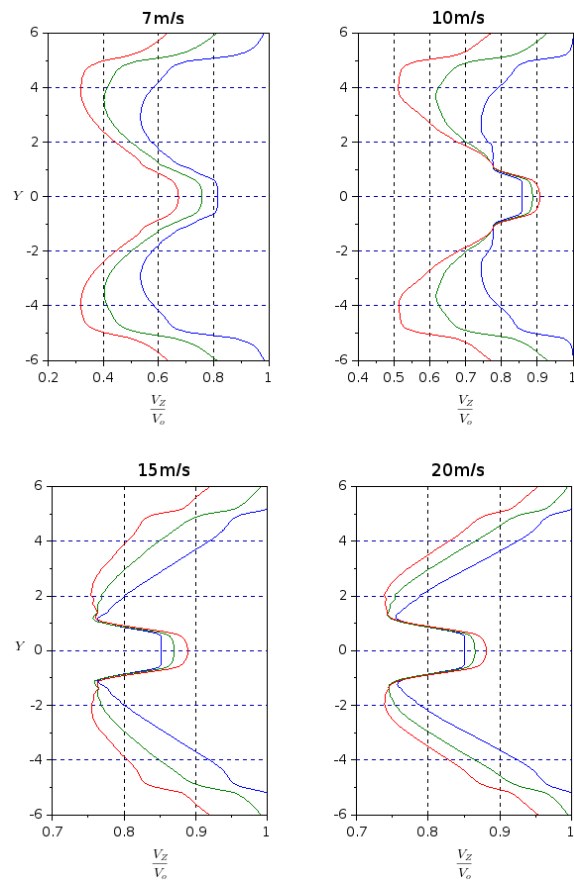


Figure 5.33: Velocity profiles at the second turbine for each wind speed of 7m/s 10m/s, 15m/s and 20m/s respectively and the different colours represent the different turbine behind the 7.5m turbine (blue), 10m turbine (green) and 12.5m turbine (red)

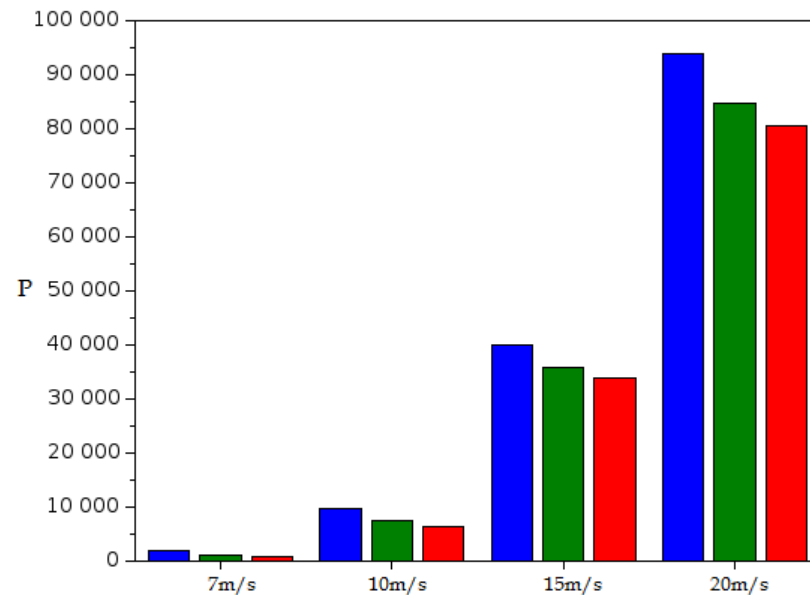


Figure 5.34: Power extracted by the second turbine (7.5m turbine (blue), 10m turbine (green) and 12.5m turbine (red)) at different wind speeds

by the turbine behind the 7.5m turbine and the least power is extracted by the turbine behind the 12.5m turbine. Table 5.14 compares the power data showing the difference in power in terms of magnitude and percentage of the turbines behind the 7.5m and 12.5m turbines compared to the turbine behind the 10m turbine. It shows that for all wind speeds the greatest percentage power variation is at wind speed of 7m/s. The greatest power different was at 20m/s, where an extra 13kW was extracted by the turbine behind the 7.5m turbine compared to the turbine behind the 12.5m. It shows that the turbine behind the 7.5m turbine extracts nearly 65% more power than the turbine behind the 10m turbine and 2.44 times more power than the turbine behind the 12.5m turbine at 7m/s. Increasing the wind speed reduces the power difference between the turbines to approximately 5%.

Similar to the 60m spacing situation to get the full picture both turbines need to be considered together. Figure 5.35 shows the combined power of the first and second turbines taken from Table 5.5 and Figure 5.34 for each wind speed. Table 5.15 shows the difference in power in terms of magnitude and percentage between configurations

Wind speed [m/s]	Rotor size [m]			
	7.5	%	12.5	%
7	695	64.9	-346	-32.3
10	2300	31.4	-1070	-14.7
15	4170	11.7	-1900	-5.32
20	9290	11.0	-4170	-4.94

Table 5.14: Difference in power of the second turbines compared to 10m turbine to 3 s.f.

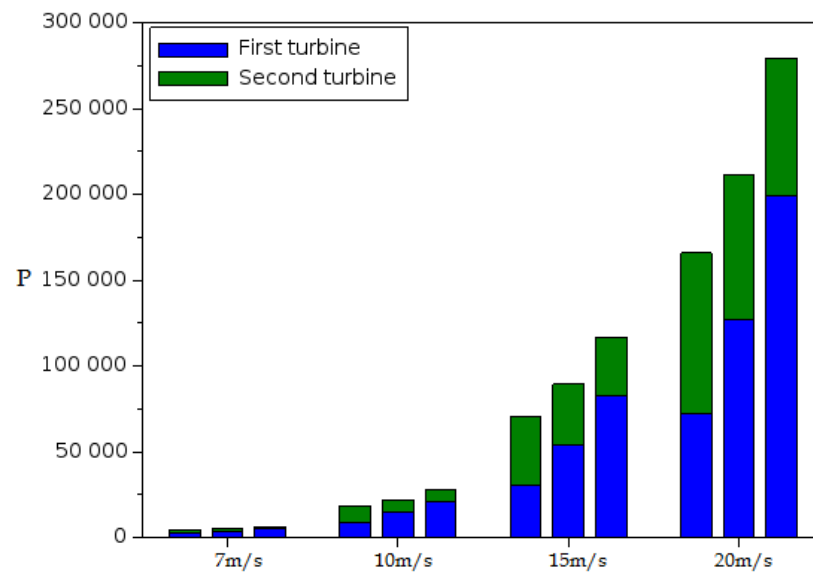


Figure 5.35: Combination of the power extracted by the first and second turbines at different wind speeds

with different diameters compared to the baseline configuration containing just 10m turbines. Figure 5.35 and Table 5.15 shows that the greatest power variation both in terms of magnitude and percentage difference occurs at 20m/s and the smallest variation occurs at 7m/s. The difference between each configuration is significant with differences ranging from approximately 1.5 – 110kW between the 7.5m and 12.5m turbine configurations depending on the wind speed. It shows that the 12.5m turbine configuration extracts the greatest amount of power and the 7.5m configuration extracts the least.

Table 5.16 shows the power deficit of the second turbines compared to the first. It

Wind speed [m/s]	Rotor size [m]			
	7.5	%	12.5	%
7	- 543	-10.9	1010	20.4
10	- 3380	-15.5	5620	25.8
15	- 19000	-21.2	27500	30.8
20	- 45700	-21.6	68000	32.2

Table 5.15: Comparison in the combined power extracted by the 7.5m and 12.5m configurations with the baseline configuration to 3 s.f.

Wind speed [m/s]	Rotor size [m]		
	7.5	10	12.5
7	33.5	72.5	86.2
10	-8.21	49.8	70.7
15	-31.1	33.3	59.3
20	-30.5	33.4	59.6

Table 5.16: Power deficit of second turbine compared to the first turbine to 3 s.f.

shows that all turbines behind the 10m and 12.5m turbines experienced a power deficit of approximately 33 – 86% depending on the turbine size and wind speed. It shows that turbines behind the 12.5m turbine experiences the largest power deficit whatever the wind speed. The turbine behind the 7.5m turbine has the least power deficit of 33% at 7m/s and for all other wind speeds the second turbine extracts more power than the first turbine by up to 31%.

5.5.8 Power comparison between spacings

Table 5.17 shows the difference in power of the second turbine at difference spacings and at various wind speeds. It shows that for all but two situations the 60m spacing extracts more power than the 30m spacing. It shows that for at the lowest wind speed of 7m/s there is a 6.5 – 13% difference in power of the second turbine. However, for all other situations there is very little difference in power extraction with a maximum difference of 3%.

Wind speed [m/s]	Rotor size [m]					
	7.5	%	10	%	12.5	%
7	124	6.55	133	11.0	109	13.1
10	311	3.14	172	2.30	- 82.1	1.34
15	990	2.42	386	1.07	- 76.7	0.227
20	2350	2.45	922	1.08	206	0.256

Table 5.17: Comparison of the power extracted by the turbines with a spacing of 60m and 30m to 3 s.f.

Chapter 6

Discussion

This chapter discusses the results of the five studies presented in Chapter 5. It was shown that the actuator disc performed well when compared with experimental data in the far wake for each of the cases simulated with the near wake predictions being poorer. Here quantitative and qualitative critical evaluation of the results of each study will be performed and common discrepancies between the models analysed using data from previous chapters and independent sources evident in the literature. This penultimate chapter then closes with an examination of the rotor diameter study results, including the possible affect these may have in regard to future developments.

6.1 Computational techniques

This section reviews the computational processes employed throughout the work described in this thesis and critiques reasoning and associated consequences. All the work described in this thesis was conducted using CFD methods using two primary computational codes together with three different rotor models.

6.1.1 RANS and LES

The RANS equations were used together with the k - ω SST turbulence model for each simulation. The reasoning for solving the RANS equations as opposed to a LES method was twofold, each relating to computational expense. LES is considered more accurate as turbulence is resolved more precisely, particularly anisotropy. LES is also transient requiring the solution to be resolved in both time and space. However, this additional accuracy significantly increases the computational time. RANS is computationally less expensive as it allows steady state simulations to be conducted and is less dependent on the particular discretization process. Considering the main rotor method implemented in this work was the actuator disc, itself a time averaged representation, it was considered that the RANS solution more appropriate. The justification is evident in this thesis (§5.3 and §5.4) where no significant changes have been observed when compared with modelling analogs (e.g. LES [195] and DES [120][121]).

6.1.2 Cell type

Subsections 4.2.5 and 5.2.3 presented and compared results of two different cell types available. It was found that there was little benefit of using quadratic cells instead of linear cells for the cases investigated here. The quadratic cells predicted a slightly higher velocity deficit at the centre of the wake for all mesh densities, although no quadratic mesh predicted a higher deficit than a finer linear mesh. The linear cells showed a reduction in turbulence intensity after the peak (Figure 5.9) this is likely due to the cells adding some numerical diffusion to certain regions of the model, as all models used the same advection scheme (high resolution scheme), thus inaccurately predicting the three-dimensional turbulent behaviour of the flow field. However, a maximum variation of only 3% was observed, showing the linear cells were adequate to predict the turbulence in the cases examined here. The major difference between the

cell types was in the computational time. The quadratic cells took at least 60% more iterations to solve which translated into a minimum of 48% longer to solve (Table 5.2). Considering the results from these mesh densities, there was no clear additional accuracy observed considering the additional computational expense. Whence there was no reason to use quadratic cells instead of linear cells given the cases considered. This is due to the relatively simple geometry and flow field which has no significant recirculation or large scale turbulence structures.

6.1.3 Boundary conditions

Every CFD simulation requires boundary conditions which can have a significant impact on the solution. The importance of the appropriate boundary conditions can not be understated although their impact are not always known.

As part of the porous disc study (§§4.2.2 and §5.2) four boundary conditions were investigated, two turbulence length scales and two different definitions at the domain's upper boundary (representing a duct and channel). It was observed that the duct produced a higher central velocity magnitude and marginally lower turbulence intensity than the channel flow. This is to be expected due to the presence of the additional wall at the top of the domain. This wall creates an additional boundary layer which restricts and slows the flow near the wall. This deceleration along the wall forces the flow at the centre to increase in velocity in order to maintain the same mass flow rate which is visible in Figure 5.2. However, the influence of the approximately inviscid central core ($0.5 < y/2R < 2.5$) is minimal, meaning that modelling an open channel flow as a duct incurs minor errors, whilst reducing computational expense.

The resistance of the disc, in the porous disc study (§§4.2.2 and §5.2), was prescribed using a predefined thrust coefficient (C_T). The differences between the calculated C_T values from the channel and duct flow can be attributed to the additional

boundary layer (i.e. a new wall boundary condition at the upper boundary) and subsequent small velocity increase, in the aforementioned inviscid core. The C_T values were calculated using a free stream velocity based on the inlet velocity which is reasonable for the channel flow, as this velocity profile is fully developed. However, this is not the case for the duct flow; taking this into account the C_T values were recalculated, as shown in Table 6.1, using a new free stream velocity of 0.34m/s obtained at the domain origin in the absence of the disc. Considering these new C_T values the duct situation predicts the C_T closest to the experimental data [185].

Disc number	Study				
	Experimental [185]	Numerical [141]	Channel	Duct	New duct
1	0.61	0.65	0.60	0.64	0.61
2	0.86	0.91	0.86	0.93	0.88
3	0.97	0.98	0.93	1.00	0.96

Table 6.1: New C_T values

Similar results were found in the actuator disc study (§4.3 and §5.3) with the walls defined as both free slip and nonslip. The different boundary conditions had little influence on the results, as the boundary layer did not develop enough to influence the velocity at the disc.

Two different turbulence definitions were investigated by defining the turbulence length scale (§§4.2.2 and §5.2). Both definitions produced similar turbulence intensities at the inlet although there was a significant difference behind the disc. The second definition referred to as inlet 2 (§4.2 and §5.2) predicted a better velocity and turbulence intensity profile when compared to the experimental data [185]. This is due to a reduction in the turbulent dissipation throughout the domain, prolonging the turbulence generated at the inlet and disc which was overly dissipated using inlet 1 (§4.2).

6.1.4 ANSYS-CFX and ANSYS-Fluent

As part of this thesis two commercially available CFD codes were used, specifically ANSYS-CFX and ANSYS-Fluent. The user customization of each code is slightly different, ANSYS-CFX uses CEL and ANSYS-Fluent uses UDFs, discussed in section 2.2. UDFs are considered more flexible although for many applications this is not a consideration¹. UDFs need to be compiled into ANSYS-Fluent and they require more lines of code to be written so take longer to write and debug. In terms of implementation the two codes are very similar and although the author found CEL easier and quicker, it is personal preference.

Subsection 5.2.4 presented results of both codes on analogous models of a porous disc within a water channel. The two codes predicted very similar results, not enough for either to be considered more numerically accurate. What differences did exist had minimal affect on the overall flow field. ANSYS-Fluent predicted almost identical velocity profiles for both channel and duct simulation away from the boundary but a large difference at the boundary. This shows that the boundary layer did not develop enough to change the velocity profile, leaving the inviscid core intact (Figure 5.11). However, ANSYS-CFX predicted a slight difference between the duct and channel velocity profiles and hence a larger boundary layer, which had an affect on the velocity profile although this was minimal at the centre of the domain. ANSYS-CFX predicted a slightly higher peak in turbulence intensity compared to ANSYS-Fluent, this may be due to boundary layer prediction as the peak is due to the merger of the shear layer between the wake and free stream velocity.

The main difference between the two codes was in the time it took for the simulations to converge. ANSYS-CFX took a few hundred iterations and approximately one hour to converge whereas ANSYS-Fluent took several thousand iterations and a

¹The author has not found a situation which is beyond CEL

few hours to converge². It appears that ANSYS-Fluent processed each iteration much quicker than ANSYS-CFX however, it took ANSYS-Fluent considerably more iterations to converge. The reason for this difference is that ANSYS-CFX has a coupled solver which solves for all variables at once by creating a global solution matrix. However, the ANSYS-Fluent simulations were conducted using a segregated solver which solves for each variable sequentially [54]. Coupled solvers converge significantly quicker although they require more memory (1.5 – 2 times) as they need to store data on all variable not just one [54].

Considering that there was no numerical difference between the two codes and the additional computational expense ANSYS-Fluent required, ANSYS-CFX is the more efficient.

6.2 Rotor models

Within this thesis three different rotor models have been described and implemented, which have been compared with other numerical models and experimental data. This section will attempt to critically evaluate the differences between the models and any discrepancies found between these and analogous experimental data evident in the literature.

6.2.1 Near wake discrepancy

Throughout this thesis, discrepancies have been indicated when comparing numerically simulated results with experiments especially in the near wake. Although good agreement has been demonstrated with comparisons made with other numerical studies. Some of the salient reasons for such apparent inconsistencies (or otherwise) will be discussed in a little more detail throughout this section.

²Simulations were conducted using a dual core 2.27Ghz Intel Xeon desk top computer.

Porous disc

The porous disc study predicted a greater velocity deficit and a turbulence intensity peak at far lower magnitude and further downstream of the disc than observed experimentally [185]. This is due to the definition of the discs within the model as opposed to the physical discs. The discs within the experimental study [185] extracted momentum from the flow by converting the velocity into small scale turbulence and thus creating a high level of turbulence behind the disc and produced a variable three-dimensional momentum loss. However, the porous discs used in the simulations were defined with an isotropic 1D momentum loss which extracted momentum from the flow explicitly, reducing the velocity with no added turbulence. This explains the relatively high levels of turbulence behind the rotor for the experimental data [185] and the lack of this peak in the modelled results. The turbulence intensity, of the simulations peaked, further downstream than observed experimentally (Figure 5.4), this is due to the merger of the shear layers at the edge of the wake created by the velocity deficit; this delayed turbulence also explains the velocity deficit. The higher turbulence levels in the experimental study increased the velocity recovery, resulting in a greater velocity deficit in the simulations.

Application of the one-dimensional momentum source as a predefined constant unidirectional loss introduces an inherent flaw into the porous disc modelling procedure. Allowing for this, these models performed well and predicted some characteristics of the velocity profile and turbulence levels remarkably well. The model generally predicted both the velocity and turbulence intensity magnitudes lower than the experimental data [185] in the near wake region, with the discrepancy reducing as the flow moves downstream.

Actuator disc

In the actuator disc study, the results obtained were compared with another actuator disc model and experimental data. All three data sets showed similar velocity profiles, although both actuator disc models under-predicted the magnitude of the velocity drop just behind the turbine. This inconsistency is not just predicted by the actuator disc but has been observed in other numerical studies which have tried to replicate the experiment [118][119]. Scheper *et al.* [119] noted that no study was able to predict both the loads and velocities. Other researchers such as Réthoré *et al.* [120] noted that either the same force distribution or velocity profile may be predicted but not both, to date there is little physical interpretation for this phenomenon. However, a possible reason maybe that the force exerted by the turbine is greater than the measured values along the blade suggests. This being evidenced by predicting a closer wake comparison by increasing force along the blade. The data produced in this study predicts the highest velocity before the turbine which is due to the inlet geometry and defined inlet velocity, which had already been reduced compared to the experimental data.

This discrepancy is due to the near wake being almost completely characterized by the turbine's geometry which results in a transient flow region, not fully predicted by a time averaged model like the actuator disc. This is particularly well demonstrated in previous studies of the MEXICO data [118][119] where the transition between aerofoil sections created unexpected velocity fluctuations which were not predicted by any model but affected the near wake.

6.2.2 Actuator disc

Even though the actuator disc has been the main model used in this thesis there are various types within the literature (§2.2.2).

x/R	Normalized mean velocity			Difference (m/s)
	This study	R��thor�� <i>et al.</i> [120]	Difference (%)	
-0.4	0.919	0.955	- 3.78	- 0.351
0.0	0.873	0.841	3.80	0.353
0.3	0.818	0.710	15.2	1.74
0.6	0.818	0.764	7.02	0.652
1.0	0.804	0.739	8.81	0.819
1.5	0.809	0.735	10.0	0.930
2.0	0.826	0.688	20.2	1.88

Table 6.2: Average velocity difference between this study and R  thor   *et al.* [120]

Within the actuator disc study two different discs were compared in terms of velocity profiles. Very good agreement was found along the centre line and wake expansion. The greater discrepancy was observed at the cross-sections behind the turbine at the wake centre. The actuator disc in this study predicted little velocity deficit at the centre of the wake, whereas R  thor   *et al.* [120] predicted their highest velocity deficit at this position. This discrepancy is due to the description of the model momentum sink, specifically the hub and nacelle which was excluded in this study but was presumably included by R  thor   *et al.* [120]. This explains the difference between the velocity profiles and why R  thor   *et al.* [120] predicted almost zero velocity at the centre just behind the turbine. Further evidence of this is shown in Table 6.2, demonstrating that R  thor   *et al.* [120] predicted a lower velocity at the rotor (approximately 4%) and hence greater momentum loss, through the inclusion of the hub. Despite the higher velocity deficit just behind the rotor the average velocity was less than 10% for $0.6 < x/R < 1$. The discrepancy for $x/R \geq 1$ increases as the mesh used in this study was only refined up to $x/R = 1$, so this was expected.

6.2.3 Actuator line

The actuator line method (§3.5.2) is a transient model which represents the turbine as lines instead of a disc. As part of this thesis the AD and AL methods were implemented

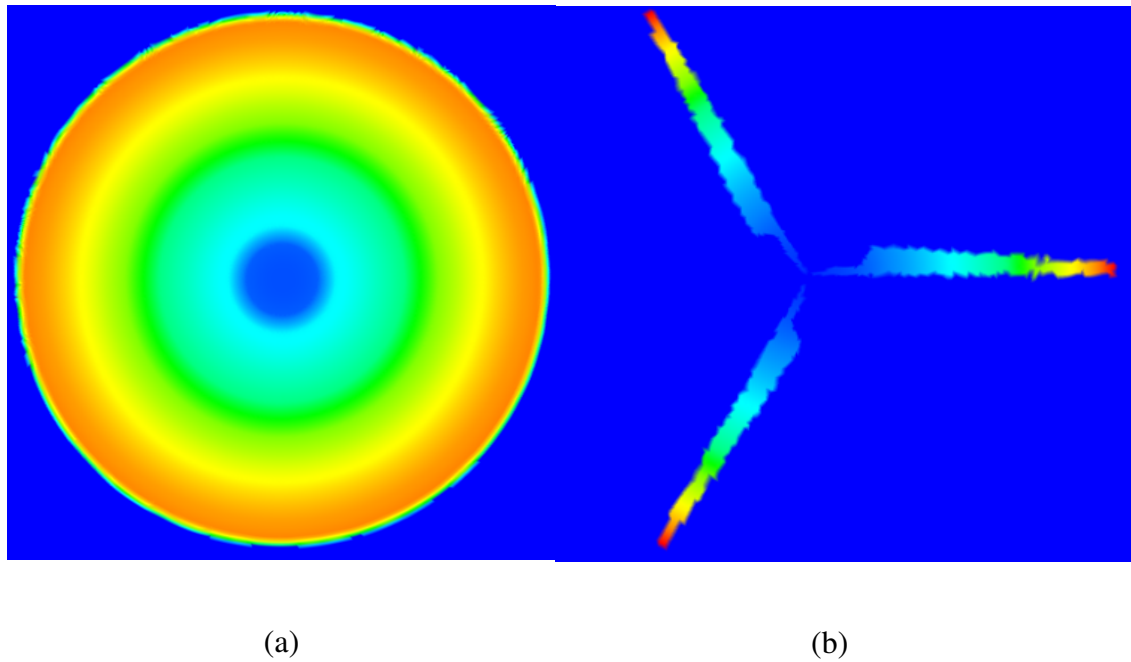


Figure 6.1: Force distribution of (a) actuator disc and (b) actuator line methods

within ANSYS-CFX. Figure 6.1 shows the force distribution of the two methods. The ALM is able to predict the tip and root vortices shown in Figure 6.2 which the ADM cannot. This additional accuracy is at the expense of computational time with the ADM taking a matter of hours but the ALM taking days.

Comparison between the ADM and ALM was conducted as part of the two turbine study (§4.4). In this instance the ALM was conducted by another author [120]. The results (§5.4) showed good agreement between the models in terms of the velocity profile behind the second turbine, showing the additional computational expense is unnecessary for turbine interactions. The ALM shows little advantage over the ADM in the far wake as the modelled vortices have broken up as part of the transition to the far wake.

Considering turbine interactions, specifically two turbines with 30m spacing, the velocity profiles at 50m and 70m behind the first turbine were compared (§4.4); at 50m the results were in very good agreement. There is less agreement at 70m particularly

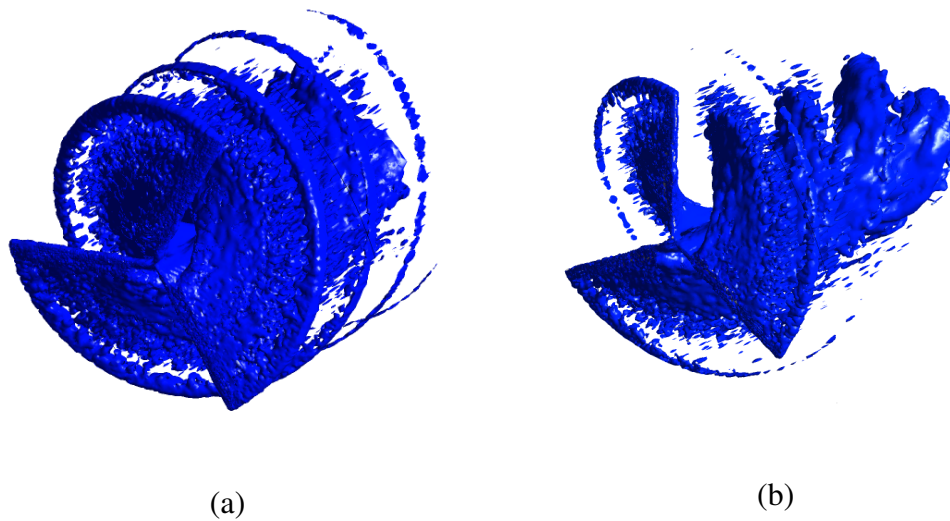


Figure 6.2: Isosurface of the vorticity (a) actuator disc and (b) actuator line methods at the centre of the wake although the edge of the wake remains in good agreement. It appears that at this distance behind the turbine, the wake has recovered more in this study, than in the numerical study detailed the literature [195]. There are two reasons for this discrepancy, being far behind the wake. Firstly, the turbulence which can not be compared may be different. Secondly, it could be due to the differences between the models, specifically the lack of tip vortices within this study, which may have caused the wake to destabilize and recover; this has been shown before to influence the wake [198].

6.2.4 Ground affect and shear

The inlets used in the work described in this thesis are nearly all defined with an uniform velocity profile. For the turbines interaction studies ground effects were not considered. This was justified (§5.4) as good agreement was found with both experimental and numerical studies which had considered these effects, and showed they had no significant influence on the velocity field. Zahle & Sørensen [156] showed that including the ground effects without a shear inflow increased the power extracted by 0.4% and

adding a shear inflow increased this further to 5.5%.

6.3 Scaling

Scaling is a significant part of fluid mechanics as there is no point in building a full scale plane just to find out if it can fly. Instead smaller, less expensive, scale models or prototypes are created which should obey what are known as scaling laws, which if satisfied the condition of similarity exists between models.

Scaling is accomplished through a branch of fluid mechanics known as dimensional analysis. A key concept in dimensional analysis involves reducing the number of flow variables, commonly to non-dimensional variables such as the Reynolds number (§1.5.2) [18]. There are several methods of reducing the dimensional variables of the flow, the Buckingham pi-theorem [206] being the most commonly used. Models are considered completely similar if all relevant dimensionless parameters have the same values. This is not always possible, instead particular similarity is normally considered such as:

- geometric similarity where all body dimensions have the same length-scale ratio;
- kinematic similarity where models have the same length-scale and time-scale ratios;
- dynamic similarity where models have the same length-scale, time-scale and force-scale ratios.

For incompressible flow with no free surface two models have dynamic similarity if the Reynolds numbers are equal [18].

6.3.1 Reynolds number

To maintain the Reynolds number when scaling, the velocity is increased to compensate for the reduction in length. In practice it is not always possible to maintain the Reynolds number when scaling a model. Increasing the velocity can create additional effects such as cavitation or compressibility. One possibility would be to change the viscosity as well as the velocity but this is not normally practical.

Scaling problems have been a factor for two studies in this thesis, specifically the porous disc and interaction studies. In the porous disc study geometrical similarity was not possible as it would have resulted in unrealistic swirl and hence cavitation in the flow due to the high RPM required to maintain the required tip speed ratio [185].

There were similar scaling issues in the two turbine study. All three studies were of course geometrically similar featuring a scaled turbine although the Reynolds number were different. The three studies had Reynolds numbers of 660 thousand, 4.5 million and 40 million for the experimental study [197], for this study and numerical study [195] respectively. Similar Reynolds numbers would have caused compressible effects in the experimental study (inlet velocity $\approx 710\text{m/s}$ and Mach number ≈ 2). If the same Reynolds number was maintained in this work it would have caused unrealistic operating conditions with an inlet velocity of 64m/s which is 2.5 times the cut off point. This increase in velocity requires the rotor velocity to increase to maintain the tip speed ratio. The rotor RPM needs to increase to 343RPM which pushes the relative velocity at the blade tip to cause compressible effects ($\text{Ma} \approx 0.6$).

However, there is a logarithmic relationship between the rotor diameter and the Reynolds number of the three studies, shown in Figure 6.3 which explains the good agreement shown in Figure 5.20.

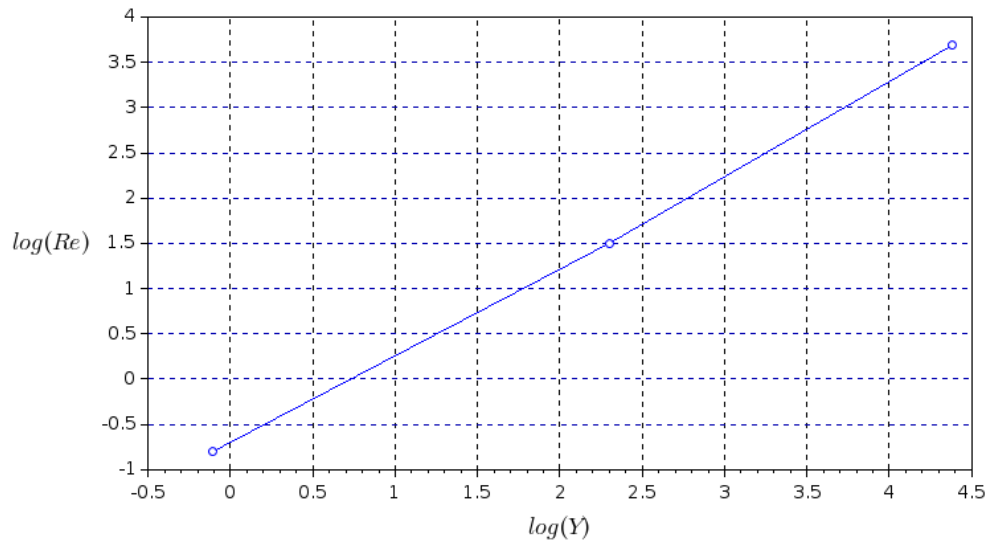


Figure 6.3: Log relationship between the Reynolds number and rotor diameter

6.4 Rotor diameter

This section discusses the results detailed in section 5.5 which investigated the influence rotor diameter size has on wind turbine wakes and the aerodynamic performance on a downwind turbine.

To begin with the first turbine was analysed in isolation, here it was found that as the diameter increased the average velocity at the rotor decreased. This decrease did not significantly influence the power which increases as the rotor diameter increases due to increase in swept area being far greater than the slight drop in velocity. The three turbines have a diameter of 7.5m, 10m and 12.5m which corresponds to a swept area of 44.2m^2 , 78.5m^2 and 123m^2 respectively which is an increase of 43.7% and 36.2% compared to a decrease in velocity of less than 7%. To investigate the affect the rotor diameter has on turbine interactions a baseline needed to be established. In this study the two 10m turbines (§4.4 and §5.4) were used for such purposes.

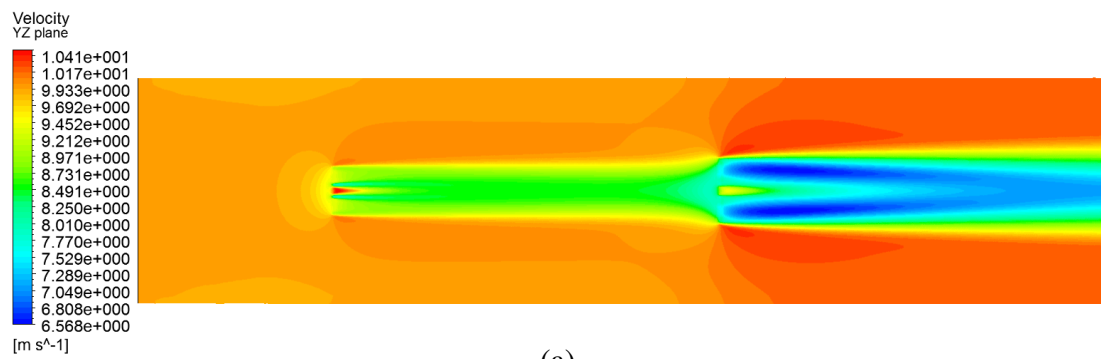
6.4.1 Wake

A downwind turbine experiences a velocity deficit and hence a power deficit compared to the first. It was shown that a turbine behind the 7.5m turbine experiences the smallest velocity deficit and narrowest wake. It had a minimum of 4% increase in velocity compared to the other turbines if spaced 60m apart and 3.5% when spaced 30m apart. Whereas, the turbine behind the 12.5m turbine experiences the highest velocity deficit and widest wake. This was expected as the 12.5m turbine extracts the most power and hence momentum reducing the velocity the most and as it is the largest it produces the widest wake. Figure 6.4 visualizes this showing the velocity contours on the yz -plane. It shows the interactions between the wakes and the difference in wake width between the three configurations. Figure 6.5 shows the streamlines through the domain and that there is more swirl in the flow after the second turbine which improves velocity recovery.

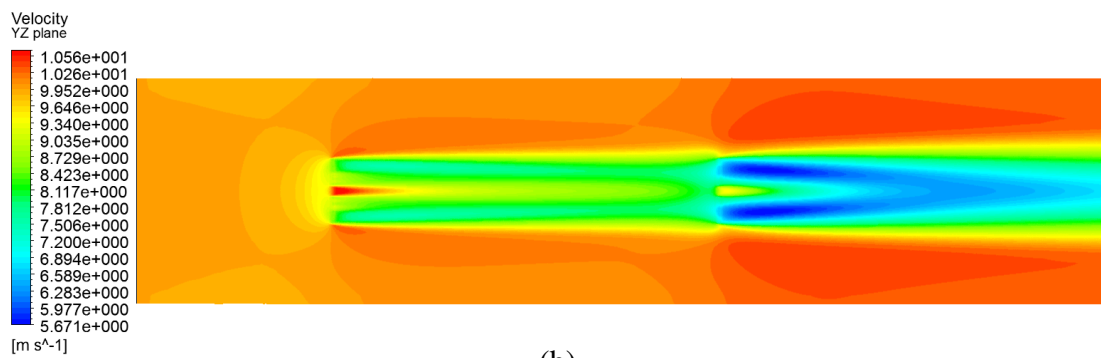
6.4.2 Power

It was shown (§§5.5.4 and §§5.5.7) that this velocity increase does translate into a power increase at the second turbine of a minimum of 12.5% if spaced 60m apart and 11% when spaced 30m apart. This is expected as the only variation in the power equation is the velocity component which is cubed.

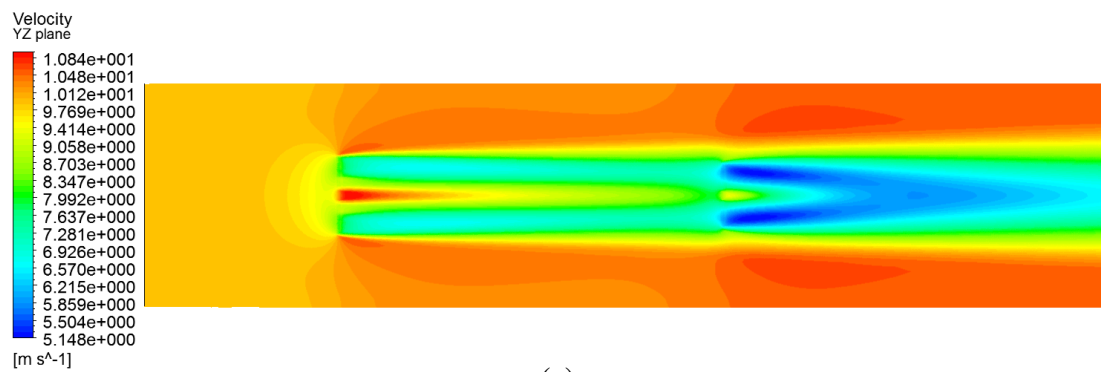
Combining the power of both turbines shows that despite the increase in power of the second turbine, the 7.5m turbine configuration extracts the lowest power overall and the 12.5m turbine configuration extracts the most power. This is because although the second turbine in the 7.5m configuration generates at least 11% more than the other turbines the first turbine extracts at least 30% less power. Considering the three configurations in this study it can be seen that rotor diameter can have a significant affect on the power extracted by as much as 40%.



(a)

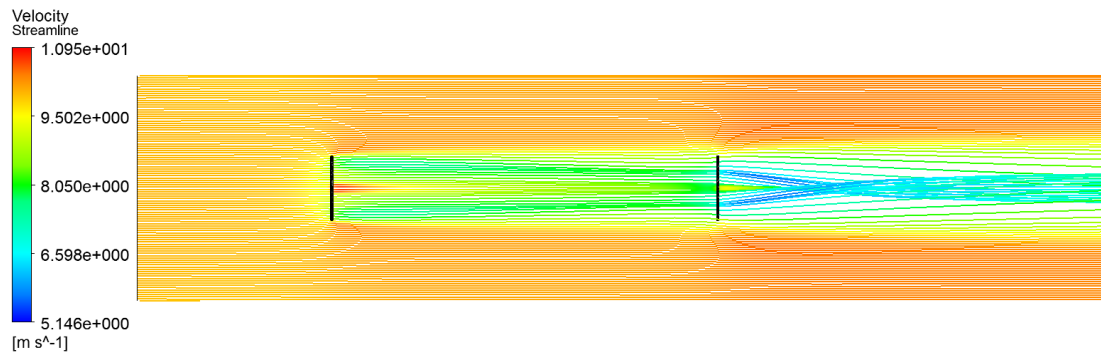


(b)

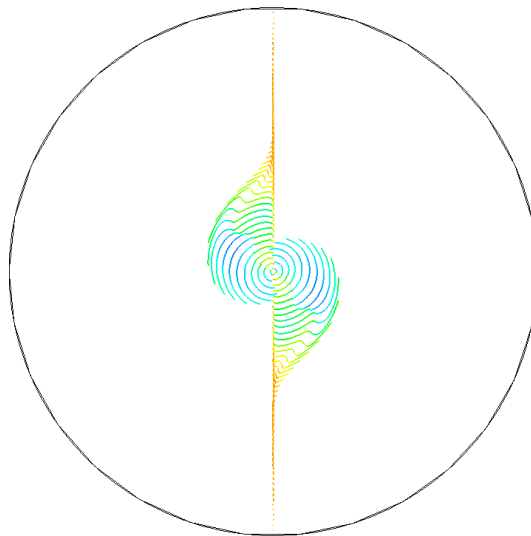


(c)

Figure 6.4: Velocity contours on the YZ plane for the (a) 7.5m configuration, (b) 10m configuration and the (c) 12.5m configuration



(a)



(b)

Figure 6.5: Streamlines viewed along (a) the yz -plane and (b) the xy -plane

Comparing the results of the different spacing situations showed that the 60m spacing extracted more power than 30m spacing. This is to be expected as the 60m spacing allows the velocity deficit to recover for longer. However, the additional distance only produced a maximum power difference of 3% for all wind speeds except for 7m/s which was 13%; this slight increase in power does not justify the additional spacing in terms of the energy density.

As previously discussed the second turbine experiences the largest velocity deficit and hence power deficit of turbines within a wind farm [13][187][188]. This work shows that the second turbine of the baseline configuration had a power loss of 33-70% depending on wind speed and spacing. Increasing the first turbine size increases the power loss of the second turbine to 60-84% depending on wind speed and spacing. However, the 7.5m turbine configuration not only reduced the power loss, the second turbine actually extracted up to 30% more power. This shows that decreasing the rotor diameter can improve the power extracted by the second turbine and a 25% decrease in rotor size results in the second turbine producing more power than the first.

Considering this a configuration with a 9m diameter rotor 60m in front of a 10m turbine was simulated. Table 6.3 shows the power extracted by a 9m turbine configuration. It shows that for this configuration the first turbine produces more power than the second as normal. This suggests that a first turbine with a diameter between 7.5 – 9m may produce a configuration where both turbines can extract the same amount of power. Comparing the 9m configuration to other configurations finds that the first turbine does extract less power and the second turbines extracts more power than the baseline. The 9m turbine has a swept area which is 19% smaller than a 10m turbine which is reflected in the power extracted in the first turbine which is approximately 19% less than the 10m turbine. The second turbine extracts approximately 4-19% more power than the 10m turbine. This results in the power extracted by the 9m configuration to be 5-10% less than the 10m turbine configuration.

Wind speed [m/s]	9m diameter		
	1st	2nd	Total
7	3400	1430	4830
10	12200	8350	20600
15	43500	37800	81300
20	103000	89200	192000

Table 6.3: Power of 9m configuration

Figure 6.6 shows the power extracted by each turbine at different wind speeds. It visually shows the large variation in the power extracted by the first turbine due to the rotor diameter and small variation in the second turbine due to the velocity variation. It shows visually the power loss of the second turbine particularly behind the 12.5m turbine which extracts the most overall power.

6.4.3 Power Coefficient

The results presented in sections 5.5.4 and 5.5.7 featured a fixed power coefficient (C_P). C_P was fixed to show the direct effect of velocity on the power however, in reality the C_P is not fixed but varies with wind speed and tip speed ratio. This section presents modified results from section 5.5.4 featuring a variable C_P . The C_P was calculated using equation (6.1). It varies based on the axial interference factor (a) which is based on the ratio between the velocity at the rotor and the free stream velocity.

$$C_P = 4a(1-a)^2 \quad (6.1)$$

$$a = 1 - \frac{U_r}{U_0} \quad (6.2)$$

Table 6.4 shows the new C_P values, for all except two situations the C_P value is lower than the 0.4 as employed in section 5.5. The 7.5m configuration experiences the highest reduction in C_P due to the increase in the velocity at the turbine. This reduction

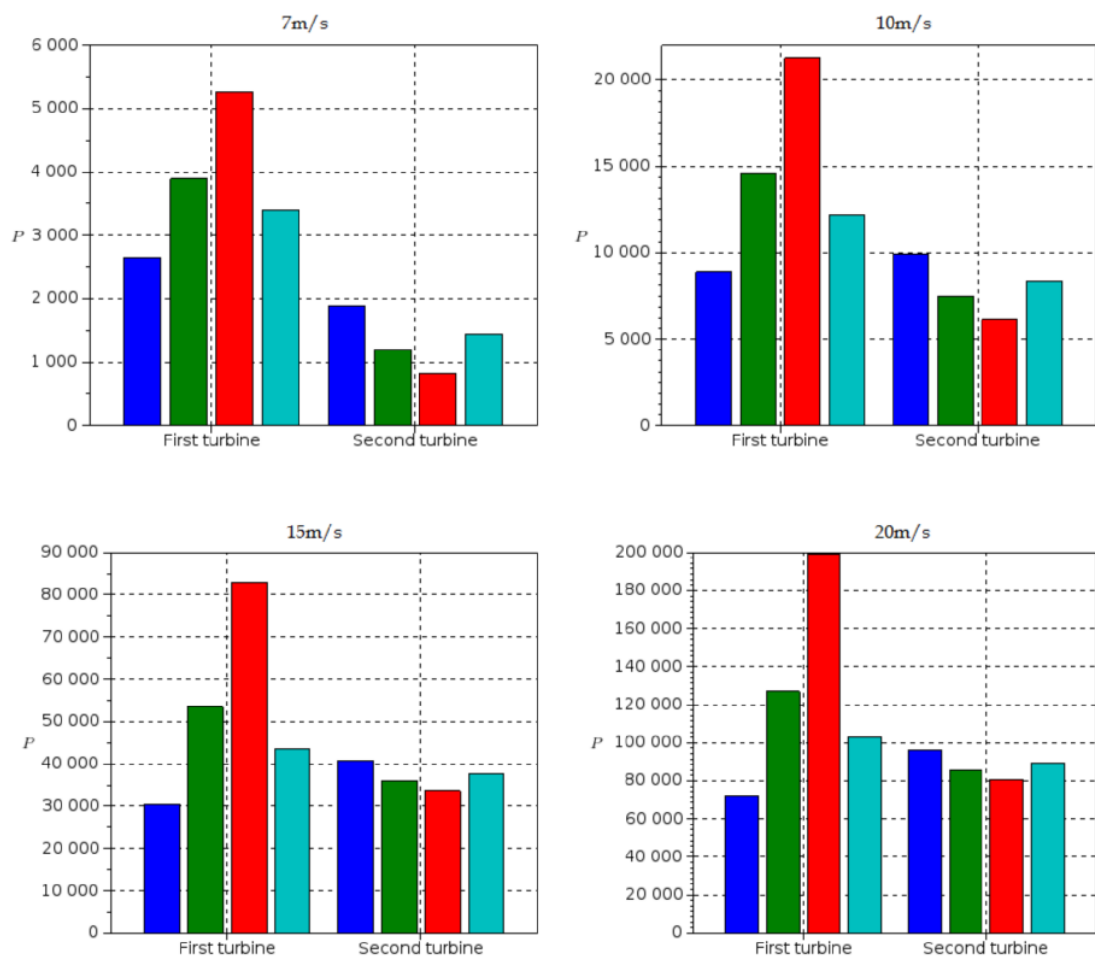


Figure 6.6: Power of each turbine at different wind speeds. Blue is the 7.5m turbine, green is the 10m turbine, red is the 12.5m turbine and light blue is the 9m turbine.

Wind speed [m/s]	Rotor size [m]		
	7.5	10	12.5
7	0.323	0.444	0.507
10	0.205	0.2795	0.332
15	0.189	0.199	0.208
20	0.192	0.199	0.195

Table 6.4: New power coefficient values to 3 s.f.

in C_P relates to a reduction in extracted power, shown in table 6.5, The exceptions being two cases where a higher C_P was calculated. Table 6.6 shows that a variable C_P exaggerates the differences between the turbines, with the 7.5m turbine extracting 60% less than the baseline (2 – 18% more than with a fixed C_P) and 12.5m turbine extracting 1.53 – 1.74 times the baseline (3-20% higher than with a fixed C_P).

Wind speed [m/s]	Rotor size [m]		
	7.5	10	12.5
7	2140	4320	6650
10	4550	10100	17600
15	14400	26700	43100
20	34500	63300	97200

Table 6.5: Approximate power extract by the first turbine with a variable C_P to 3 s.f.

Variable	7.5 m turbine		12.5 m turbine	
	Magnitude	% deficit	Magnitude	factor
7	- 2180	50.4	2330	1.54
10	- 5580	55.1	7500	1.74
15	- 12300	46.0	16400	1.61
20	- 28700	45.4	34000	1.54

Table 6.6: Power difference of the first turbines compared with the baseline using a variable C_P to 3 s.f.

When considering the second turbine there is an issue with the definition of the C_P value, as it involves the power in the wind. As the first turbine has extracted power from the wind the free stream velocity is not applicable for the second turbine. Considering this a new C_P value which is referred to C_{P2} was, calculated using a velocity one

diameter in front of the turbine (referred to as the local free stream velocity), before the velocity is influenced by the turbine as shown in Figures 5.25 and 5.26. Table 6.7 shows the C_{P2} values for each turbine and that for each situation (except the 12.5m configuration at 7m/s) the $C_{P2} < C_P$. This translates into a power deficit for each situation, save the aforementioned exception (Table 6.8).

Wind speed [m/s]	Rotor size [m]		
	7.5	10	12.5
7	0.2530991	0.4074242	0.5405362
10	0.1843507	0.2514721	0.3081106
15	0.1879297	0.1950545	0.2045937
20	0.1907710	0.195539	0.1906686

Table 6.7: C_P values calculated for the second turbine referred to as C_{P2}

Wind speed [m/s]	Rotor size [m]					
	7.5		10		12.5	
	C_P	C_{P2}	C_P	C_{P2}	C_P	C_{P2}
7	1526	1196	1335	1226	1055	1126
10	5084	4566	5207	4698	5103	4734
15	19343	19192	17972	17593	17502	17246
20	46212	45881	42617	41786	39376	38414

Table 6.8: Approximate power extract by the second turbine for different C_P values

Table 6.9 shows a comparison between the power extracted by the second turbines using the variable C_P values. It shows similar characteristics to the fixed C_P results. Using a variable C_P the results are much closer with a maximum variation of 10% from the baseline configuration (except 12.5m configuration at 7m/s). These results are much closer now due to the variation in the power coefficient of the device.

Table 6.10 shows the power deficit of the second turbine compared to the first. Here, very similar predictions to the fixed C_P value data (Table 5.11 and 5.16) are observed, with the 12.5m configuration having the largest power deficit of 60-83% and the 7.5m configuration extracting more power from the second turbine.

Wind speed [m/s]	Rotor size [m]							
	7.5				12.5			
	C_P		C_{P2}		C_P		C_{P2}	
	Total	%	Total	%	Total	%	Total	%
7	190	14.3	-29	-2.45	-279	20.9	-99	-8.10
10	-122	-2.36	-131	-2.81	-103	1.98	36	0.78
15	1370	7.63	1598	9.09	-470	2.62	-346	-1.97
20	3595	8.44	4095	9.80	-3240	7.60	-3371	-8.07

Table 6.9: Difference in power of the second turbines compared to 10m turbine

Wind speed [m/s]	Rotor size [m]					
	7.5		10		12.5	
	C_P	C_{P2}	C_P	C_{P2}	C_P	C_{P2}
7	28.8	44.2	69.1	71.6	84.1	83.1
10	-11.7	-0.334	48.6	53.6	71.1	73.1
15	-34.3	-33.3	32.6	34.0	59.3	59.9
20	-33.8	-32.9	32.6	33.9	59.5	60.5

Table 6.10: Power deficit of the second turbine

Table 6.11 combines the power of the two turbines to give their overall power extracted. It shows little difference between the power extracted given the two different power coefficients. The maximum variation is 10% for the 7.5m configuration at 7m/s, all other power values have a variation of below 5%. This shows that using the free stream velocity to define the C_P is reasonable for both turbines even though there is less power for the second to extract. Table 6.12 shows the comparison between the different configurations. Furthermore, similar results to the fixed C_P results with the 12.5m configuration extracting the most power and the 7.5m configuration extracting the least are also shown. Comparing the results for different power coefficient values shows that using a variable coefficient of performance predicts higher power extraction at low values for the 10m and 12.5m configurations but lower power for all other situations. A variable C_P also predicts a greater variation between the configurations of up to 50%, due to a larger variation predicted for the first turbine.

Wind speed [m/s]	Rotor size [m]					
	7.5		10		12.5	
	C_P	C_{P2}	C_P	C_{P2}	C_P	C_{P2}
7	3669	3339	5653	5544	7709	7779
10	9635	9117	15340	14831	22738	22369
15	33744	33593	44642	44262	60553	60297
20	80748	80416	105875	105044	136630	135669

Table 6.11: Combined power of the first and second turbines for two variable C_P values

Wind speed [m/s]	Rotor size [m]							
	7.5				12.5			
	C_P		C_{P2}		C_P		C_{P2}	
	Total	%	Total	%	Total	%	Total	%
7	-1984	-35.1	-2205	-39.8	2055	36.4	2235	40.3
10	-5705	-37.2	-5714	-38.5	7397	48.2	7538	50.8
15	-10897	-24.4	-10669	-24.1	15911	35.6	16035	36.2
20	-25127	-23.7	-24627	-23.4	30755	29.0	30625	29.2

Table 6.12: Comparison in the combined power extracted by the 7.5m and 12.5m configurations with the power extracted by the 10m configuration for two variable C_P values

6.4.4 Overall performance

There are different ways to measure the performance of a wind-farm. The power production is normally the most important and in this case the 12.5m configuration clearly extracts the most. A wind-farm's performance is also measured in terms of power extracted related to the installed capacity. Considering these cases in that regard and considering the first turbine to be operating at its installed capacity, the 7.5m configuration performs best. It performs at least 8% closer to its installed capacity than the other configurations over all wind speeds using a fixed C_P and 3% closer using a variable C_P . This is because it features the least amount of wake interactions and each turbine performs closest to its optimum. Considering these two measures the 12.5m configuration extracts the most power but the 7.5m configuration performs closest to installation.

6.4.5 Wind-farm

It has been shown that reducing the diameter of the first turbine can improve the second turbine's performance by as much as 65% at low wind speeds and 10% at high speeds (§5.5.4). However, decreasing the diameter of the first turbine can also significantly decrease the pair's overall power. However, the velocity behind the second turbine is significantly higher (up to 10%) which would improve the performance of additional turbines, so would improve the performance of more than one turbine. This could allow the smaller 7.5m configuration to improve the performance of more turbines and make up for its own loss in power. Unfortunately, only two turbines were considered in this study but considering a full wind-farm or a row could have benefits not found for two turbines. It was shown that using larger turbines only effected the final velocity behind the second turbine by 4% compared to the baseline and it was shown that the 36% increase in swept area of the larger turbine more than makes up for the reduced velocity. It was also shown that the presence of the second turbine increased the wake recovery. To this end there may be scope of using a range of turbines to extract more power, with some large turbines to extract the energy and smaller ones which promote wake recovery while still extracting some power.

Chapter 7

Conclusions & Recommendations

This final chapter describes the major conclusions of the five studies conducted as part of this thesis, highlighting the novel findings. The chapter concludes with recommendations for further work which could be conducted to extend the work presented in this thesis.

The aims and objectives of this thesis as described in Section 1.2 have been satisfied. Objective 1 (§1.2) was satisfied in Section 2.2 where three rotor models were described and implemented within ANSYS-CFX and ANSYS-Fluent. Objective 2 (§1.2) was satisfied in sections 5.1, 5.2 and 5.3 where the methods employed in this thesis were benchmarked with previous theoretical, experimental and numerical work. Objective 3 (§1.2) was satisfied in section 5.4 where the aerodynamic interactions of two similar axially aligned turbines was predicted. Objective 4 and 5 (§1.2) were satisfied in subsections 5.5.4, 5.5.7 and 5.5.8 where the performance and power extraction of two aligned turbines with different rotor diameters was presented. Objective 6 (§1.2) was satisfied in Section 6.4 where possible benefits of using different sized turbines was discussed. Objective 7 (§1.2) was satisfied through the work presented at two conferences [1][2] and published within peer-reviewed journals [3]. Through these objectives the aims of the thesis were satisfied and a number of conclusions were reached

which are detailed in this chapter.

Novel contributions to knowledge

The novel contributions to knowledge provided by this thesis are concerned with the aerodynamic interaction between two turbines with different rotor diameters and how this affects performance. To the authors knowledge, this has not been investigated before either numerically or experimentally in any detail before. The work described throughout this thesis found that changing the rotor diameter of the first turbine¹ has a significant affect on both the downstream turbine and the performance of the pair as a whole; resulted in:

- a velocity increase at the second turbine by as much as 18% thereby resulting in a 65% increase in power extraction;
- conversely, the velocity can decrease as much as 12% thereby resulting in a 32% decrease in power extraction.

However, it was found that the performance of the second turbine was not as significant as the first turbine in terms of overall power extraction.

- A reduction in the first turbine's rotor diameter decreases the overall power extracted by the pair by between 10-20%.
- An increase in the first turbine's rotor diameter increased the overall power extracted by the pair by 20-32%.

Other possible novelty within this thesis may be attributed implementation of the actuator disc and actuator line methods within commercially available CFD software, specifically ANSYS-CFX and ANSYS-Fluent. The work described through out this thesis, is certainly one of the first independent attempts to conduct simulations of turbine interactions using ANSYS-CFX and most probably the first to use actuator methods which are entirely calculated by this code². Hence, the thesis contains the most detailed and comprehensive description of the implementation process of the actuator methods within ANSYS-CFX and ANSYS-Fluent.

¹(by $\pm 25\%$ in this case)

²Before starting this project the author could not find any literature in regard to the actuator methods within commercially available CFD codes. However, recently some preliminary work in this area has come to light [87]. Here, the actuator disc and line methods were implemented in ANSYS-CFX; a single turbine using prescribed forces from an external program was simulated.

7.1 Conclusions

A part from the key contributions to knowledge there are a number of other conclusions. The first part of this thesis involved implementation and benchmarking the rotor methods detailed in section 2.2. The benchmarking was conducted using previous theoretical, numerical and experimental data for turbines in water and air. The second part involved investigating the aerodynamic interactions of two turbines and how the rotor diameter of the first turbine affects these interactions.

7.1.1 Porous disk in water

Porous discs have been used both experimentally and numerically to represent turbines. This study compared CFD results of a porous disc in water with that of experimental [185] and numerical [141] studies and found:

- the modelling method was sufficient to predict the far field velocity characteristics of a porous disc;
- the CFD models was unable to match the velocity deficit and turbulence magnitude just behind the disc of the experimental study [185], although the agreement improved further downstream. This discrepancy was attributed to small scale turbulence present in the experiments and the momentum extraction method employed by the models.

The main discrepancies observed were attributed to the difference between the CFD and experimental setup in terms of the momentum source. In the CFD simulations momentum was extracted explicitly rather than converting it into small scale turbulence as in the experimental case [185]. Moreover, only an unidirectional momentum source was used, which did not account for the three dimensional effects of the real discs used in the experimental study [185].

7.1.2 Influence of the boundary conditions

The influence of the boundary conditions were investigated using two different turbulence definitions as well as two different definitions of the top of the domain representing a duct and channel.

- The two turbulence boundary conditions produced very similar inlet profiles but different profiles downstream of the disc, showing the importance of the definition of turbulence throughout the domain.
- It was found that the channel and duct simulations predicted very similar results with the duct predicting a slightly higher velocity magnitude for the majority of the domain which was discussed in subsection 6.2.1.

It demonstrated the usefulness of the duct boundary conditions (for computational ease) for representing a porous disc in open channel flow when simulating far field effects; given the particular velocity profile applied at the inlet.

7.1.3 Actuator disc in air

The actuator disc method is a very popular method for modelling turbines, however the majority of CFD studies use in-house software. Previous experimental and numerical studies were compared with CFD results conducted as part of this thesis. It featured an actuator disc in air implemented within the commercially available CFD code ANSYS-CFX and found:

- good agreement in terms of velocity profile compared with previous experimental and numerical studies. The main discrepancy was just behind the rotor and due to the force defined by the CFD model being too small to accurately predict the velocity deficit measured in the experimental data. This is likely the cause

as it was found by other studies and my inlet velocity was shown to be too high compared to other data sets.

- For this particular experiment it is possible to produce the correct load profile along the blade or the correct velocity deficit but not both, which was also found by others.
- Good agreement with previous numerical results in terms of average velocity profile behind the turbine and hence momentum loss. Difference in velocity profile is due to the distribution of the force along the turbine, specifically at the hub as the nacelle was not considered in the work in this thesis.

This study showed it is possible to implement the actuator disc methods within commercially available codes such as ANSYS-CFX. Therefore negating the need to use specially developed codes to implement the actuator methods.

7.1.4 Two turbine interactions

Within the literature there is no definitive two turbine study or benchmark, as such CFD results of two actuator discs were compared with normalized data from a previous experimental study of two model turbines and a previous numerical study of two full size turbines using the actuator line. Although each study featured different turbines both in terms of size and blade geometry and at different wind speeds it was found that:

- there was a good agreement between all data sets in terms of normalized velocity profiles. This shows it is possible to compare normalized data of different turbine studies despite the different rotor diameters and blade geometry.
- Equally, the results of this study were predicted using an actuator disc and RANS to get a time averaged prediction of the turbines. In comparison the experimental

study used model turbines and the numerical study used the actuator line method, both of which would have had tip and root vortices which the actuator disc can not predict. This shows that the influence of these vortices is not significant for the interactions between two turbines. This is compelling as the actuator disc method requires significantly less computational resources than the actuator line method.

- The second turbine experiences a power deficit of approximately 32-72% depending on the wind speed.

7.1.5 Influence of rotor diameter

It is known that the second turbine experiences the largest velocity deficit and hence power deficient within a wind-farm. Therefore improving its performance should improve the overall performance of the wind-farm. There are a number of approaches investigated within the literature such as yawing the first turbine or reducing its RPM. This study is the first to investigate the affect of the first turbine's rotor diameter has on performance. The key conclusions have already been detailed in the novel contributions to knowledge section at the start of the chapter, the other conclusions found are:

- that increasing the rotor diameter decreases the average velocity at the rotor however, the power increases as the increase in swept area is greater than the decrease in velocity;
- the second turbine improves the velocity recovery;
- reducing the first turbine diameter increases the power extracted by the second turbine to the point that it extracts up to 34% more power;

- a variable C_p exaggerates the differences between the first turbines but predicts similar power extraction for the second turbines;
- two variable C_p values predict similar power showing that using the free stream velocity to define the C_p is reasonable for both turbines even though there is less power for the second to extract;
- the spacing between the turbines has little affect on the overall power extracted, with the maximum difference of 3% found for all but the lowest wind speeds.

7.2 Recommended work

This thesis has shown that the rotor diameter of the first turbine has a significant affect on the performance of a downstream turbine. This is the first study into the influence of rotor diameter size and was limited to two axially aligned turbines, which was investigated as it represents the worst case scenario.

There are multiple avenues this research could take, four possible investigations are detailed below.

- The influence rotor diameter has on multiple turbines. It was found that reducing the rotor diameter increased the velocity throughout the domain. This suggests that more than one turbine would be effected by varying the rotor diameter.
- The influence of the rotor diameter within a turbine array. It was found that the second turbine increased wake recovery. It may be possible to use different sized turbines to improve power extraction and wake recovery by using smaller, cheaper turbine to improve the velocity for larger turbines within an array.
- The interactions of offset turbines could be investigated. The different rotor diameters produced different sized wakes, which would influence the interactions

of offset or misaligned turbines. Using different sized turbines allows the turbines to be offset both vertically and horizontally, which has not been conducted before and would likely have an affect on the turbine interactions.

- The work presented conducted CFD simulation which solved the RANS equations using uniform inlets with no ground or shear affects. Investigations could be conducted to determine these influences on the interaction, specifically considering different hub heights.

References

- [1] Johnson BMC. Analytical and numerical study of a constantly loaded actuator disk using CFX. In: 8th PhD Seminar on Wind Energy in Europe. Zurich, Switzerland; 2012. p. 5.
- [2] Johnson BMC. Implementation of Actuator Methods in ANSYS-CFX. In: 9th PhD Seminar on Wind Energy in Europe. Gotland, Sweden; 2013. p. 5.
- [3] Johnson B, Whitty J, Howe J, Francis J. Computational Actuator disk models for wind and tidal applications. *Journal of Renewable Energy*. 2014;p. In press.
- [4] Whitty J, Haydock T, Johnson B, Howe J. On the Deflexion of Anisotropic Structural Composite Aerodynamic Components. *Journal of Wind Energy*. 2014;(Article ID 987414):13.
- [5] DIRECTIVE 2009/28/EC OF THE EUROPEAN PARLIAMENT AND OF THE COUNCIL of 23 April 2009, *Official Journal of the European Union*; 2009.
- [6] Sawyer S, Rave K. *Global wind report: Annual market update 2012*. Fried L, Sawyer S, Shukla S, Qiao L, editors. GWEC; 2012.
- [7] Johnston A, editor. *Tracking Clean Energy Progress 2013: IEA input to the Clean Energy Ministerial*. IEA publications; 2013.

- [8] Chowdhury S, Zhang J, Messac A, Castillo L. Unrestricted wind farm layout optimization (UWFLO): Investigating key factors influencing the maximum power generation. *Renewable Energy*. 2012;38(1):16–30.
- [9] Katic I, Højstrup J, Jensen NO. A simple model for cluster efficiency. In: EWEC. Italy; 1986. p. 407–410.
- [10] Burton T, Sharpe D, Jenkins N, Bossanyi E. *Wind Energy HandBook*. John Wiley and Sons; 2001.
- [11] Manwell JF, McGowan JG, Rogers AL. *Wind Energy Explained: Theory, Design and Application*. John Wiley and Sons; 2009.
- [12] Sørensen T, Nielsen P, Thøgersen ML. Recalibrating wind turbine wake model parameters validating the wake model performance for large offshore wind farms. In: EWEC. Athens, Greece; 2006. p. 6.
- [13] Barthelmie RJ, Frandsen ST, Hansen K, Schepers JG, Rados K, Schlez W, et al. Modelling the impact of wakes on power output at Nysted and Horns Rev. In: EWEC. Marseille, France; 2009. p. 10.
- [14] Barthelmie RJ, Frandsen ST, Rathmann O, Hansen K, Politis ES, Prospathopoulos J, et al. Flow and wakes in large wind farms in complex terrain and offshore. In: EWEC. Brussels, Belgium; 2008. p. 10.
- [15] Barthelmie RJ, Frandsen ST, Nielsen NM, Pryor SC, Réthoré PE, Jørgensen HE. Modelling and measurements of power losses and turbulence intensity in wind turbine wakes at middelgrunden offshore wind farm. *Wind Energy*. 2007;10:217–228.
- [16] Réthoré PE. *State of the Art in Wind Farm Layout Optimization*; 2010.

- [17] Vermeer LJ, Sørensen JN, Crespo A. Wind turbine wake aerodynamics. *Progress in Aerospace Sciences*. 2003;39:467–510.
- [18] White FM. *Fluid Mechanics (Sixth Edition)*. McGraw-Hill; 2009.
- [19] Newton I. *The Principia: Mathematical Principles of Natural Philosophy*. Snowballpublishing; 2011.
- [20] Clausius R. Über die bewegende Kraft der Wärme. *Poggendorff's Annalen der Physick*. 1850;79:368–397,500–524.
- [21] Clausius R. On the Moving Force of Heat, and the Laws regarding the Nature of Heat itself which are deducible therefrom. *Philosophical Magazine and Journal of Science*. 1851;2:1–21, 102–119.
- [22] Snel H. Review of Aerodynamics for Wind Turbines. *Wind Energy*. 2003;6:203–211.
- [23] Bechmann A. *Large-Eddy Simulation of Atmospheric Flow over Complex Terrain*. Technical University of Denmark; 2006.
- [24] Wilcox DC. *Turbulence Modeling in CFD*. DCW; 2006.
- [25] Stull RB. *An Introduction to Boundary Layer Meteorology*. Kluwer Academic Publishers; 1988.
- [26] Reynolds O. An Experimental Investigation of the Circumstances Which Determine Whether the Motion of Water Shall Be Direct or Sinuous, and of the Law of Resistance in Parallel Channels. *Philosophical Transactions of the Royal Society of London*. 1883;174:935–982.

- [27] Reynolds O. On the Dynamical Theory of Incompressible Viscous Fluids and the Determination of the Criterion. *Philosophical Transactions of the Royal Society of London (A)*. 1895;186:123–164.
- [28] Jones WP, Launder BE. The prediction of laminarization with a two-equation model of turbulence. *International Journal of Heat and Mass Transfer*. 1972;15(2):301–314.
- [29] Menter FR. Zonal two-equation k - ω models for aerodynamic flows. *AIAA*. 1993;(93-2906).
- [30] Boussinesq MJ. *Théorie de l'écoulement tourbillonnant et tumultueux des liquides*. Gauthier-Villars et fils; 1897.
- [31] Réthoré PE. *Wind turbine wake in atmospheric turbulence*. Aalborg University; 2009.
- [32] Smagorinsky J. General Circulation Experiments with the Primitive Equations. *Monthly Weather Review*. 1963;91:99–164.
- [33] Lilly DK. On the application of the eddy viscosity concept in the Inertial sub-range of turbulence. NCAR; 1966. Manuscript 123.
- [34] Lilly DK. The representation of small-scale turbulence in numerical simulation experiments. NCAR; 1966. Manuscript 281.
- [35] Blazek J. *Computational Fluid Dynamics: Principles and Applications*. Elsevier; 2001.
- [36] Piomelli U. *Large-Eddy and Direct Simulation of Turbulent Flows*; 2014.

- [37] Schmitt FG. About Boussinesq's turbulent viscosity hypothesis: historical remarks and a direct evaluation of its validity. *Comptes Rendus Mécanique*. 2007;335:617–627.
- [38] Prandtl L. Über die ausgebildete Turbulenz. *ZAMM*. 1925;5:136–139.
- [39] Prandtl L. Über ein neues Formelsystem für die ausgebildete Turbulenz. *Nachr Akad Wiss Gttingen, Math Phys*. 1945;p. 6–19.
- [40] Baldwin BS, Barth TJ. A One-Equation Turbulence Transport Model for High Reynolds Number Wall-Bounded Flows. NASA; 1990. TM 102847.
- [41] Spalart PR, Allmaras SR. A One-Equation Turbulence Model for Aerodynamic Flows. *AIAA*. 1992;(92-0439).
- [42] Wilcox DC. Comparison of two-equation turbulence models for boundary layers with pressure gradient. *AIAA Journal*. 1993;31:1414–1421.
- [43] Bredberg J. On Two-equation Eddy-Viscosity Models. Chalmers University of Technology; 2001.
- [44] Kolmogorov AN. Equations of Turbulent Motion of an Incompressible Fluid. *Izv Akad Nauk SSSR*. 1942;6:56–58.
- [45] Launder BE, Sharma BI. Application of the Energy Dissipation Model of Turbulence to the Calculation of Flow Near a Spinning Disc. *Letters in Heat and Mass Transfer*. 1974;1(2):131–138.
- [46] Reynolds WC. Computation of tubulent flows. *Annual Review Fluid Mechanics*. 1976;8:183–208.
- [47] Wilcox DC. Reassessment of the Scale Determining Equations for Advanced Turbulence Models. *AIAA Journal*. 1988;26(11):1311–1320.

- [48] Menter FR. Turbulence Modeling for Engineering Flows. ANSYS inc.; 2011.
- [49] Menter FR. Two-equation eddy-viscosity turbulence models for engineering applications. *AIAA Journal*. 1994;32(8):1598–1605.
- [50] Menter FR, Kuntz M, Langtry R. Ten Years of Industrial Experience with the SST Turbulence Model. In: *Turbulence, Heat and Mass Transfer*. vol. 4; 2003. p. 625–632.
- [51] Johnson DA, King LS. A new turbulence closure model for boundary layer flows with strong adverse pressure gradients and separation. *AIAA*. 1984;(1984-0175).
- [52] Kalitzin G, Medic G, Iaccarino G, Durbin P. Near-wall behavior of {RANS} turbulence models and implications for wall functions. *Journal of Computational Physics*. 2005;204(1):265 – 291.
- [53] Rotta JC. Statistische Theorie nichthomogener Turbulenz. *Zeitschrift für Physik*. 1951;129:547–572.
- [54] ANSYS FLUENT Solver User Guide. ANSYS Inc.; 2012.
- [55] Courant R, Friedrichs KO, Lewy H. Über die partiellen Differenzgleichungen. *der mathematischen Physik Math*. 1928;100:32–74. Transl.: *On the Partial Difference Equations of Mathematical Physics*. *IBM Journal*, 11 (1967), pp. 215-234.
- [56] Zou GW, Liu SL, Chow WK, Gao Y. Large eddy simulation of Turbulent flows. *International Journal of Architectural Science*. 2006;7(1):26–34.
- [57] Ferziger JH. Direct and Large Eddy Simulation of Turbulence. In: Vincent A, editor. *Numerical Methods in Fluid Mechanics*. vol. 16. CRM; 1998. p. 53–73.

- [58] Iliescu T. Large Eddy Simulation for Turbulent Flows. University of Pittsburgh; 2000.
- [59] Deck S. Zonal detached-eddy simulation of the flow around a high-lift configuration with deployed slat and flap. AIAA. 2005;43:2372–2384.
- [60] Spalart PR, Jou WH, Strelets M, Allmaras SR. Comments on the feasibility of LES for wing and on a hybrid RANS/LES approach. In: 1st ASOSR CONFERENCE on DNS/LES; 1997. p. 137–147.
- [61] Spalart PR. Detached-Eddy Simulation. Annual Review of Fluid Mechanics. 2009;41(1):181–202.
- [62] Moin P, Mahesh K. DIRECT NUMERICAL SIMULATION: A Tool in Turbulence Research. Annual Review of Fluid Mechanics. 1998;30(1):539–578.
- [63] Turner MJ, Clough RWaHC, J TL. Stiffness and Deflection Analysis of Complex Structures. J of Aero Sci. 1956;23(9):805–823.
- [64] McDonald PW. The Cornputatdon of Transonic Flow through Two-Dimensional Gas Turbine Cascades. ASME; 1971. 71-GT-89.
- [65] ANSYS CFX Solver Theory Guide. ANSYS Inc.; 2010.
- [66] ANSYS FLUENT Solver Theory Guide. ANSYS Inc.; 2012.
- [67] Sanderse B, van der Pijl SP, Koren B. Review of CFD for wind-turbine wake aerodynamics. Wind Energy. 2011;14:799–819.
- [68] Wu Y, Porté-Agel F. Large-eddy simulation of wind-turbine wakes: Evaluation of turbine parameterizations. Boundary Layer Meteorology. 2011;138.
- [69] Aubrun S, Loyer S, Hancock PE, Hayden P. Wind turbine wake properties: Comparison between a non-rotating simplified wind turbine model and

- a rotating model. *Journal of Wind Engineering and Industrial Aerodynamics*. 2013;120:1–8.
- [70] Calaf M, Meneveau C, Meyers J. Large eddy simulation study of fully developed wind-turbine array boundary layers. *Physics of Fluids*. 2010;22:22–38.
- [71] Port-Agel F, Wu YT, Chen CH. A Numerical Study of the Effects of Wind Direction on Turbine Wakes and Power Losses in a Large Wind Farm. *Energies*. 2013;6(10):5297–5313.
- [72] Castellani F, Vignaroli A. An application of the actuator disc model for wind turbine wakes calculations. *Applied Energy*. 2013;101:432–440.
- [73] Sørensen JN, Kock CW. A model for unsteady rotor aerodynamics. *Journal of Wind Engineering and Industrial Aerodynamics*. 1995;58(3):259–275.
- [74] Troldborg N. Actuator line modeling of wind turbine wakes. Technical University of Denmark; 2008.
- [75] Mikkelsen R. Actuator disc methods applied to wind turbines. Technical University of Denmark; 2002.
- [76] Porté-Agel F, Lu H, Wu Y. A large-eddy simulation framework for wind energy applications. In: *The Fifth International Symposium on Computational Wind Engineering*; 2010. p. 21.
- [77] Porté-Agel F, Wu Y, Lu H, Conzemijs RJ. Large-eddy simulation of atmospheric boundary layer flow through wind turbines and wind farms. *Journal of Wind Engineering and Industrial Aerodynamics*. 2011;99(4):154–168.
- [78] Shen WZ, Mikkelsen R, Sørensen J, Bak C. Tip loss corrections for wind turbine computations. *Wind Energy*. 2005;8(4):457–475.

- [79] Branlard E. Wind turbine tip-loss corrections. Technical University of Denmark; 2011.
- [80] Chicacausa AM. Development of a model for computing tip loss corrections in wind turbines. University of Zaragoza; 2013.
- [81] Prandtl L. Applications of modern hydrodynamics to aeronautics. NACA; 1921. report No. 116.
- [82] Xu G, Sankar L. Computational studies of horizontal axis wind turbines. In: ASME Wind Energy Symposium; 1999. p. 6.
- [83] Lindenburg C. Investigation into rotor blade aerodynamics. ECN; 2003. ECN-C-03-025.
- [84] Sant T. Improving BEM-based aerodynamics models in Wind turbine design codes. Delft University Wind Energy Research Institute; 2007.
- [85] Hand MM, Simms DA, Fingersh LJ, Jager DW, Cotrell JR, Schreck S, et al. Unsteady Aerodynamics Experiment Phase VI: Wind Tunnel Test Configurations and Available Data Campaigns. NREL/TP-500-29955; 2001.
- [86] Bracewell R. The Fourier Transform and Its Applications. Third edition ed. New York: McGraw-Hill; 2000.
- [87] Keck RE. A numerical investigation of nacelle anemometry for a HAWT using actuator disc and line models in CFX. *Renewable Energy*. 2012;48(0):72–84.
- [88] ANSYS FLUENT 14.5 UDF Manual. ANSYS Inc.; 2012.
- [89] Sørensen JN, Shen WZ. Numerical modeling of wind turbine wakes. *Journal of Fluids Engineering*. 2002;124:393–399.

- [90] Snel H. Review of the present status of rotor aerodynamics. *Wind Energy*. 1998;1:46–69.
- [91] Sande B. Aerodynamics of wind turbine wakes Literature review. ECN Wind Energy; 2009. ECN-E-09-016.
- [92] Sørensen JN. 2.08 - Aerodynamic Analysis of Wind Turbines. In: Sayigh A, editor. *Comprehensive Renewable Energy*. Oxford: Elsevier; 2012. p. 225–241.
- [93] Rankine WJM. On the Mechanical Principles of the Action of Propellers. *Transactions of the Institution of Naval Architects*. 1865;6:13–30.
- [94] Froude RE. On the part played in propulsion by differences of fluid pressure. *Transactions of the Institute of Naval Architects*. 1889;30:390–405.
- [95] Hansen MOL. *Aerodynamics of Wind Turbines (Second Edition)*. Earthscan; 2008.
- [96] Betz A. Das Maximum der theoretisch möglichen Ausnützung des Windes durch Windmotoren. *Zeitschrift für das gesamte Turbinenwesen*. 1920;26:307–309.
- [97] Bergey KH. The Lanchester-Betz limit. *Journal of Energy*. 1979;3:382–384.
- [98] van Kuik GAM. The Lanchester-Betz-Joukowsky limit. *Wind Energy*. 2007;10:289–291.
- [99] Okulov VL, van Kuik GAM. The Betz-Joukowsky limit: on the contribution to rotor aerodynamics by the British, German and Russian scientific schools. *Wind Energy*. 2012;15(2):335–344.
- [100] Lanchester FW. A contribution to the theory of propulsion and the screw propeller. *Journal of the American Society for Naval Engineers*. 1915;27:509–510.

- [101] Joukowsky NE. Windmill of the NEJ type. In: Transactions of the Central Institute for Aero-Hydrodynamics of Moscow; 1920. And in: Joukowsky NE. Collected Papers Vol VI . The Joukowsky Institute for AeroHydrodynamics: Moscow, Russia, 1937; VI : 405-409 (in Russian).
- [102] Crespo A, Hernández J, Frandsen S. Survey of Modeling Methods for Wind Turbine Wakes and Wind Farms. *Wind Energy*. 1999;2:1–24.
- [103] Butterfield CP, Musial WP, Simms DA. Combined Experiment Phase I Final Report. NREL/TP-257-4655; 1992.
- [104] Simms DA, Hand MM, Fingersh LJ, Jager DW. Unsteady Aerodynamics Experiment Phases II-IV Test Configurations and Available Data Campaigns. NREL; 1999. TP-500-25950.
- [105] Simms DA, Schreck S, Hand MM, Fingersh LJ. NREL Unsteady Aerodynamics Experiment in the NASA-Ames Wind Tunnel: A Comparison of Predictions to Measurements. NREL; 2001. TP-500-29494.
- [106] Schepers JG, Snel H. Model experiments in controlled conditions, final report. ECN; 2007. ECN-E-07-042.
- [107] Stoevesandt B, Herraéz Hernandez I, Plischka H, Peinke J. 3D - Rotational Effects - A Lesson to Learn from the MEXCIO Experiment. In: EWEA; 2012. p. 6.
- [108] Bechmann A, Sørensen NN, Zahle F. CFD simulations of the MEXICO rotor. *Wind Energy*. 2011;14(5):677–689.
- [109] Sørensen NN, Bechmann A, Réthoré PE, Zahle F. Near wake Reynolds-averaged Navier-Stokes predictions of the wake behind the MEXICO rotor in axial and yawed flow conditions. *Wind Energy*. 2012;17:75–86.

- [110] Lutz T, Meister K, Krämer E. Near wake studies of the Mexico rotor. In: European Wind Energy Conference (EWEC); 2011. p. 161–165.
- [111] Carrión M, Steijl R, Woodgate M, Barakos G, Munduate X, Gomez-Iradi S. Computational fluid dynamics analysis of the wake behind the MEXICO rotor in axial flow conditions. *Wind Energy*. 2014;p. 1–23.
- [112] Grasso F, van Garrel A. Near Wake Simulation of Mexico rotor in Axial and Yawed Flow Conditions with Lifting Line Free Wake Code. In: Wake Conference; 2011. p. 9.
- [113] Micallef D, Kloosterman M, Ferreira CS, Sant T, van Bussel G. Validating BEM, Direct and Inverse Free Wake Models with the MEXICO Experiment. 48th AIAA Aerospace Sciences Meeting; 2010. AIAA 2010-462.
- [114] Breton S, Sibuet C, Masson C. Using the Actuator Surface Method to Model the Three-Bladed MEXICO Wind Turbine. In: 48th AIAA Aerospace Sciences meeting; 2010. p. 11.
- [115] Shen W, Sørensen J, Yang H. Actuator Line/Navier-Stokes Computations for Flows past the Yawed MEXICO Rotor. In: Wake Conference; 2011. p. 6.
- [116] Shen WZ, Zhu WJ, Sørensen J. Actuator line/Navier-Stokes computations for the MEXICO rotor: comparison with detailed measurements. *Wind Energy*. 2012;15(5):811–825.
- [117] Schepers JG, Pascal L, Snel H. First results from Mexnext: Analysis of detailed aerodynamic measurements on a 4.5 m diameter rotor placed in the large German Dutch Wind Tunnel DNW. In: European Wind Energy Conference and Exhibition (EWEC); 2010. p. 9.

- [118] Schepers JG, Boorsma K, Cho T, Schaffarczy SGIG, Jeromin A, Shen WZ, et al. Final report of IEA Task 29, Mexnext (Phase 1), Analysis of Mexico wind tunnel measurements. Energy Research Center of the Netherlands, ECN; 2011. ECN-E-12-004.
- [119] Schepers JG, Boorsma K, Munduate X. Final Results from Mexnext-I: Analysis of detailed aerodynamic measurements on a 4.5 m diameter rotor placed in the large German Dutch Wind Tunnel DNW. In: *The Science of Making Torque From Wind*; 2012. p. 24.
- [120] Réthoré PE, Zahle F, Sørensen N, Bechmann A. CFD Simulations of the MEXICO Wind Tunnel and Wind Turbine. In: *EWEA Annual Event*; 2011. p. 8.
- [121] Réthoré PE, Zahle F, Sørensen N, Bechmann A. MEXICO wind tunnel and wind turbine modelled in CFD. In: *41st AIAA Fluid Dynamics Conference and Exhibit*; 2011. p. 10.
- [122] Glauert H. *Aerodynamic Theory*. vol. 4. Durand WF, editor; 1935.
- [123] Lissaman PBS. Energy effectiveness of arbitrary arrays of wind turbines. In: *AIAA, Aerospace Sciences Meeting*; 1979. p. 7.
- [124] Ainslie JF. Development of an eddy viscosity model for wind turbine wakes. In: *7th EWEA Wind Energy Conference*; 1985. p. 61–66.
- [125] Ainslie JF. Calculating the flowfield in the wake of wind turbines. *Journal of Wind Engineering and Industrial Aerodynamics*. 1988;27:213–224.
- [126] Adams BM, Quarton DC. Dynamic loads in wind farms. Hassan G, editor. *Joule Project*; 1996.

- [127] Crespo A, Manuel F, Moreno D, Fraga E, Hernández J. Numerical analysis of wind turbine wakes. Proceedings Delphi Workshop On Wind Energy Applications. 1985;p. 15–25.
- [128] Crespo A, Hernández J. Numerical modelling of the flow field in a wind turbine wake. 3rd Joint ASCE/ASME Mechanics Conference Forum on Turbulent Flows. 1989;p. 121–127.
- [129] Crespo A, Manuel F, Hernández J. Numerical modelling of wind turbine wakes. In: EWEC. Madrid; 1990. p. 166–170.
- [130] Crespo A, Chacón L, Hernández J, Manuel F, Grau JC. UPMPARK: a parabolic 3D code to model wind farms. EWEC. 1994;p. 454–459.
- [131] Gómez-Elvira R, Crespo A, Migoya E, Manuel F, Hernández J. Anisotropy of turbulence in wind turbine wakes. Journal of Wind Engineering and Industrial Aerodynamics. 2005;93:797–814.
- [132] Zahle F. Wind Turbine Aerodynamics Using an Incompressible Overset Grid Method. Imperial College London; 2006.
- [133] Michelsen JA. Basis3D - a platform for development of multiblock PDE solvers. Technical University of Denmark; 1992. AFM 92-05.
- [134] Michelsen JA. Block structured multigrid solution of 2D and 3D elliptic PDEs. Technical University of Denmark; 1994.
- [135] Sørensen NN. General purpose flow solver applied to flow over hills. Risoe National Laboratory; 1995.
- [136] Ivanell S. Numerical Computations of Wind Turbine Wakes. KTH Royal Institute of Technology; 2009.

- [137] Laursen J, Enevoldsen P, Hjort S. 3D CFD Quantification of the Performance of a Multi-Megawatt Wind Turbine. *Journal of Physics: Conference Series*. 2007;75(1):1–13.
- [138] Yelmule MM, EswaraRao Anjuri VSJ. CFD predictions of NREL phase VI rotor experiments in NASA/AMES wind tunnel. *International Journal of Renewable Energy Research*. 2013;3(2):261–269.
- [139] Choi NJ, Nam SH, Jeong JH, Kim KC. Numerical study on the horizontal axis turbines arrangement in a wind farm: Effect of separation distance on the turbine aerodynamic power output. *Journal of Wind Engineering and Industrial Aerodynamics*. 2013;117(0):11–17.
- [140] Harrison ME, Batten WMJ, Myers LE, Bahaj AS. A comparison between CFD simulations and experiments for predicting the far wake of horizontal axis tidal turbines. In: *8th European Wave and Tidal Energy Conferences*. Uppsala, Sweden; 2009. p. 10.
- [141] Harrison ME, Batten WMJ, Myers LE, Bahaj AS. Comparison between CFD simulations and experiments for predicting the far wake of horizontal axis tidal turbines. *IET Renewable Power Generation*. 2010;4:613–627.
- [142] Mahu R, Popescu F. NREL Phase VI rotor modeling and simulation using ANSYS FLUENT 12.1. *Mathematical Modeling In Civil Engineering*. 2011;p. 185–194.
- [143] Mahu R, Popescu F, Frunzulica F, Dumitrache A. 3D CFD Modeling and Simulation of NREL Phase VI Rotor. *AIP Conference Proceedings*. 2011;1389(1):1520–1523.

- [144] Qunfeng L, Jin C, Jiangtao C, Ning Q, Danao LAM. Study of CFD simulation of a 3-D wind turbine. In: *Materials for Renewable Energy Environment (ICMREE)*. vol. 1; 2011. p. 596–600.
- [145] WuBow S, Sitzki L, Hahm T. 3D simulation of the turbulent wake behind a wind turbine. *Journal of Physics Conference Series* 75; 2007. 012033.
- [146] Makridis A, Chick J. CFD Modeling of the wake interactions of two wind turbines on a Gaussian hill. In: *EACWE 5*; 2009. p. 9.
- [147] Makridis A, Chick J. Validation of a {CFD} model of wind turbine wakes with terrain effects. *Journal of Wind Engineering and Industrial Aerodynamics*. 2013;123, Part A(0):12–29.
- [148] Stovall T, Pawlas G, Moriarty P. Wind farm wake simulations in OpenFOAM. 48th AIAA Aerospace Sciences Meeting; 2010. AIAA 2010-825.
- [149] Réthoré PE, Sørensen NN, Bechmann A, Zahle F. Study of the atmospheric wake turbulence of a CFD actuator disc model. In: *EWEC*. Marseille, France; 2009. p. 9.
- [150] El Kasmi A, Masson C. An extended k- ϵ model for turbulent flow through horizontal-axis wind turbines. *Journal of Wind Engineering and Industrial Aerodynamics*. 2008;96:103–122.
- [151] Cabezón D, Migoya E, Crespo A. Comparison of turbulence models for the computational fluid dynamics simulation of wind turbine wakes in the atmospheric boundary layer. *Wind Energy*. 2011;14(7):909–921.
- [152] Rados KG, Prospathopoulos JM, Stefanatos NC, Politis ES, Chaviaropoulos PK, Zervos A. CFD modeling issues of wind turbine wakes under stable atmospheric conditions. In: *EWEC*. Marseille, France; 2009. p. 8.

- [153] Johansen J, Sørensen NN, Michelsen JA, Schreck S. Detached-eddy simulation of flow around the NREL phase VI blade. *Wind Energy*. 2002;5:185–197.
- [154] Troldborg N, Sørensen JN, Mikkelsen R. Actuator Line Simulation of Wake of Wind Turbine Operating in Turbulent Inflow. *The Science of Making Torque from Wind Journal of Physics: Conference Series*. 2007;75.
- [155] Zahle F, Sørensen NN. Overset grid flow simulation on a modern wind turbine. AIAA; 2008. Paper 20086727.
- [156] Zahle F, Sørensen NN. In: *Upwind Navier-Stokes Rotor Flow Simulations with ground proximity and shear*. European Wind Energy Association (EWEA); 2010. p. 255–263.
- [157] Mann J. The spatial structure of neutral atmospheric surface-layer turbulence. *Journal of Fluid Mechanics*. 1994;272:141–168.
- [158] Mann J. Wind field simulation. *Probabilistic Engineering Mechanics* 13. 1998;13(4):269–282.
- [159] Mikkelsen R, Sørensen JN, Troldborg N. Prescribed wind shear modelling with the actuator line technique. In: *EWEC*. Milan, Italy; 2007. p. 5.
- [160] Meyers J, Meneveau C. Large eddy simulations of large wind-turbine arrays in the atmospheric boundary layer. 48th AIAA Aerospace Sciences Meeting; 2010. AIAA 2010-827.
- [161] Sørensen JN, Shen WZ, Munduate X. Analysis of wake states by a full-field actuator disc model. *Wind Energy*. 1998;1:73–88.
- [162] Ivanell S, Sørensen JN, Mikkelsen R, Henningson D. Analysis of numerically generated wake structures. *Wind Energy*. 2009;12:63–80.

- [163] Whale J, Anderson CG, Bareiss R, Wagner S. An experimental and numerical study of the vortex structure in the wake of a wind turbine. *Journal of Wind Engineering and Industrial Aerodynamics*. 2000;84:1–21.
- [164] Prospathopoulos JM, Politis ES, Chaviaropoulos PK. Modelling wind turbine wakes in complex terrain. In: EWEC. Brussels, Belgium; 2008. .
- [165] Antoniadis AF, Drikakis D, Zhong B, Barakos G, Steijl R, Biava M, et al. Assessment of CFD methods against experimental flow measurements for helicopter flows. *Aerospace Science and Technology*. 2012;19(1):86–100.
- [166] Wald QR. The aerodynamics of propellers. *Progress in Aerospace Sciences*. 2006;42(2):85–128.
- [167] Réthoré PE, Zahle F, Sørensen NN. Comparison of an actuator disc model with a full Rotor CFD model under uniform and shear inflow condition. In: 4th PhD seminar on wind energy in Europe; 2008. p. 123–126.
- [168] Réthoré PE, Zahle F, Sørensen NN. Validation of an actuator disc model. In: EWEC. Warsaw, Poland; 2010. p. 10.
- [169] Conway JT. Analytical solution for the actuator disk with variable radial distribution of load. *Journal of Fluid Mechanics*. 1995;297:327–355.
- [170] Réthoré PE, Sørensen NN. Actuator disc model using a modified Rhie-Chow/SIMPLE pressure correction algorithm. Comparison with analytical solutions. In: EWEC. Brussels, Belgium; 2008. p. 11.
- [171] Sørensen JN, Mikkelsen R, Troldborg N. Simulation and Modelling of Turbulence in Wind Farms. In: EWEC. Milan, Italy; 2007. p. 10.

- [172] Ivanell S, Mikkelsen R, Sørensen JN, Henningson D. Three dimensional actuator disc modelling of wind farm wake interaction. In: EWEC. Brussels, Belgium; 2008. p. 20.
- [173] Alinot C, Masson C. Aerodynamic simulations of wind turbines operating in atmospheric boundary layer with various thermal stratifications. ASME 2002 Wind Energy Symposium. 2002;p. 206–215.
- [174] Mikkelsen R, Sørensen JN, Øye S, Troldborg N. Analysis of Power Enhancement for a Row of Wind Turbines Using the Actuator Line Technique. Journal of Physics: Conference Series 75. 2007;(012044).
- [175] Réthoré PE, Troldborg N, Zahle F, Sørensen NN. Comparison of the Near Wake of Different Kinds of Wind Turbine CFD Models. In: Wake Conference. Gotland; 2011. p. 7.
- [176] Shen WZ, Sørensen JN, Zhang JH. Actuator surface model for wind turbine flow computations. In: EWEC. Milan, Italy; 2007. p. 8.
- [177] Shen WZ, Zhang JH, Sørensen JN. The Actuator Surface Model: A New Navier-Stokes Based Model for Rotor Computations. Journal of Solar Energy Engineering. 2009;131(1):9.
- [178] Dobrev I, Massouh F, Maalouf B. Lifting surface method for prediction of rotor vortex wake. 19ème Congrès Français de Mécanique, Marseille. 2009;p. 24–28.
- [179] Sibuet Watters C, Breton SP, Masson C. Application of the actuator surface concept to wind turbine rotor aerodynamics. Wind Energy. 2010;13:433–447.
- [180] Dobrev I, Massouh F, Rapin M. Actuator surface hybrid model. Journal of Physics: Conference Series. 2007;75(1):1–7.

- [181] Sørensen NN, Hansen MOL. Rotor performance predictions using a Navier-Stokes method. AIAA; 1998. Paper 98-0025.
- [182] Zahle F, Sørensen NN, Johansen J. Wind turbine rotor-tower interaction using an incompressible overset grid method. *Wind Energy*. 2009;12(6):594–619.
- [183] Miller W, Sitaraman J, Mavriplis D. Large Scale Simulations of Wind Farm Aerodynamics in Turbulent Atmospheric Inflow Conditions; 2013.
- [184] Bahaj AS, Myers LE, Thompson G. Characterising the wake of horizontal axis marine current turbines. In: 7th European Wave and Tidal Energy Conference. Porto, Portugal; 2007. p. 9.
- [185] Myers LE, Bahaj AS. Experimental analysis of the flow field around horizontal axis tidal turbines by use of scale mesh disk rotor simulators. *Ocean Engineering*. 2010;37:218–227.
- [186] ANSYS Modeling and Meshing Guide. ANSYS Inc.; 2005.
- [187] Beyer HG, Pahlke T, Schmidt W, Waldl HP, de Witt U. Wake effects in a linear wind farm. *Journal of Wind Engineering and Industrial Aerodynamics*. 1994;51(3):303–318.
- [188] Dahlberg J, Thor S. Power performance and wake effects in the closely spaced Lillgrund offshore wind farm. In: European Offshore Wind Conference; 2009. p. 10.
- [189] Wu YT, Porté-Agel F. Simulation of Turbulent Flow Inside and Above Wind Farms: Model Validation and Layout Effects. *Boundary-Layer Meteorology*. 2013;146:181–205.
- [190] Chamorro L, Arndt R, Sotiropoulos F. Turbulent Flow Properties Around a Staggered Wind Farm. *Boundary-Layer Meteorology*. 2011;141(3):349–367.

- [191] Chamorro LP, Porté-Agel F. Turbulent Flow Inside and Above a Wind Farm: A Wind-Tunnel Study. *Energies*. 2011;4(11):1916–1936.
- [192] Nilsson K. Numerical computations of wind turbine wakes and wake interaction : Optimization and control; 2012. QC 20130111.
- [193] Barthelmie RJ, Hansen K, Frandsen ST, Rathmann O, Schepers JG, Schlez W, et al. Modelling and measuring flow and wind turbine wakes in large wind farms offshore. *Wind Energy*. 2009;12(5):431–444.
- [194] Yang X, Kang S, Sotiropoulos F. Computational study and modeling of turbine spacing effects in infinite aligned wind farms. *Physics of Fluids*. 2012;24(11):115107 – 115107–28.
- [195] Troldborg N, Larsen GC, Madsen HA, Hansen KS, Sørensen JN, Mikkelsen R. Numerical simulations of wake interaction between two wind turbines at various inflow conditions. *Wind Energy*. 2011;14(7):859–876.
- [196] Adaramola M, Krogstad PA. Wind tunnel simulation of wake effects on wind turbine performance. In: EWEC; 2010. p. 64–67.
- [197] Bartl J, Pierella F, Sætrana L. Wake Measurements Behind an Array of Two Model Wind Turbines. *Energy Procedia*. 2012;24:305–312.
- [198] Fletcher TM, Brown RE. Simulation of wind turbine wake interaction using the vorticity transport model. *Wind Energy*. 2010;13(7):587–602.
- [199] Ozbay A. Experimental investigations on the wake interferences of multiple wind turbines. Iowa State University; 2012.
- [200] Turnock SR, Phillips AB, Banks J, Nicholls-Lee R. Modelling tidal current turbine wakes using a coupled RANS-BEMT approach as a tool for analysing

- power capture of arrays of turbines. *Ocean Engineering*. 2011;38(11):1300–1307.
- [201] O’Doherty DM, Mason-Jones A, O’Doherty T, Byrne CBB. Considerations of improved tidal stream turbine performance using double rows of contra-rotating blades. In: 8th European Wave and Tidal Energy (EWTEC); 2009. p. 9.
- [202] Steinbuch M, de Boer WW, Bosgra OH, Peters SAWM, Ploeg J. Optimal control of wind power plants. *Journal of Wind Engineering and Industrial Aerodynamics*. 1988;27(1-3):237–246.
- [203] Johnson KE, Thomas N. Wind farm control: Addressing the aerodynamic interaction among wind turbines. In: American Control Conference; 2009. p. 2104–2109.
- [204] Frandsen S, Barthelmie R, Pryor S, Rathmann O, Larsen S, Højstrup J, et al. Analytical modelling of wind speed deficit in large offshore wind farms. *Wind Energy*. 2006;9(1-2):39–53.
- [205] Wind Turbine Power Calculations. The Royal Academy of Engineering;.
- [206] Buckingham E. On Physically Similar Systems: Illustrations of the Use of Dimensional Equations. *Physics Review*. 1914;4(4):345–376.

Appendix A

Reynolds number

This appendix details two methods which can be used to prove that the Reynolds number, equation (A.2), is a ratio of the inertia force to the viscous force.

$$Re = \frac{\textit{Inertia force}}{\textit{Viscous force}} \quad (\text{A.1})$$

$$= \frac{\rho ul}{\mu} \quad (\text{A.2})$$

Equations (A.3) and (A.4) define the inertia and viscous force respectively.

$$\textit{Inertia force} = ma = \rho Ala \quad (\text{A.3})$$

$$\textit{Viscous force} = \mu A \dot{\gamma} \quad (\text{A.4})$$

Where m is the mass, a is the acceleration, A is the area, l is a length, ρ is the density, u is the velocity, μ is the dynamic viscosity and $\dot{\gamma}$ is the shear rate.

Combining these definitions produces equation (A.5).

$$= \frac{\rho A l a}{\mu A \dot{\gamma}} \quad (\text{A.5})$$

$$= \frac{\rho l a}{\mu \dot{\gamma}} \quad (\text{A.6})$$

Comparing equations (A.5) and (A.2) shows that if the Reynolds number is a ratio of the inertia force to the viscous force then $\frac{a}{\dot{\gamma}} = u$. Equation (A.7) shows that this is consistent using dimensional analysis.

$$\frac{a}{\dot{\gamma}} = \frac{[ms^{-2}]}{[s^{-1}]} = [ms^{-1}] = u \quad (\text{A.7})$$

Proof 1:

Considering strain

$$a = \frac{D\varepsilon}{Dt} \times u \quad (\text{A.8})$$

$$\dot{\gamma} = \frac{D\varepsilon}{Dt} \quad (\text{A.9})$$

Combining these variables as shown in equation (A.10), then expanding and simplifying shows that:

$$\frac{a}{\dot{\gamma}} = a\dot{\gamma}^{-1} \quad (\text{A.10})$$

$$= \frac{D\varepsilon}{Dt} \times u \times \left[\frac{D\varepsilon}{Dt} \right]^{-1} \quad (\text{A.11})$$

$$= u \quad (\text{A.12})$$

where $\frac{D}{Dt}$ is the substantial derivative, a is the acceleration, $\dot{\gamma}$ is the shear rate, ε is

the strain, u is the velocity and t is the time.

Proof 2:

This proof is provided online on the NASA website¹.

$$\text{Inertia force} = \rho u \frac{du}{dx} \quad (\text{A.13})$$

$$\text{Viscous force} = \mu \frac{d^2u}{dx^2} \quad (\text{A.14})$$

$$Re = \frac{\text{Inertia force}}{\text{Viscous force}} \quad (\text{A.15})$$

$$= \frac{\rho u \frac{du}{dx}}{\mu \frac{d^2u}{dx^2}} \quad (\text{A.16})$$

The velocity gradient is proportional to the velocity divided by a length scale l . Similarly, the second derivative is proportional to the velocity divided by the length scale squared.

$$\frac{\rho u \frac{du}{dx}}{\mu \frac{d^2u}{dx^2}} = \frac{\rho u \frac{u}{l}}{\mu \frac{u}{l^2}} = \frac{\rho u l^2}{\mu l} \quad (\text{A.17})$$

$$= \frac{\rho u l}{\mu} \quad (\text{A.18})$$

Where ρ is the density, u is the speed, μ is the dynamic viscosity, γ is the shear stress and $\nu = \frac{\mu}{\rho}$ is the kinematic viscosity.

¹<https://www.grc.nasa.gov/www/k-12/airplane/reynolds.html>